



HAL
open science

Transfer Reactions Induced with ^{56}Ni : Pairing and $N=28$ Shell Closure

Anastasia Georgiadou

► **To cite this version:**

Anastasia Georgiadou. Transfer Reactions Induced with ^{56}Ni : Pairing and $N=28$ Shell Closure. Nuclear Experiment [nucl-ex]. Université Paris Saclay (COMUE), 2018. English. NNT : 2018SACLS294 . tel-01921598

HAL Id: tel-01921598

<https://theses.hal.science/tel-01921598>

Submitted on 13 Nov 2018

HAL is a multi-disciplinary open access archive for the deposit and dissemination of scientific research documents, whether they are published or not. The documents may come from teaching and research institutions in France or abroad, or from public or private research centers.

L'archive ouverte pluridisciplinaire **HAL**, est destinée au dépôt et à la diffusion de documents scientifiques de niveau recherche, publiés ou non, émanant des établissements d'enseignement et de recherche français ou étrangers, des laboratoires publics ou privés.

Transfer Reactions Induced with ^{56}Ni : Pairing and the N=28 Shell Closure.

Thèse de doctorat de l'Université Paris-Saclay
préparée à l'Université Paris-Sud

Ecole doctorale n°576 Particules, Hadrons, Énergie et Noyaux :
Instrumentation, Imagerie, Cosmos et Simulation ((PHENICS))
Spécialité de doctorat : Structure et Réactions Nucléaires

Thèse présentée et soutenue à Orsay, le 27 septembre 2018, par

ANASTASIA GEORGIADOU

Composition du Jury :

Dr. Dominique JACQUET Directrice de Recherche, Université Paris-Sud, Institut de Physique Nucléaire d'Orsay	Présidente
Prof. Thorsten KRÖLL Professeur, TU Darmstadt	Rapporteur
Dr. Julien GIBELIN Maître de Conférences, Ecole Nationale Supérieure d'ingénieurs de Caen, LPC	Rapporteur
Dr. Giacomo DE ANGELIS Directeur de Recherche, INFN, Laboratoire National de Legnaro	Examineur
Dr. Marlène ASSIE Chargée de Recherche, Université Paris-Sud, Institut de Physique Nucléaire d'Orsay	Directrice de thèse

École Doctorale PHENIICS
Université Paris-Saclay
Institut de Physique Nucléaire d'Orsay

THÈSE

pour l'obtention du Diplôme de
Docteur en Sciences de l'Université Paris-Sud XI
Spécialité Physique Nucléaire

par

Anastasia GEORGIADOU

Le 27 septembre 2018

Transfer reactions induced with ^{56}Ni : pairing and the N=28 shell closure.

Composition du jury :

<i>Directrice de thèse</i>	Dr. Marlène ASSIÉ	IPN, Orsay
<i>Rapporteur</i>	Prof. Thorsten KRÖLL	TU Darmstadt
<i>Rapporteur</i>	Dr. Julien GIBELIN	LPC Caen
<i>Examinatrice</i>	Dr. Dominique JACQUET	Paris-Sud XI - IPN, Orsay
<i>Examineur</i>	Dr. Giacomo DE ANGELIS	GANIL, Caen

Aknowlegdements

In this following lines I would like to express my gratitude and thanks to the people who contributed in this work with one way or another.

My first thanks go to Marlène Assié the supervisor of this work who initialized this journey of mine in the world of international research and big collaboration experiments. The help that you provided to me this last months was vital for this manuscript as well as the psychological support at the end of my thesis.

I would like to express my sincere gratitude to Prof. Thorsten Kröll, Dr. Julien Gibellin, Dr. Giacomo De Angelis and Dr. Dominique Jacquet for being members of my jury and contributing to this work with fruitful discussions and commentary.

The people who helped the most during this three years are people who belong to our little subgroup in the unity of the NESTER group. Freddy Flavigny who I personally admire for his passion for science as well as his talent to teach. Dear Freddy, I will never cross that bridge in Caen again alone! I hope you will have students soon because you will make an excellent advisor and friend to them. Jacques Guillot, thank you for taking the time to teach me how to! It was very important to me to have somebody that I could ask whatever question I had without being afraid of any judgment. Last but not least, I would like to thank Yorick Blumenfeld for participating in every analysis meeting and correcting this manuscript.

Due to my talkative nature I made sure that in this last three years I've spoken to every single person not only in the NESTER group but also in the entire IPNO! I had the luck to spend lunch time with Fadi, David and Andrea while they were discussing funny things. I would like to specially thank David for his support and his understanding that we were still students that needed a pep talk ones in a while.

This last year brought me closer to some people such as Didier and Serge. Gentlemen, thank you so much for the time we spent in Japan. I had a memorable experience and the luck to know you a bit better.

Merci Céline pour toute l'aide apportée depuis le premier moment de mon arrivée à IPN. Je me souviendrai toujours de ton sourire et de tes câlins dans les moments difficiles. Sois patient dans ce monde de la recherche, ne perds pas ton charme.

A big thank you goes to Xavier for the support and the belief that he showed in me during my last year when I needed it the most.

I would like also to say a few words for my lunch time group. The theory group! I met some very interesting people there and I made some great friends! A big thank you to Paolo for being

there making me for once the fast eater of the table. Paolo, your innovative ideas and your funny way of describing them will follow me around for a while.

I would like to thank the person who showed me the way to the theory group whom I also thank for being one of my dear friends at most of the thesis life in Paris. Monsieur Noël Martin, merci pour tout ce que tu m'as appris sur Paris et surtout sur Lyon. A bientôt en Grèce (bien sur avec mon amie Sophie).

Thanks, to the people that I met as postdocs and friends, David, Phil and Laura. Thanks for all the help and the advice.

And with that we reach the point where I have to shout out a big thank you to ALL the PhD students that passed through IPN during 2015-2018.

A big thank you goes also to Benjamin. Still there when I arrived he really tried to introduce me to the topic and to show me everything he had done until that day. But the biggest thanks goes for after, when he graduated but he was still there for me whenever I wanted to ask him something.

Arriving in IPN I got the best office that I could ever wish for! Not about the space but about the 2 people that came with it: Clement and Marie-Co. Thank you so much for the times we spent together, the laughs, the drinks, the crazy dances.

Thanks to Marie-Co I had a cultural event that I could follow her there almost every weekend, as well as more friends that welcomed me in their house more then once, Maud, Pierre, Marty and Inna. Even though our roads split now I will always know that I have a place in Paris, with you and Jason to cook some pasta.

And when M.C. left it was a sad day in our office but we were lucky once more! We met Daniele, the "smile of life" as we say in Greek. An unbelievable smart guy with an amazing gift of teaching you whatever he wants. Dear Daniele, I am so lucky that I met you. Even if we live far I promise you, you won't get rid of me so easy.

My dearest Clemandela, I wish you all the best for your scientific carrier, I expect only the best from you. Thank you for being my office mate for all this time and who knows maybe we will meet again at some office in the future.

I would like to also thank the most positive person that I've ever known. Cheers to Ian! Wish you all the best to your new start. See you in Japan!!!

I would like to thank also Liqiang, Anne, Claire and Louis, for the time we spent together and all that D2I2 events.

Thanks Flo Flo for all the parties that you invited me and Perito! You will be a free elf soon as well. I wish you all the luck!

And then finally I want to thank my fantastic 4: Perito, Jana, Alice and Liss. The people who supported me this 3 years, somehow "through sickness and health". I am grateful that I have all of you in my life, my scientific brothers and sisters.

I would like to say a big thank you to my friends who were far but only a phone call away, Tea, Joe, Elena, Christina and Nancy.

I may not have a sister but these last years I gained one. A big part of this achievement belongs to you, my friend Dina. Not only you support me but also you make me believe in myself. A thank you is not enough, I only hope I can support you one day as you did.

I wouldn't be who I am if it wasn't for my parents. I am more than grateful that I am their child. They prepared me to be able to go anywhere and to not be afraid of life. Now at the end of my studies they deserve to know that I wouldn't be able to do the same without their help and constant support. Thanks to my Dad, for his scientific mind that gave birth to my passion in physics and thanks to my Mom, for her social talents that follow me everyday.

Also I would like to thank JP and Cath for their support and their help. They made sure I knew that their house was open for me whenever I wanted.

In this last lines I would like to thank my husband to be for his support and patience, for each and everyday this last year. I am lucky to thank him as well for scientifically enlightening this work. Marc, this thesis is devoted to you.

Contents

1	Introduction	8
2	Physics Motivations	12
2.1	Nucleon-Nucleon Interaction	13
2.2	Nuclear Shell Model	13
2.2.1	Mean-field potential and the spin-orbit term	15
2.2.2	N=28 shell closure	17
2.2.3	Single particle states via one-nucleon transfer	18
2.3	Pairing Correlations	23
2.3.1	Theoretical studies of np pairing	28
2.3.2	Experimental methods for the np pairing studies	28
2.3.3	Pairing via two nucleon transfer	30
2.4	Valuable experimental assets	36
3	Experimental case	39
3.1	Experimental Overview	40
3.2	Secondary beam production at GANIL	40
3.2.1	Description of the LISE spectrometer	40
3.2.2	Secondary beam of ^{56}Ni	43
3.3	Beam Tracking Detectors: CATS	44
3.4	Charged particle detection	45
3.4.1	Silicon Strip Detectors	45
3.4.2	TIARA	45
3.4.3	MUST2	47
3.5	Recoil detection	50
3.5.1	CHARISSA telescope	50

3.6	γ -ray detection	50
3.6.1	EXOGAM	51
4	Data Analysis	53
4.1	Data Analysis Overview	54
4.2	Beam Particle Selection	55
4.3	CATS	55
4.3.1	Calibration	56
4.3.2	Beam path reconstruction	56
4.3.3	Beam reconstruction at target position	57
4.3.4	Reconstruction validation	59
4.4	Targets	60
4.5	Time and Energy Calibration	61
4.5.1	MUST2: Energy and Time Calibration	61
4.5.2	DSSSD Time Calibration	63
4.6	Particle Identification	64
4.6.1	Hit on target condition	64
4.6.2	Light Particle Identification for forward angles	67
4.6.3	TIARA-Hyball Energy Calibration	68
4.6.4	EXOGAM Energy calibration	70
4.7	Energy Losses	73
4.8	Simulation for the reactions of interest	73
4.8.1	Kinematic lines and resolution	74
5	Results and Discussion	77
I	One nucleon-transfer reactions	78
5.1	The (p,d) & (d,t) reactions	79
5.1.1	Kinematic Lines	80
5.1.2	Excitation Energies	81
5.1.3	Particle-Gamma Coincidences	82
5.1.4	Background Subtraction	87
5.1.5	Angular Distribution	88
5.1.6	Theoretical Analysis	91
5.1.7	Results	98

5.1.8	Discussion	99
II	Two-nucleon transfer reaction	104
5.2	The $^{56}\text{Ni}(d,\alpha)^{54}\text{Co}$ reaction	105
5.2.1	Kinematic Lines and Excitation Energy spectra	105
5.2.2	Background Subtraction	105
5.2.3	Upper Limit Cross Section	108
5.2.4	Discussion	110
6	Conclusions	111
6.1	One-nucleon transfer	111
6.2	Two-nucleon transfer	113
	Appendices	116
A	Target Position	117
B	Fresco Input file example	119
C	Résumé en français	122
C.1	Motivation Physique	122
C.1.1	Réaction de transfert d'un nucléon	123
C.1.2	Réaction de transfert de deux nucléons	123
C.2	Dispositif expérimental	124
C.3	Résultats et conclusions	125
C.3.1	Réaction de transfert d'un nucléon	125
C.3.2	Réaction de transfert de deux nucléons	126
	Bibliography	128

1

Introduction

If one considers the atomic nucleus as a microscopic laboratory then nuclear reactions are powerful tools that let us have a glance into the microscopic world and its mechanisms. By means of nuclear reactions we are able to produce radioactive ions from stable beams, investigate beyond the ground state properties by exciting the nuclei, learn about the structure of the nuclei and enrich our understanding of the dynamics and the nuclear equation of state.

In a more general manner one can classify nuclear reactions in two main categories depending on their incidence time: the *compound – nucleus* and the *direct reactions*.

Compound-nucleus reactions form a unified system of the two colliding bodies that lives for a sufficient period of time giving the time to reach thermodynamic equilibrium. In addition, the system loses the memory of the entrance channel.

Direct reactions are characterized by the short time of interaction of the projectile with the target which is about 10^{-22} second and occur mainly on the surface of the target nucleus. The short period of time does not allow the system to lose the memory of the initial state. The main mechanism of these reactions is the loss or the exchange of few nucleons the other ones behaving like spectators [1].

Historically, the nuclear structure studies emerged by means of direct reactions in *direct kinematics*. The reactions were performed, by using light ion beams on the target consisting of the nuclei of interest. As to be able to study short-lived nuclei far from stability one has to inverse the problem. That led to the use of the *inverse kinematics* where the target consist of the light ion and the beam is produced by the short-lived unstable nuclei or else the radioactive exotic beam.

The last three decades inverse kinematics have been used to reveal the properties of the radioactive nuclei in exotic regions of the nuclear chart (see Figure 1.1), such as the drip-lines, and initialized the ability to study the shell evolution far from stability.

In this work with the use of one- and two-nucleon transfer reactions we study two different physical aspects. The doubly magic nucleus ^{56}Ni , with $N = Z = 28$, makes an excellent probe for studying the $N = 28$ shell closure next to stability as well as the neutron-proton (np) pairing correlations.

One-nucleon transfer

The Ni isotopic chain provides a variety of doubly magic nuclei. From the proton drip-line and ^{48}Ni lying in the edge of the particle-stability and being the mirror nucleus of ^{48}Ca , to the $N = Z$ ^{56}Ni and finally ^{78}Ni lying in the neutron-drip line. The shell evolution of the $N = Z = 28$ has been of great interest the recent years. With new experimental results on the neutron drip line, the $Z = 28$ magic shell reveals a resistive strength making ^{78}Ni the most neutron rich doubly magic nucleus [3]. Although as one moves to the edges of the nuclear chart the $N = 28$ shell closure becomes questionable and a quenching of the single-particle states is expected to take place.

One-nucleon transfer reactions such as (d,p), (p,d) and (d,t) are one of the most direct ways to test the single particle configuration of the magic nucleus ^{56}Ni . Measuring the $f_{7/2}$ orbit as well as the single particle states below the Fermi surface of ^{56}Ni will provide information on the robustness of the $N = 28$ magic number.

Two-nucleon transfer

An important part involved in the nucleon-nucleon (NN) interaction is the short range correlations. Inspired by the material science and the electron Cooper pairs, pairing in between the nucleons rather becomes a prominent part of the NN interaction while more and more experiments prove its existence [4].

There are two kinds of pairing, the first is called the Isovector and the other the Isoscalar

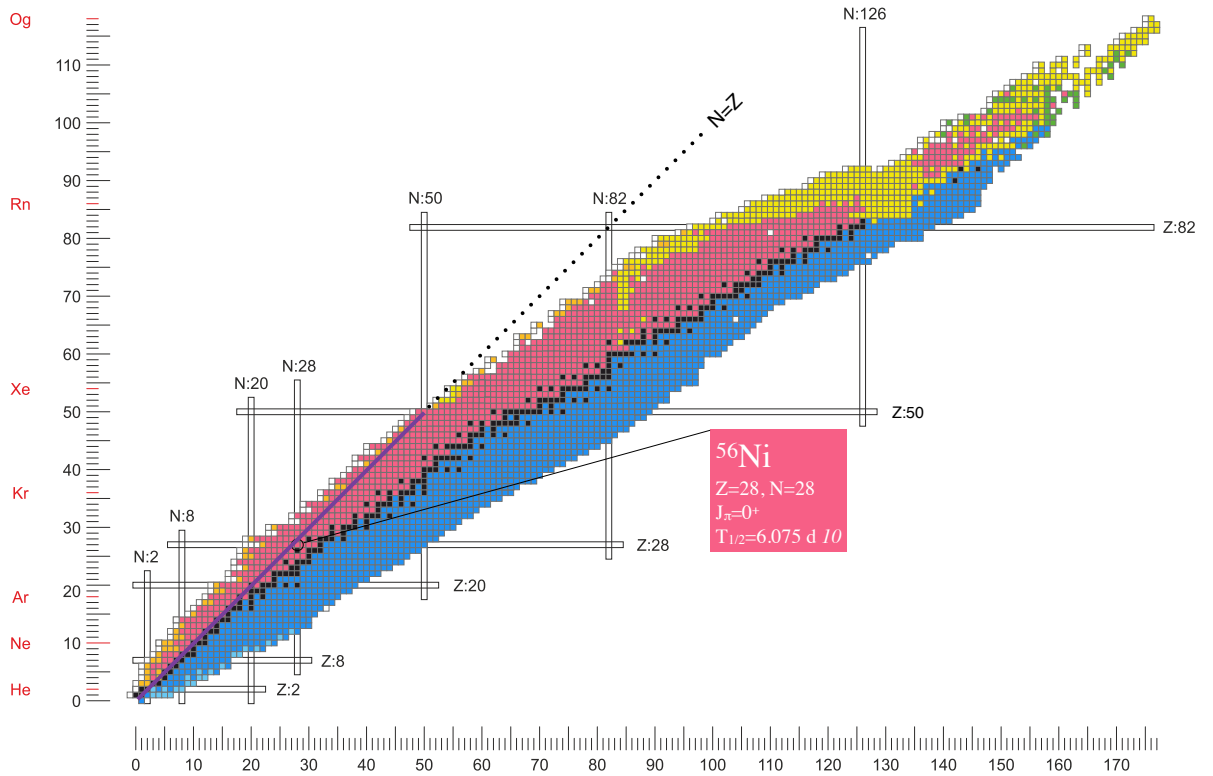


Figure 1.1: Nuclear chart classified as a function of the proton and neutron numbers. The valley of stability is represented in black and the different colors represent the different decay modes. Figure adapted from [2].

depending on the isospin of the pair. The Pauli principle plays also an important role in determining the total angular momentum (J) and the spin (S) of the pair.

Following this principle np pairs have states with either total angular momentum $J = 0$ and isospin $T = 1$ (isovector mode), or with $J = 1$ and $T = 0$ (isoscalar mode). Nevertheless, the concrete proof of the existence of the np isovector mode $T=1$, which should be similar to the $T=1$ nn and pp pairing due to charge independence, the characteristics of $T=0$ pairing are largely unknown.

The experimental study of the np pairing is a challenging task that relies on the strength of the physical observable. nn and pp pairing was evidenced through two-nucleon transfer reactions studies in the Pb and Sn isotopes. The two-nucleon transfer cross-section between the ground state of even-even nuclei and towards the 1st excited states reveals a vibrational-like behavior in the Pb isotope (closed shell isotopes) where the cross-section is proportional to the number of pairs. Whereas for the Sn isotopes (open shell nuclei) the cross-section is largely enhanced by a factor of about 25, showing a rotational behavior. By extension, the same effects are expected in the np-transfer reaction if np pairing develops in the $N = Z$ nuclei. The transfer reaction that we study will reveal information about the T=0 np pairing strength in the fp shell, due to the fact that it is particularly suitable for this study since only the $\Delta T = 0$ transition (transfer of a deuteron) is allowed.

Thesis Outline

In the following chapters the reader can find a detailed description of:

1. The theoretical motivation of the experimental studies of the $N = 28$ shell closure and the np pairing (Chapter 2).
2. The experimental Set-up used during the experiment in April 2014 in GANIL, France (Chapter 3).
3. The steps followed for the data treatment and analysis, as well as the post-experiment simulations that played an important role in the analysis (Chapter 4).
4. The results obtained from these studies, separated in two parts: the one-nucleon transfer analysis that was used to obtain the spectroscopic factors of the ground state and the excited states, and the two-nucleon transfer reaction, with which we investigate the T=0 isoscalar pairing mode (Chapter 5).
5. The conclusions of these studies can be found in the last chapter, as well as possible perspectives (Chapter 6).

2

Physics Motivations

Contents

2.1	Nucleon-Nucleon Interaction	13
2.2	Nuclear Shell Model	13
2.2.1	Mean-field potential and the spin-orbit term	15
2.2.2	N=28 shell closure	17
2.2.3	Single particle states via one-nucleon transfer	18
2.3	Pairing Correlations	23
2.3.1	Theoretical studies of np pairing	28
2.3.2	Experimental methods for the np pairing studies	28
2.3.3	Pairing via two nucleon transfer	30
2.4	Valuable experimental assets	36

2.1 Nucleon-Nucleon Interaction

The interaction between the nucleons in the nucleus can be described by two components:

- The nuclear one that acts between each nucleon, as a residual interaction originating from the strong interaction between the quarks that form the nucleons.
- A repulsive Coulomb part that acts between protons.

The most possible fundamental way to describe the nuclear part of the interaction would be to solve the corresponding QCD equations. However, it is not possible to use a perturbative development and for that reason we make use of an effective nucleon-nucleon interactions.

However, by considering symmetries of the interactions we constrain the expression of the nuclear interaction that can be decomposed in two terms:

- the local part, that contains the central and the tensor forces,
- the non-local part of the interaction, which mostly corresponds to the two-body spin-orbit term

There is some unknown functions in the expression of these terms. An effective interaction will assume the expressions of these unknown function, using some parameters fitted to experimental data.

2.2 Nuclear Shell Model

By using an effective nucleon-nucleon interaction \hat{V}_{ij} as described in paragraph 2.1 we can approximate the exact nuclear Hamiltonian \hat{H} depicting the system as:

$$\hat{H} = \sum_i \hat{T}_i + \sum_{i<j} \hat{V}_{ij}, \quad (2.1)$$

where \hat{T}_i is the kinetic energy operator for a nucleon i . The Schrödinger equation to solve is then:

$$\hat{H}\Psi = E\Psi, \quad (2.2)$$

where Ψ the A-body wave function of the nucleus and E the associated energy. Solving this equation corresponds to an A-body problem. The difficulty to solve the many body problem mathematically rises the quest of a model that is able to describe the nucleus. The success of the

atomic shell model as it was introduced by Niels Bohr and adapted in quantum mechanics by Erwin Schrödinger naturally influenced the parallel tries of the description of the nucleus. In the case of the nuclear shell model the main hypothesis derives by considering in a first place that each nucleon moves independently in a mean-field describing the average interaction with the other nucleons and represented by a one-body potential $\hat{U}(i)$. This $\hat{U}(i)$ potential corresponds to the average interaction between the nucleons, called the *mean-field*. The Hamiltonian can be rewritten as:

$$\hat{H} = \sum_i \left[\hat{T}_i + \hat{U}(r_i) \right] + \sum_{i < j} \left[\hat{V}_{ij} - \hat{U}'(r_{ij}) \right] \equiv \hat{H}_0 + \hat{H}_R, \quad (2.3)$$

where

$$\hat{U}'(r_i) = \frac{1}{A} \hat{U}(r_i). \quad (2.4)$$

The latter form of Hamiltonian determines the conditions for the use of a potential, within the framework of which this potential should be such as:

$$\hat{H}_R = \sum_{i < j} \left[\hat{V}_{ij} - \hat{U}'(r_{ij}) \right] = \sum_{ij} \hat{V}_{ij} \quad (2.5)$$

which is called the *residual interaction*.

If the \hat{H}_R is **negligible** to the \hat{H}_0 then we can directly consider the Schrödinger equation of A independent nucleons in the mean-field \hat{U} :

$$\hat{H}_0 \Psi_0 = E_0 \Psi_0. \quad (2.6)$$

The solution Ψ_0 of this equation is given by a Slater determinant of A particles and can be obtained by diagonalizing \hat{H}_0 and filling all the A lowest energy states.

However most of the times, the \hat{H}_R is **not negligible** and then we can add a part of it by considering particle-hole excitation on Ψ_0 in a valence space. The inert core represents the nucleons that are assumed to interact only through the mean-field. At the opposite, the nucleons occupying an energy level in the valence space can interact with each other beyond the mean field approximation. Such an example is illustrated in Figure 2.1. The first column in this figure corresponds to the energy level filling of Ψ_0 , the two following ones correspond to 1-particle 1-hole (1p1h) excitation on Ψ_0 , while the two next ones correspond to 2p2h excitation on the Ψ_0 as well. In this figure the development goes up to 8p8h excitation as represented in the last column.

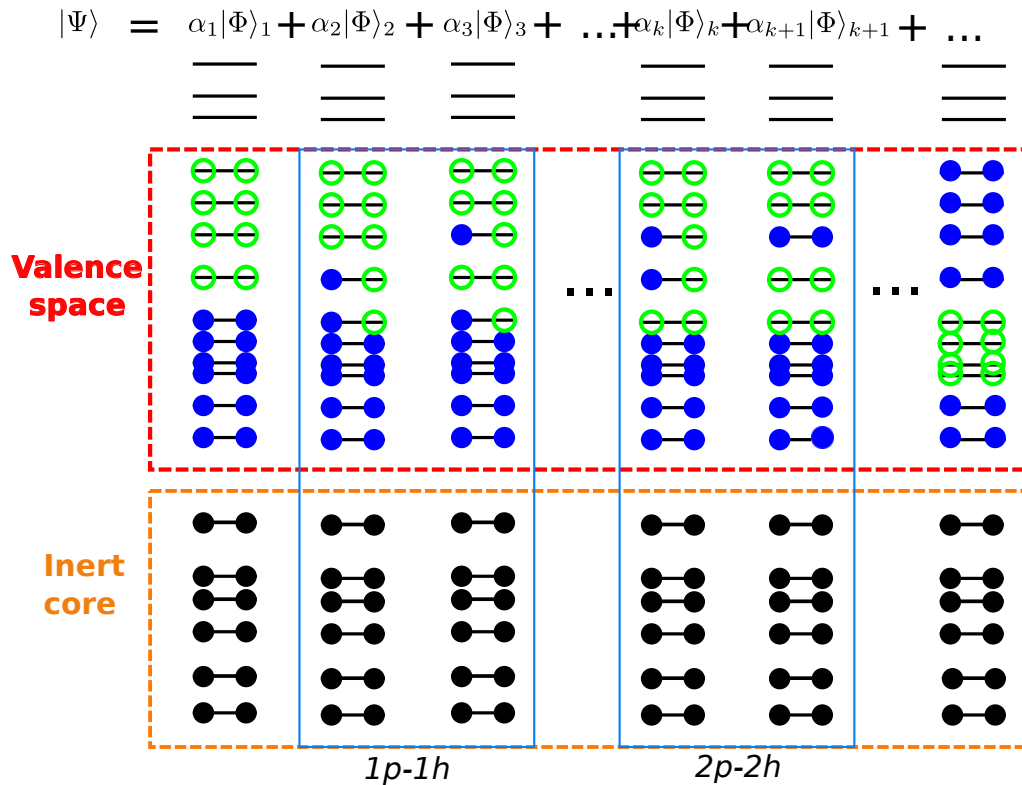


Figure 2.1: Illustration of the shell-model depicting the inert core and the valence space in the two cases of $1p1h$ and $2p2h$ excitation on Ψ_0 , N. Schunck

2.2.1 Mean-field potential and the spin-orbit term

Due to the fact that in stable nuclei there is a nearly constant nucleon density and that nuclear forces are short-range interactions we use an effective mean-field instead of calculating it from a nucleon-nucleon interaction. The mean-field is generally chosen to be a Wood-Saxon potential, or a harmonic oscillator. The nucleon orbitals that can be built from such a potential are shown in Figure 2.2, on the left and central columns.

Perhaps the most important prediction of the shell model is the existence of energy levels created by the gradual completion of the potential states. It was experimentally observed that shells of 50, 82 and 126 number of neutrons are particularly stable as well [5]. By using the harmonic oscillator, physicists can successfully describe these first *magic numbers*. Later, however, the fact that the model was not capable of reproducing the higher shell closures using simple potential wells was still not so convincing. The introduction of the spin-orbit term $\ell \cdot s$ that was proposed and studied independently by Maria Göppert-Mayer [6] and Haxel, Jensen and Suess[7]

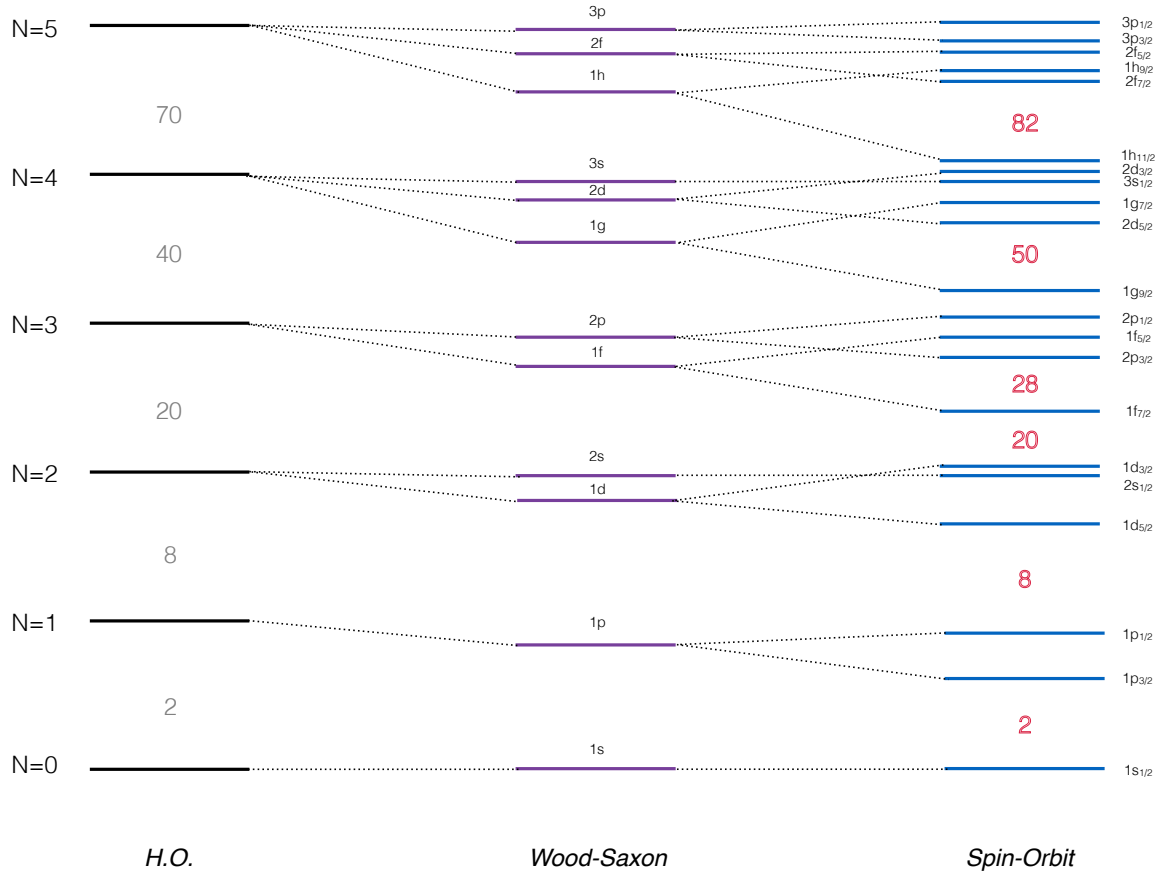


Figure 2.2: Orbital scheme from the single-particle Hamiltonian \hat{H}_0 , using a harmonic oscillator potential (left), a Woods-Saxon potential (center), and a Woods-Saxon potential plus the spin-orbit term (right).

during the 50's established the basic integrity of the nuclear shell model.

With the introduction of the spin orbit term a greater removal of the degeneracy was achieved. The energy now depends on three quantum numbers, the principal number n , the orbital angular momentum quantum number ℓ and the total angular momentum quantum number $j = \ell \pm 1/2$. The resultant single-particle levels are shown in the right column in Figure 2.2.

The predicted magic numbers correspond to orbitals with a large gap separating them from the next highest orbital. For the lowest levels, the spin-orbit splitting is sufficiently small that the original magic numbers, 2, 8, and 20 are retained. For the higher levels, the splitting becomes

important and the gaps now appear at the numbers 28, 50, 82 and 126. Besides predicting the correct magic numbers, the shell model also correctly predicts the spins and parities of many nuclear states.

The addition of this spin-orbit term adds also some questions about the effectiveness of the two-body interaction that we take into account, due to the fact that it fails to reproduce saturation properties of nuclei and spin-orbit magic numbers in specific nuclei [8]. The fact that we are limiting the two-body forces is probably the origin of this problem and the addition of a three-body term has been argued to give a better agreement with the experimental data [9]. One of the examples of the need of an addition of an effective interaction with a three-body term has been the reproduction of the first 2^+ state in ^{48}Ca .

2.2.2 N=28 shell closure

In the nuclear shell model, the magic number 28 is the first that appears after the introduction of the spin-orbit term. In addition, N=28 is a great choice to study nuclear forces as it involves nuclei having an intermediate mass and size, with orbits relatively well separated from the neighboring. According to the binding energies for ^{40}Ca and ^{48}Ca obtained by theoretical calculations [10, 11], a change in the $s_{1/2} - d_{3/2}$ splitting is expected from N=20 to N=28, but was found twice as small as experimentally [12] showing a significant change in the N=28 shell gap in the ^{48}Ca region.

Furthermore, the properties of the N=27 and N=29 isotones give further information about the N=28 shell closure. The structural evolution studied with N=27 isotones for ^{48}Ca is described in detail in the review paper of O.Sorlin and M-G. Porquet [12]. It is noted specifically that about 90% of the ground state configuration of the spherical ^{47}Ca nucleus corresponds to a neutron hole inside the $f_{7/2}$ shell (0p1h configuration) and a closed proton core (0p0h configuration). They presented a possible development of collectivity in the N = 27 isotones, by comparing the characteristics of their first states, as can be seen in Figure 2.3. The plot is showing the configurations of the ground and the first excited states which are displayed using a bi-dimensional representation, where the proton (neutron) configuration is shown on the y(x) axis. N_π (N_ν) gives the number of proton (neutron) excitation above the 0p0h (0p1h) core configuration and the size of the squares in the $N_\pi - N_\nu$ representation gives the intensity of each component.

The first excited state with $J^\pi = 3/2^-$ is expected to involve the promotion of one neutron in the upper $p_{3/2}$ shell with two neutron holes coupled in the $f_{7/2}$ shell (1p2h). This agrees with theoretical calculation showing that the strength lies mainly in the pure excitation of one neutron and less from three neutrons. This state, with closed proton configuration would be found well above the ground state of all the N=27 isotones, except if the N=28 shell gap is reduced and there is domination by the correlations. As it is shown in the same study it is the case for the

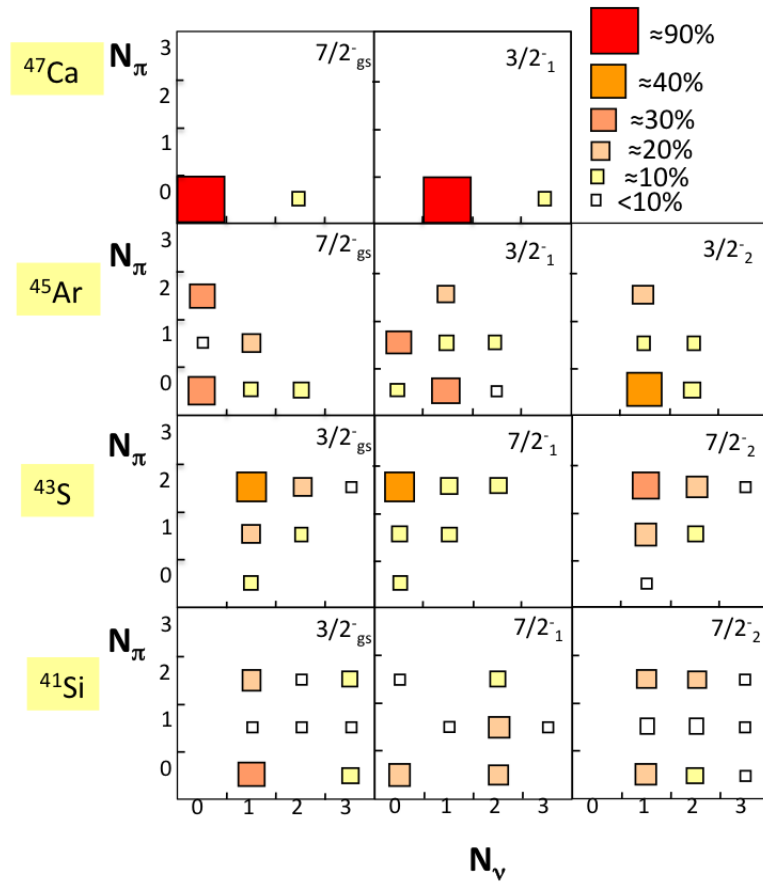


Figure 2.3: Squared wave functions of the first $7/2^-$ and $3/2^-$ states in the $N=27$ isotones represented in the proton (N_π) versus neutron (N_ν) particle-hole configuration plane, originally adapted from L. Gaudefroy [13] and presented in O.Sorlin [12]

$N=27$ isotones in the sd shell.

2.2.3 Single particle states via one-nucleon transfer

Due to the fact that $N = 28$ ^{48}Ca and ^{56}Ni are two doubly magic nuclei, both of them have the same sequence of levels, thus we do not expect any dependency of the protons. However, moving towards the fp shell and the ^{56}Ni , the interest of the shell evolution and the comparison with Ca isotopes arises. One-nucleon transfer reactions such as (d,p), (p,d) and (d,t) are one of the most direct ways to test the single particle configuration by measuring the occupancy of the nucleons in the $f_{7/2}$ orbits. In the closed-shell model for ^{56}Ni , these orbits will be completely

filled. Direct measurements of the spectroscopic factors of the neutron hole state in ^{56}Ni using the pickup (p,d) and (d,t) reactions will determine the robustness of the shell closure.

In the case of an open shell, the experimental data can be used to determine the measure of configuration mixing. More specifically, the evolution in between the $s_{1/2} - d_{3/2}$ particle orbitals and the 1p2h configuration corresponding to the $2p_{3/2}$ valence orbital will fulfill the picture of the N=28 shell evolution close to the stability. In addition, these information provide constraints to the ^{56}Ni core in shell model interactions and effective single particle energies.

The complementarity of the aforementioned one-nucleon transfer reactions can be used to draw the Fermi surface of the nuclei of interest. In the studies of ^{40}Ca and ^{48}Ca by Y.Uozumi *et al.* [14, 15] even if only the (d,p) reaction was measured they were able to investigate the Fermi surfaces, where the difference on the sharpness of the Fermi surface unravels information about the shell closure in the two nuclei. They express the nuclear surface by the Fermi distribution:

$$n(E_0) = \frac{1}{1 + \exp[(E_a - E_\lambda)/\Delta]} \quad (2.7)$$

The E_λ and Δ are being adjusted by least-square fitting to their experimental data. In Figure 2.4 while E_a corresponds to the binding energy, the resultant distributions are displayed by the solid lines. The values of the diffuseness parameter Δ result in 0.59 and 1.7 MeV for ^{48}Ca and ^{40}Ca , respectively. They conclude that the structure of ^{48}Ca is much harder than that of the ^{40}Ca nucleus. Since by means of the (d,p) reaction they study mostly the particle-states, the picture could be improved by measuring at the same time (p,d) and (d,p) or more easily (d,t) and (p,d) providing that we have the angular coverage. This can be done as well for ^{56}Ni as long as all the complimentary reactions are studied in the same experiment and information below and above the Fermi surface are obtained.

N=29 isotones

Obtaining the information above the Fermi surface requires the $^{56}\text{Ni}(d,p)^{57}\text{Ni}$ transfer reaction and the information emerging from the N=29 isotones. The discovery of ^{57}Ni was reported in the 1938 paper ‘‘Radio Isotopes of Nickel’’ by Livingood and Seaborg [16]. ^{57}Ni was observed at the University of California, Berkeley, by irradiating iron with 12.6 and 16 MeV α particles. Positrons and γ -rays were measured following chemical separation. Since then, many different experiments have been done for the identification of the levels and the extraction of spectroscopic information with different kind of methods [17, 18, 19, 20]. One of the interesting studies by means of transfer reaction in inverse kinematics is the work of K. E. Rehm *et al.* [21] where they measure the spectroscopic factors of the low-lying states in ^{57}Ni . Due to low statistics (Figure 2.5)

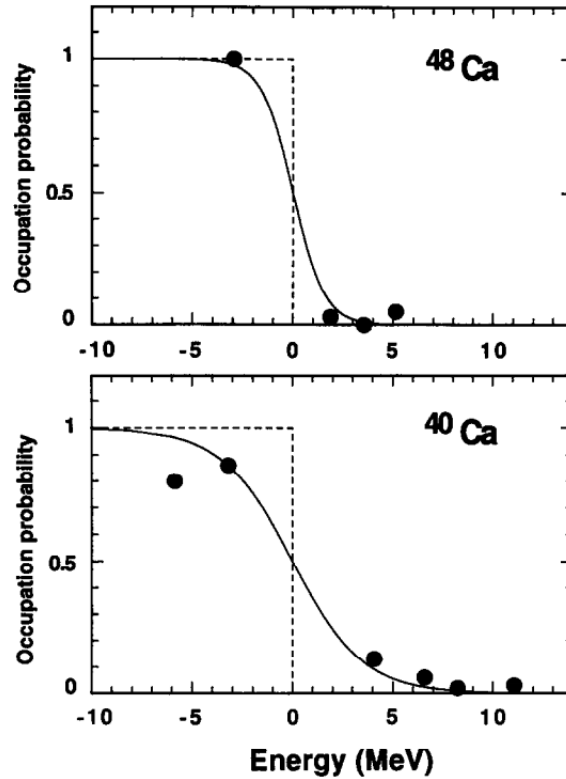


Figure 2.4: Occupation probabilities for neutron shells in ^{48}Ca (top) and ^{40}Ca (bottom). Black circles are the experimental results, and solid lines the Fermi distributions obtained from least-square calculations. [14, 15]

and lack of optical potential parameters for $^{56,57}\text{Ni}$ by the time, they conclude that the accuracy for determining the absolute spectroscopic factor is estimated to be about 50%. However, the low yields observed in the excitation energy region between 2–4 MeV, where higher-lying $1/2^-$, $3/2^-$, and $5/2^-$ states are expected, support the fact that the main single-particle strength for these low-spin states is concentrated in the first three excited states. With main focus of the experiment being the astrophysical interesting yield for the $^{56}\text{Ni}(d,p)$ reaction to the mirror nucleus ^{57}Cu , they solely conclude on the indication that these states in ^{57}Ni are indeed well characterized as the $2p_{3/2}$, $2p_{1/2}$, and $1f_{5/2}$ single-particle states.

N=27 isotones

Below the Fermi surface the information arises from the N=27 isotones and the $^{56}\text{Ni}(p,d)^{55}\text{Ni}$ or $^{56}\text{Ni}(d,t)^{55}\text{Ni}$ reactions. The discovery of ^{55}Ni came a bit later in 1972 by Proctor *et al.*[22].

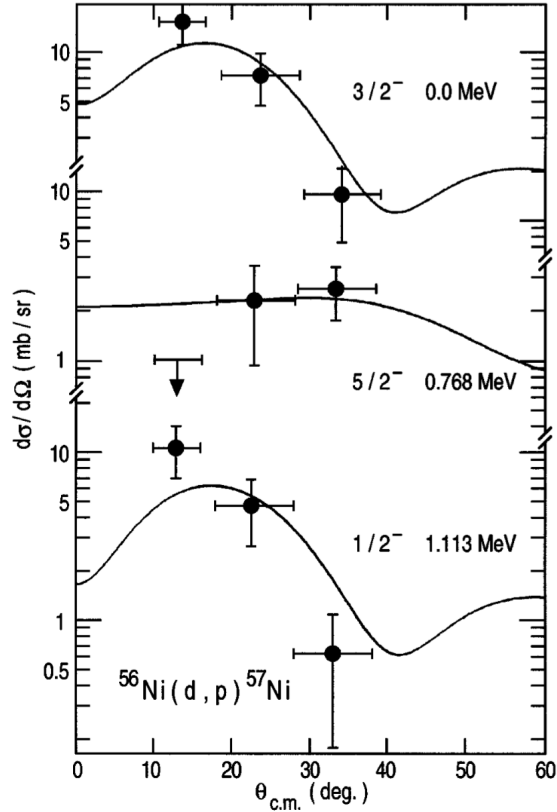


Figure 2.5: Differential cross-section as a function of the center-of-mass angle θ_{CM} for the three lowest states populated in the (d,p) reaction. The solid lines are the result of DWBA calculations with spectroscopic factors from shell-model calculations. [21]

The Michigan State University (MSU) sector-focused cyclotron accelerated ${}^3\text{He}$ to 65-75 MeV and the reaction ${}^{58}\text{Ni}({}^3\text{He}, {}^6\text{He})$ was used to produce ${}^{55}\text{Ni}$ [23]. The first time that excited states and high-spin rotational bands in the vicinity of the doubly-magic ${}^{56}\text{Ni}$ have been established was in 1998 in the work of D. Rudolph *et al.* [24]. Until latterly the only information around ${}^{55}\text{Ni}$ were coming from β -decay or isobaric analog states studies [25].

The most recent studies concerning the neutron spectroscopic factors of ${}^{55}\text{Ni}$ hole-states by means of the (p,d) transfer reactions have been performed in MSU by A. Sanetullaev *et al.* [26]. They extracted cross-sections for the (p,d) reaction in inverse kinematics using a high resolution array, micro channel plate tracking detectors and the S800 spectrometer. Their study has shown that, the measured spectroscopic factor (see section 2.4) for the ground state is equal to 6.7 ± 0.7 .

They conclude that this spectroscopic factor has a value less than the one expected for a closed $f_{7/2}$ shell in the independent particle model ($SF < 7$) even though it is within errors. Their results indicate a separation of about 3–4 MeV in between the sd and the fp shell. In total they extract the spectroscopic information for three low-lying states of ^{55}Ni assigning the two first excited states of ^{55}Ni (2.09 MeV and 3.18 MeV) to the $2p_{3/2}$ and $2s_{1/2}$ single particle states respectively. However, the fact that the low lying excited states are only a few hundreds keV away from each other increases significantly the difficulty to identify the single particle states by using only the particle information. Consequently, in that study they rely mostly on the information extracted from the database and shell model calculation performed.

They performed two kinds of calculations, shell model and ab-initio:

- For the shell model excitation energies of low lying $f_{7/2}$ and $2p_{3/2}$ relatively accurate calculations have been done in the fp valence space (PF) using the G-matrix based effective interaction, GXPF1A [27, 28]. On the other hand, to describe the $2s_{1/2}$ state it is required to take into account a valence space that mixes relevant sd (SD) with fp orbitals.
- In addition, they performed calculations with ab-initio self-consistent Green's function (SCGF) theory [29]. In this way it is possible to estimate the separation energies and the spectroscopic factors of quasi-hole states away from the major shells.

In this work, particle- γ coincidence will provide additional information for the populated states of ^{55}Ni nucleus. The information about the excited states of ^{55}Ni is limited, thus the data from the current experiment may identify and characterize the excited states that are populated by the (p,d) and (d,t) transfer reaction. The results are compared with the aforementioned calculations (shell model and ab-initio).

2.3 Pairing Correlations

Until now we studied the NN interaction by taking into account the particle-hole configuration. There is another part involved in the NN interaction and it is the short range correlations. Many experimental evidences showed that there was a need to add another kind of correlation in between the nucleons and it has been attributed to the *pairing correlations*. The experimental evidences were the following:

Energy gaps: There is a difference in the energy levels of deformed even-even and even-odd nuclei. For the even-even there are a few collective levels in lower energies and the rest of the states lie in higher energies (Figure 2.6). In the contrary the even-odd nuclei have collective levels and single particle states in the same energy interval.

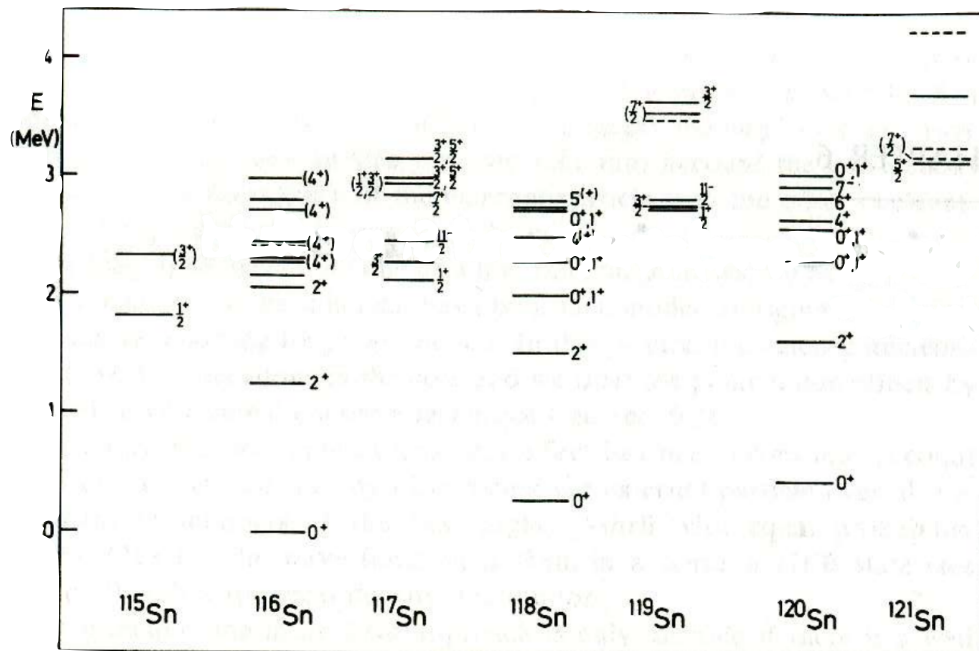


Figure 2.6: Example of excitation spectra of ^{50}Sn isotopes. [30]

Level densities: If a small number of nucleons occupy a given j-shell, there can be many states with energetically degenerate corresponding to various possibilities of the angular momentum.

The number of states per energy unit can be estimated and it emerges that at low lying excitation region the level density overcomes the one measured experimentally by almost two times.

Odd-even effect: We call the odd-even effect the fact that the even-even nuclei are more bound than the even-odd nuclei. The arithmetic mean of the binding energies of two even-even nuclei is larger than the total binding energy of the even-odd neighbor. In Figure 2.7 one can see that the binding energies of the even-even nuclei are always higher than the even-odd ones.

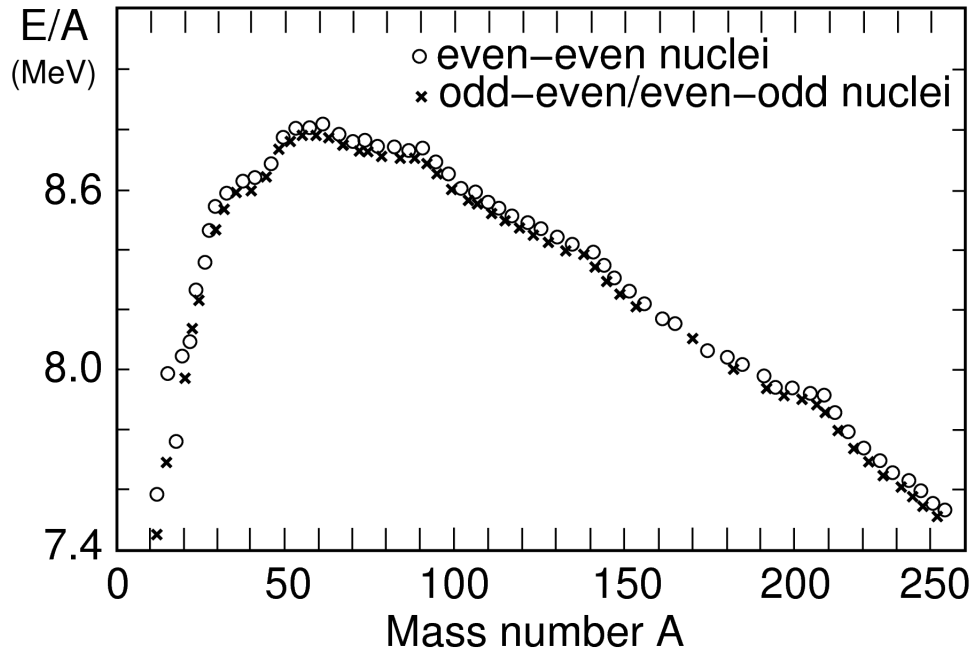


Figure 2.7: Binding energy per nucleon for the most beta-stable isobars (adapted from [31]).

Moments of inertia: The moments of inertia of deformed nuclei measured experimentally differ by factor of two from theoretical calculations that take into account only single particle states. If we add the pairing correlations theory and experiment are in a better agreement.

Deformation: It has been observed that conversely to what it was expected by pure shell model calculations the spherical nuclei do not appear only at the shell closure but also at nuclei whose mass does not deviate much from the shell closure. In addition, while a smooth transition was expected, there is a region in which we observe a rapid change in deformation. The peak of this phenomenon being the middle of the shell.

Low lying 2^+ states: For nuclei that are near closed shells a low lying state with angular momentum 2 and positive parity has been observed. The character of this levels cannot be explained as rotational or single particle excitation. A vibrational character has been attributed

to them which strongly involves the pairing phenomena [30, 32].

The nucleons have spin $s = 1/2$. In the case of a pair of two nucleons the total spin should be:

$$\vec{S} = \vec{s}_1 + \vec{s}_2 = \frac{1}{2}(\vec{\sigma}_1 + \vec{\sigma}_2) \quad (2.8)$$

where $\vec{\sigma}_1$ and $\vec{\sigma}_2$ the Pauli matrices. We note as $S(S+1)$, the eigen values of \vec{S}^2 and M_S are those of S_z and the values of S that we have are $S=0$ and $S=1$, with $|M_S| \leq S$. The states that commute to \vec{S}^2 and S_z are the states $|SM_S\rangle$ which are expressed according to the states $|1/2 m_1 1/2 m_2\rangle$ of the spin states of each nucleon. By replacing the states $|1/2 m_1 1/2 m_2\rangle$ with "spin up" and "spin down" we end up in the following configuration with respect to the Pauli principle:

$$\begin{aligned} |0 0\rangle &= \frac{|\uparrow\downarrow\rangle - |\downarrow\uparrow\rangle}{\sqrt{2}} \\ |1 1\rangle &= |\uparrow\uparrow\rangle \\ |1 0\rangle &= \frac{|\uparrow\downarrow\rangle + |\downarrow\uparrow\rangle}{\sqrt{2}} \\ |1 -1\rangle &= |\downarrow\downarrow\rangle \end{aligned} \quad (2.9)$$

The state $S = 0$, is called spin singlet and is anti-symmetric in the exchange of particles 1 and 2, whereas the state $S = 1$, is called the spin triplet and is symmetrical in this exchange.

In the same way by taking into account the isospin of the nucleons, the total isospin of the pair is equal to $\vec{T} = \vec{t}_1 + \vec{t}_2 = \frac{1}{2}(\vec{\tau}_1 + \vec{\tau}_2)$. We note as $T(T+1)$, the proper values of \vec{T}^2 and M_T are those of T_z and the values of T that we have are $T = 0$ and $T = 1$, with $|M_T| \leq T$. The states that commute to \vec{T}^2 and T_z in this case are the states $|TM_T\rangle$ which are expressed according to the states $|1/2 t_1 1/2 t_2\rangle$ of the spin states of each nucleus. By replacing the states $|1/2 t_1 1/2 t_2\rangle$ with $|nn\rangle$, $|np\rangle$, $|pn\rangle$ and $|pp\rangle$ we get the possible pair configuration:

$$\begin{aligned} |0 0\rangle &= \frac{|np\rangle - |pn\rangle}{\sqrt{2}} \\ |1 1\rangle &= |nn\rangle \\ |1 0\rangle &= \frac{|np\rangle + |pn\rangle}{\sqrt{2}} \\ |1 -1\rangle &= |pp\rangle \end{aligned} \quad (2.10)$$

A graphical representation of the two possible pairing channels can be seen in Figure 2.8. The channel which corresponds to isospin $T = 1$ is called *isovector* and the one with $T = 0$ is called *isoscalar* [33]. While in the $T = 1$ channel the np pairs are expected to be formed in a same way

to the nn and pp pairs due to charge independence, the $T = 0$ np pairs are largely unknown. However, there are strong evidences that this latter channel has a large strength as the only bound $A=2$ nucleus is the deuteron with a ground state $J=1^+$, $T=0$, while nn and pp pairs do not have any bound state. Figure 2.9 presents the evolution of the matrix element with two bodies (a pair of nucleons) as a function of the angle θ between the projections j and the total angular momentum J of each of the nucleons of the np pairs as studied by Molinari *et al.* [34] and Schiffer and True [35].

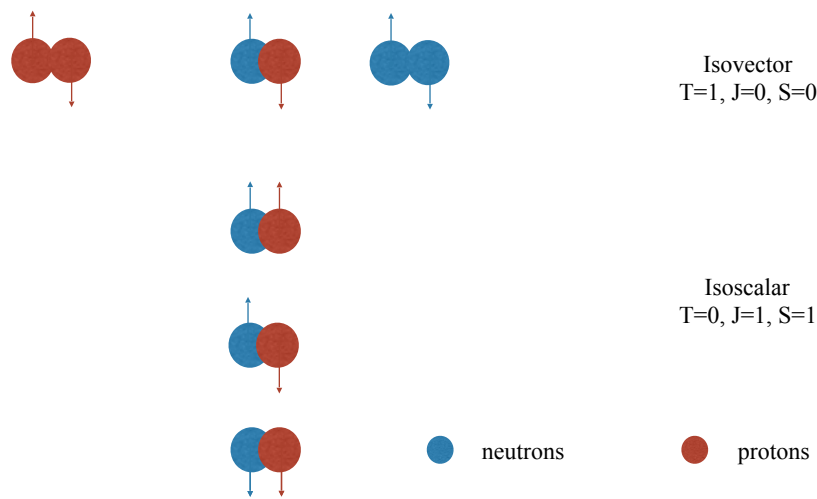


Figure 2.8: Graphical representation of the possible NN pairs. The arrows represent the spins of the nucleons. While with T , S and J are noted the quantum numbers of the pair.

We observe different behaviors of the $T = 0$ and $T = 1$ np pairing depending to the total angular momentum J . As expected from a short range interaction, the favored angular momenta are $J=0$ for $T=1$ pairs and $J=1$ or $J=J_{max}$ for $T=0$ pairs. The isovector pairing is maximum for $J = 0$ ($\theta = 180^\circ$) while the isoscalar pairing is maximum $J = 0$ ($\theta = 180^\circ$) but also when the spins are aligned at $\theta = 0^\circ$, as shown in Figure 2.9.

There are still many open questions about the $T=0$ channel. Although the maximum aligned pairs with $J=J_{max}$, $T=0$ are of interest, we focus here on the $J=1$, $T=0$. And while there are experimental evidences of a strong pairing force in the $T=0$ channel, the question remains for whether or not a correlated state can be formed. This correlated state would be in analogy to

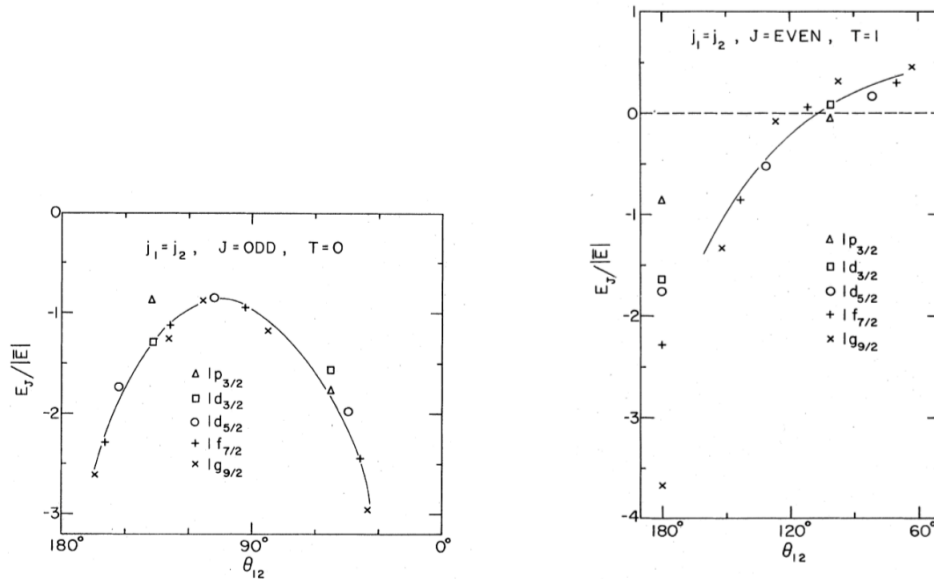


Figure 2.9: A pairing matrix element as a function of the isospin of the np pair and the angle between the projections j of the total angular momenta J of each of the nucleons of the pair np ($\theta = 180^\circ, J_{pair} = 0$ and $\theta = 0^\circ, J_{pair} = 2j$) adapted from [36], originally from [35].

pair phase of superconductors and superfluids. This is why Bohr, Mottelson and Pines [37] and Belyan successfully applied the methods of the theory of superconductivity developed by Barden, Cooper and Schieffer [4] to the nuclei.

Far from the thermodynamic limit, one has to use these definitions carefully. In fact, as simple models and general arguments indicate, the control parameter that originates the transition between a normal system and a correlated pair depends not only on the strength of the pairing force G but also on the available degeneracy $\Omega = j + 1/2$ (number of pairs) and the single particle spacing D , usually expressed as $G\Omega/D$. In a mean-field approach there is a pairing-field and a correlation energy associated.

In a microscopic system such as the nucleus the definitions provided by the macroscopic superconductivity can not have identical use. In this kind of small systems, the singularity of a phase transition fades away into an extended cross-over region. The beginning of such correlations appears with the presence of the pair vibration, which are further associated with the pair condensate of macroscopic superconductors.

For most nuclei, for which $N \neq Z$, the pairing manifests mainly by pp and nn pairs because there is a small overlap between the wave functions of protons and neutrons. On the other hand,

$N = Z$ nuclei are good candidates to exhibit np pairing. As pairing correlations depend on the degeneracy of the shell, nuclei populating high-j orbitals are required.

2.3.1 Theoretical studies of np pairing

There has been many years of theoretical studies, trying to explain the np pairing and the competition in between the two modes using different approaches and formalisms, with the main developments based on the shell-model and mean-field calculations. The most recent approaches try to include the np pairing in the Hartree-Fock-Bogoliubov theory by adding the isovector and isoscalar pairing modes [38]. In these prior studies for $N = Z$ and $N > Z$ even-even nuclei with $A > 50$, the isoscalar and isovector pairing appears, in the ground state. More recently, Bertsch and Luo [39] applied the Hartree-Fock-Bogoliubov theory to investigate the competition between isoscalar and isovector pairing in nuclei with $A > 100$. They conclude that for $N = Z$ nuclei with $A \approx 130-140$ close to the drip-line, the T=0 pairing would dominate. Similarly, some more recent studies [40], using a many-body model described by Bogoliubov–de Gennes equations and the same Hamiltonian as in [39], demonstrate that the condensate is a mixture of T=1 and T=0 pairing, which appears when the $N - Z$ imbalance grows, close to the proton drip line. Figure 2.10 shows the nuclear chart focused on the $N = Z$ line for $A=100$ nuclei. Most of the nuclei are dominated by T=1 pairing (green squares). Part of the $N = Z$ nuclei show pure T=0 pairing, while outside the $N = Z$ line some of the nuclei show a mixture of T=1 and T=0 states.

In the meantime, while the studies of Macchiavelli *et al.* [41] around ^{56}Ni show collective behavior of the pairing vibrations, they can not conclude on manifestation of the isoscalar mode collectivity. Later, Yoshida [42] demonstrated that low-lying 1^+ states in odd-odd $N = Z$ nuclei can be a precursory soft mode of the T = 0 pairing condensation.

Despite many years of np pairing theory, the subject is yet under debate because of the inconclusive experimental evidences.

2.3.2 Experimental methods for the np pairing studies

There are several methods to study np pairing and can be briefly described as follows:

Binding Energies: If one considers a nucleus A, with a ground state that is a pair condensate and adding gradually pairs, the increase in the binding energy will correspond to the pairing energy if these pairs contributing to the correlations of the nucleus A. The gain in energy is considered to be proportional to the number of pairs. In the case that the pairs do not interfere with the other correlations in the nucleus then there should be no gain in energy. The reduced energy corresponds to the reduced pairing energy. The results from this phenomenological approach

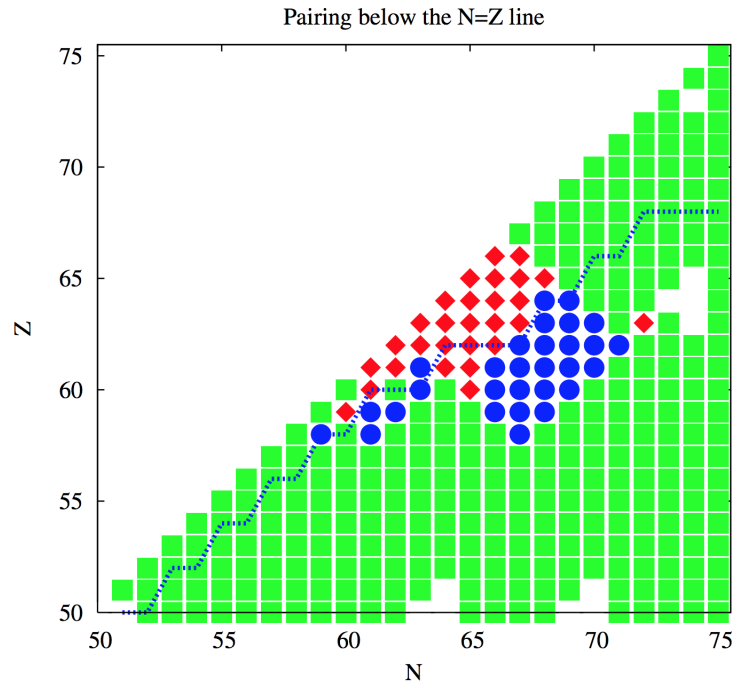


Figure 2.10: Competition between isoscalar and isovector pairing in heavy, very proton-rich spherical nuclei, assuming a ratio $3/2$ for the respective interaction strengths and a Woods-Saxon spin-orbit potential. Green: Isovector condensate, red: isoscalar condensate, blue: coexistence of both condensates, from [40]

show full isovector pairing evidences, which by taking into account the charge independence of the nuclear force was to be expected [43].

Rotational Properties: From early on it has been observed that pairing reduces the moment of inertia of deformed nuclei. The variation of the moment of inertia with the angular momentum provides information about the strength of the pairing fields. Experimental studies focus on the ground state rotational bands of $N = Z$ nuclei and their angular momentum, in regions where rotational alignment is expected. The “delayed alignment” then can be associated with np pairing correlations [44]. The results from these experiments are in agreement with the $T=1$ cranking model. [45]

Spectroscopy: By using the spectroscopy of ^{92}Pd , Cederwall *et al.*[46] have deduced a spin-aligned, isoscalar neutron proton coupling scheme. They interpreted that the obtained level scheme emerges from the strong attractive interaction between $g_{9/2}$ neutrons and protons in aligned angular momentum ($J = 9$) coupling. With $J=9$ the isoscalar pairing revealed in ^{92}Pd is

different from the predictions of a BCS type of isoscalar np pairing condensate in $N = Z$ nuclei, the state is strongly correlated but it is not considered as pairing itself.

Deuteron transfer reaction: In the case of two nucleon transfer reaction by depositing or picking up a np pair at the same point in space we have in hand a specific tool to probe the amplitude of this collective motion. The transfer amplitude $\langle A+2|a^+a^+|A \rangle$ is analogous to the reduced transition probabilities BE2's in the quadrupole case. The pairing correlations result in a constructive interference of reaction amplitudes giving a enhanced two-nucleon transfer. This is the method chosen in this work to study the np pairing. We will detail it in the next paragraph.

2.3.3 Pairing via two nucleon transfer

Two nucleon transfer reaction provides a powerful tool to study pairing. To study the neutron-proton pairing by this method, we transfer np pairs. The enhancement of deuteron transfer reactions by np pairing was first addressed by Fröbrich [47] who predicted an increase of ≈ 2.5 in the cross-section over the single-particle estimate. Additionally, the transfer operator of a deuteron pair should enable the measurement of the collectivity in the case of the presence of pairing. This enquiry will test the phase transition of the nucleus from a phase of independent particles to a superfluid phase.

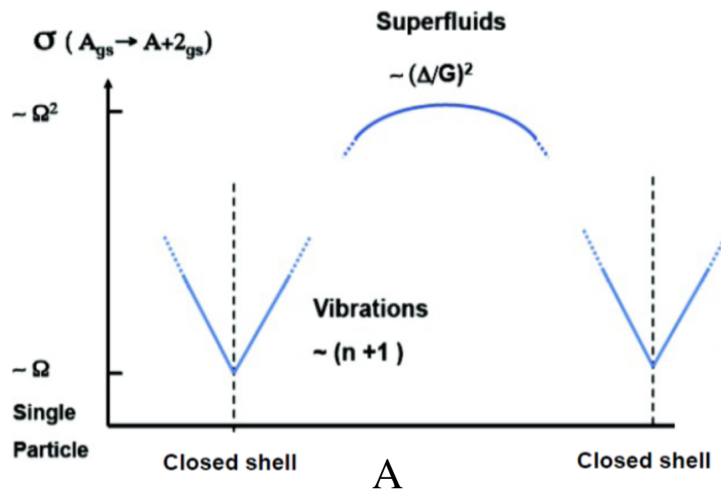


Figure 2.11: Schematic diagram describing the behavior of the 2-nucleon transfer cross-sections in between two closed shells. [36]

A graphical representation of the two-nucleon transfer cross section between the ground states

of an initial nucleus with A nucleons and a final one with $A+2$ nucleons, in the presence of pairing correlations going from a closed shell to the next one, is described in Figure 2.11. In this figure one observes that near the closed shells, the cross section has a linear behaviour, proportional to the number of pairs and it is described by a harmonic vibrational pattern. Furthermore, the cross section lies closer to the single particle limit and is proportional to the number of phonons with an enhancement of the order of the single particle degeneracy Ω . While adding pairs and reaching the mid-shell, there is a rapid change that can be described by a BCS type of state closer to the superfluid limit. The cross-sections become now almost constant and increased by Ω^2 , of the order of $(\Delta G/2)$. Thereby, we expect a parabolic shape for the systematic of the two nucleon transfer cross-section from one closed shell to the next one.

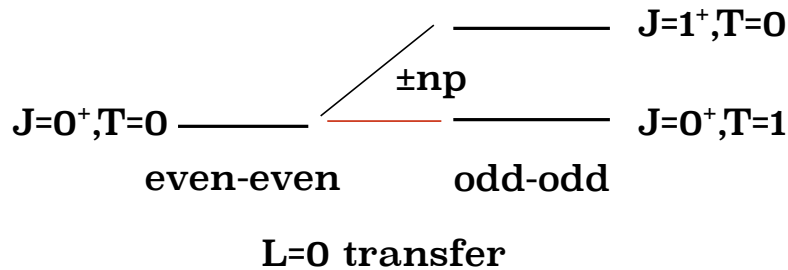


Figure 2.12: Schematic diagram depicting the use of two-particle transfer (np) reactions to study np correlations.

As discussed earlier, the rapid quenching of np pairs as one moves away from $N = Z$ suggests that the addition or removal of an np pair from a self-conjugate even-even nucleus the lowest 0^+ and 1^+ states in odd-odd self conjugate nuclei (Figure 2.12) stands out as the best tool to study np pairing correlations. More recently, Van Isacker *et al.* [48] studied the effect in the framework of the IBM model and independently concluded that the transfer intensities should reflect the nature of the ground state condensates. The Table 2.1 shows the amplitudes of the direct transfer of a np pair in the case where the projectile is an even-even or an odd-odd nucleus. The value x corresponds to the relative intensity between the $T=0$ and $T=1$ pairing. When $x = 0$ it corresponds to purely isoscalar pairing, when $x = 1$ the relative intensity corresponds to purely isovector. In the case of $x = 0.5$ the ground state of the odd-odd nuclei $N = Z$ would be $T = 0$. Thus, for nuclei where $A > 40$, it is more likely to correspond at $x > 0.5$. To be able to study both the channels of np pairing, it is more suitable to use even-even nuclei.

With ^{40}Ca being the last stable $N = Z$ nucleus, the transfer reactions for higher masses

Relative Intensity	Reaction	$C_{T=0}^2$	$C_{T=1}^2$
x=0.5	EE \rightarrow OO $_{T=0}$	$1/2(N_b + 6)$	0
	EE \rightarrow OO $_{T=1}$	0	$1/2(N_b + 6)$
	OO $_{T=0} \rightarrow$ EE	$1/2(N_b + 1)$	0
	OO $_{T=1} \rightarrow$ EE	0	$1/2(N_b + 1)$
x=0	EE \rightarrow OO $_{T=0}$	$N_b + 3$	0
	EE \rightarrow OO $_{T=1}$	0	3
	OO $_{T=0} \rightarrow$ EE	$N_b + 1$	0
x=1	EE \rightarrow OO $_{T=0}$	3	0
	EE \rightarrow OO $_{T=1}$	0	$N_b + 3$
	OO $_{T=1} \rightarrow$ EE	0	$N_b + 1$

Table 2.1: Table summarizing the np pairs transfer amplitudes according to whether the projectile is an even-even (EE) or an odd-odd (OO) nucleus. Where $x = 0$ corresponds to a purely isoscalar pairing, $x = 1$ in the case where it is purely isovector and $x = 0.5$ in the case where the pairing is both isoscalar and isovector. N_b is the number of bosons (number of pairs) [48].

have to be studied in inverse kinematics as required for radioactive beams. Following from the argument that larger single-particle degeneracies Ω provide a better opportunity to develop collective effects, as a consequence, the perfect nucleus for studying np pairing would have been ^{92}Pd for instance and the corresponding $g_{9/2}$ shell. Even if the development of radioactive beams gave us the ability to gain ground on the nuclear chart it is still not possible to study these nuclei by means of transfer reactions. The reason is that the current intensities of the radioactive beams can not provide the sufficient particles per second ($\approx 10^4$) in order to achieve this study by using transfer reactions.

Until now the relative ratios for the sd shell nuclei were obtained by different experiments performed in earlier decades under different conditions, making it difficult to have a clear picture. For this reason recent studies have been performed at RCNP Osaka. Y.Ayyad *et al.* have measured (^3He , p) and (p, ^3He) transfer reactions in direct kinematics with ^{24}Mg , ^{28}Si , ^{32}S and ^{40}Ca [49]. The ratios of the cross-sections of this experiment in addition with all the previous measurements obtained from the literature & ENSDF can be seen in Figure 2.13. The new measurements presented with the open diamonds show that by adding or removing a pair the relative ratio of the two channels has approximately the same order of magnitude. These results have smaller values than the (p, ^3He) results from previous measurements and as the authors mention the experimental ratios do not show a clear trend with the number of valence particles. In addition, it is noted that for few cases, the deviation from the single particle limit shows a dominance of the cross-section populating the 1^+ state.

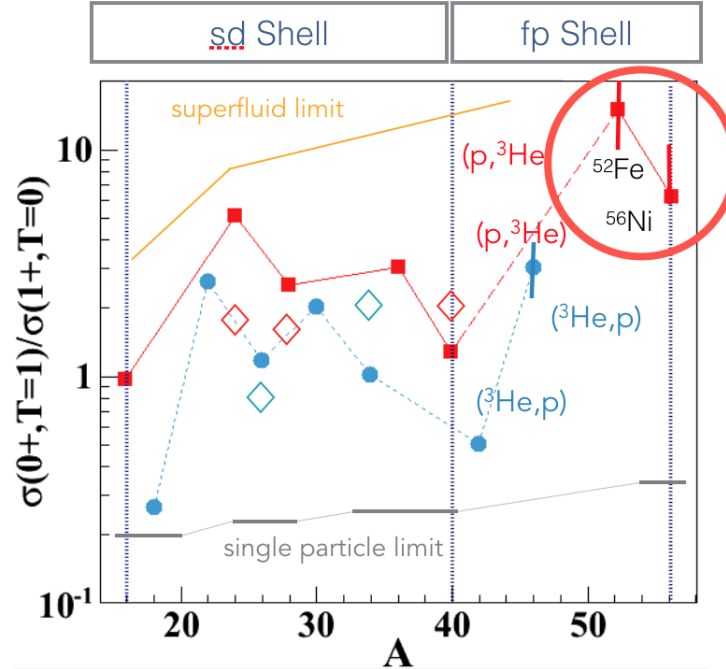


Figure 2.13: Systematics of the ratio of the cross-sections of the T=1 over the T=0 pairing in the *sd* as well as in the *fp* shell. The results derived from our experiment lie on the closure of the *fp* shell indicating dominance of the isovector pairing.

In Figure 2.13 one can also see first measurements by means of a radioactive beam in the *fp* shell. Preliminary results are presented in Figure 2.13, showing the first result by A.O. Macchiavelli *et al.* for ^{44}Ti measured in Argonne with ATLAS.

This experiment

In order to progress in the understanding of the *np* pairing, the study of $^{56}\text{Ni}(p, ^3\text{He})$ and $^{52}\text{Fe}(p, ^3\text{He})$ reactions has been performed in GANIL. This is sensitive to both types of *np* pairing populating $\Delta T = 0, 1$. The analysis of the $(p, ^3\text{He})$ reaction has been performed by B. Le Crom in his thesis [50]. The results can be seen in Figure 2.13 in a red circle adding the information in the shell closure of the *fp* shell. In the $(p, ^3\text{He})$ reaction, the ratio of the population of the T=0 and T=1 states indicates a predominance of T=1 pairing. Additionally, the cross-section to the T=0 state in the *fp* shell is much lower than in the *sd* shell. This is in agreement with

the theoretical predictions that the spin-orbit hinders the $T=0$ pairing in the fp shell. From this measurement, it was possible to extract the angular distribution of the ground state of ^{54}Co assuming no contribution from the 7^+ isomeric state (Figure 2.15).

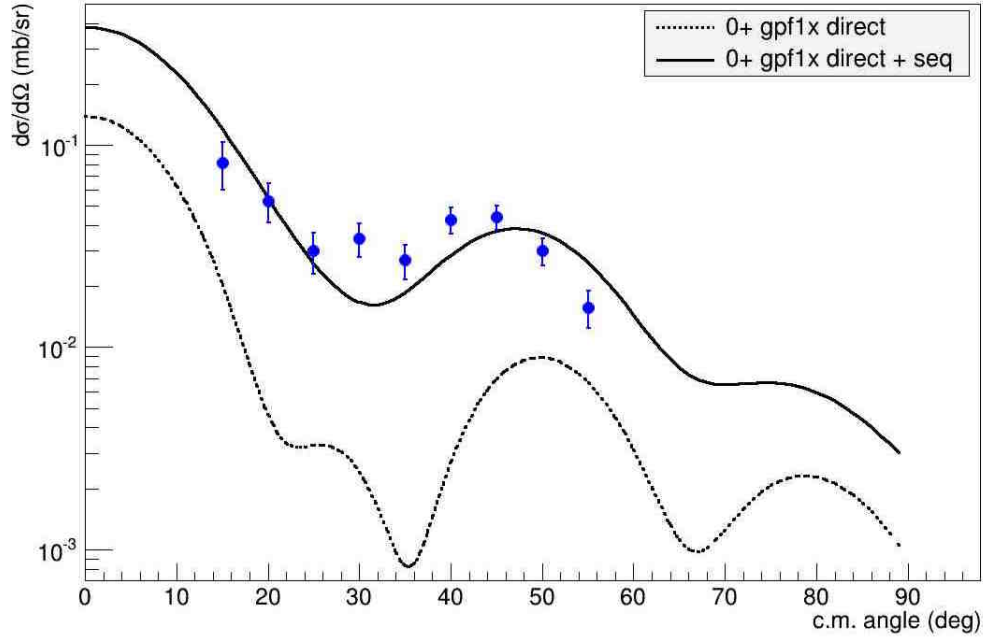


Figure 2.14: Angular distribution for the transfer to the ground state of ^{54}Co . [50] The experimental points are in blue. The dotted curve is derived from the calculation considering only a direct transfer. The calculation results considering only a sequential transfer are represented by the red curve. The black curve represents the results from the calculation taking into account both the direct and sequential transfer. The spectroscopic factors used were calculated with GXPF1J interaction by T. Suzuki and H. Sagawa.

The angular distributions are needed to understand more deeply the reaction mechanism for each channel. *Distorted Wave Born Approximation* (DWBA) calculations have been performed for the ground state of ^{54}Co and show that the sequential transfer is dominant over the direct transfer Figure 2.14. However according to G. Potel *et al.* [51], the correlations are kept during the transfer process and information of the pairing correlation can be obtained. From these data, it was impossible to extract the angular distribution for the $T=0$ state due to a cross-section that was very low ($\approx 10\mu\text{ b}$) and a high density of states.

In this thesis the $^{56}\text{Ni}(d,\alpha)$ reaction that is selective in $\Delta T=0$ will be investigated. This measurement was performed during the same experiment. With its selectivity in $\Delta T = 0$ the analysis of the (d,α) reaction may:

- distinguish clearly the $T=0$ states and help us to obtain its cross-section
- determine the contribution from the $T=0$ isomeric state as no ground state contribution is expected in this case. In that way it is possible to verify the measured ratio from the $(p, {}^3\text{He})$ reaction, due to the fact that no contribution of the isomeric state was taken into account.

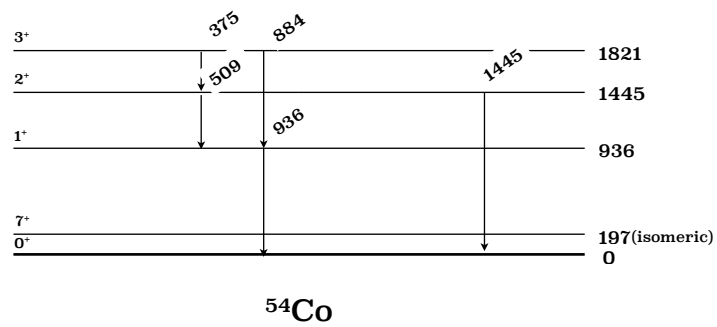


Figure 2.15: Level scheme of ${}^{54}\text{Co}$ obtained by NNDC [52]

2.4 Valuable experimental assets

Reaction kinematics

To simplify the problem when presenting the valuable experimental measurements we still use the direct kinematics description as a system of reference. From the energy and momentum conservation we are able to draw the two body kinematics that reveal all the information about the residue nucleus (4) of interest. This is feasible since we are measuring the momentum p_3 and we know the mass m_3 of the second outgoing particle(3). Then, we can use the relation:

$$E_4 = \sqrt{E_4^2 + p_4^2 c^2 - m_4^2}, \quad (2.11)$$

where

$$E_4 = \sqrt{T_1 - m_1 + m_2 - (T_3 + m_3)} \quad (2.12a)$$

$$p_4^2 = p_1^2 + p_3^2 - 2p_1 p_3 \cos\theta. \quad (2.12b)$$

The p_1 and $m_{1,3}$ are known and $T_{1,3}$ can be obtained by $T = \sqrt{(2m + p)p}$. The method of reconstructing the missing mass and consequently the energy spectra is called the *missing mass* technique [1]. In the case that the nucleus of interest is not measured, all the bound and unbound states can be measured in the same way. This technique is one of the most used techniques nowadays for the spectroscopy of the unbound states.

Angular Distribution and ℓ reaction matching

A nucleon transfer is a quantum process during which a quantized angular momentum is transferred. The differential cross section to a given final state, as a function of the scattering angle, shows an oscillation pattern whose structure depends on the transferred angular momentum. For simplicity, we assume a reaction in direct kinematics where a nucleon is removed from a target whose mass is considered infinite compared to the projectile and light residue, so that all the transferred angular momentum is taken away by the light particle. In a quantum system for which the angular momentum is a good quantum number, the operator \hat{L}^2 commutes with the Hamiltonian and its application to the nucleus wave function gives

$$L^2|\Phi\rangle = \ell(\ell + 1)\hbar^2|\Phi\rangle \quad (2.13)$$

In the classical limit of a transfer reaction occurring at the surface of the nucleus, the trans-

ferred momentum in the reaction is given by $L = p_{\perp} \hat{R}$, where p_{\perp} is the transverse momentum of the scattered particle and R is the distance between the two at grazing, leading a non-relativistic approximation

$$p_{\perp} \hat{R} = \sqrt{\ell(\ell + 1)} \hbar. \quad (2.14)$$

In the infinite mass target approximation, the perpendicular momentum of the light recoil can be approximated to $p_{\perp} = p \sin \theta_o$. Under these approximations, the scattering angle (the first maximum of the cross section) is given by

$$\theta_o = \arcsin \frac{\sqrt{\ell(\ell + 1)} \hbar}{pR} \quad (2.15)$$

Intuitively, the beam velocity will impact strongly the population of states depending on the transferred angular momentum they imply. The optimum population of given states requires momentum matching imposed by equation 2.14.

Spectroscopic Factors

The spectroscopic factors relate a given direct reaction with the nuclear structure. As spectroscopic factors we can theoretically describe the overlap of the wave function between a nucleus of A nucleons in an initial state $|\Psi_0^A\rangle$ and a nucleus with $A \pm 1$ nucleons in the final state $k|\Psi_k^{A \pm 1}\rangle$.

$$S_+ = \int |\langle \Psi_0^{A+1} | a^\dagger | \Psi_0^A \rangle| \quad (2.16)$$

$$S_- = \int |\langle \Psi_0^{A-1} | a | \Psi_0^A \rangle| \quad (2.17)$$

where a^\dagger is the creation operator and a is the annihilation operator, depending on if a nucleon is added or removed, respectively. By means of the spectroscopic factors we try to model the nucleus $A \pm 1$ as a core Φ_0^A plus a hole or a particle. It quantifies the description of a populated state in a transfer reaction as a single particle state. The spectroscopic factor is not an observable since it is not conserved through a unitary transformation, but it is an experimentally extracted quantity [53, 54]. It is obtained by the comparison of the theoretical cross section with the experimental one. In the case where only one orbital contributes in one state we get:

$$C^2 S_{exp} = \frac{\sigma_{exp}}{\sigma_{th}^S P} \quad (2.18)$$

With C^2 being the Clebsh-Gorban coefficient of the isospin, which takes into account the

possible difference between the initial and final state, and σ_{ih}^{SP} the theoretical cross section for a single particle transfer reaction. It is clear that C^2S_{exp} is dependant on the reaction model used to extract the theoretical cross section. In this work the *Distord Wave Born Approximation* has been used and it is thoroughly describe in section 5.1.6. Once the experimental C^2S_{exp} has been extracted it can be then compared to the theoretical one calculated within the shell model formalism as can be seen in the following chapters.

3

Experimental case

Contents

3.1	Experimental Overview	40
3.2	Secondary beam production at GANIL	40
3.2.1	Description of the LISE spectrometer	40
3.2.2	Secondary beam of ^{56}Ni	43
3.3	Beam Tracking Detectors: CATS	44
3.4	Charged particle detection	45
3.4.1	Silicon Strip Detectors	45
3.4.2	TIARA	45
3.4.3	MUST2	47
3.5	Recoil detection	50
3.5.1	CHARISSA telescope	50
3.6	γ-ray detection	50
3.6.1	EXO GAM	51

3.1 Experimental Overview

To probe the gap of $N=28$, we study the spectroscopy of the $N=27$, ^{55}Ni by the $^{56}\text{Ni}(d,t)^{55}\text{Ni}$ and $^{56}\text{Ni}(p,d)^{55}\text{Ni}$ one nucleon transfer reactions on ^{56}Ni , while to study the np pairing in the self-conjugate nucleus ^{56}Ni we have measured the two-nucleon transfer reactions $^{56}\text{Ni}(p,^3\text{He})^{54}\text{Co}$ [50] and $^{56}\text{Ni}(d,\alpha)^{54}\text{Co}$.

The experiment was performed in 2014 in Grand Accélérateur National d'Ions Lourds (GANIL), Caen. The radioactive beam of ^{56}Ni at 30 MeV/u was produced by fragmentation of a primary beam of ^{58}Ni and purified by means of the LISE3 separator. Measurements were performed in inverse kinematics on CH_2 and CD_2 targets. Two beam tracking multiwire proportional chambers (CATS) were placed upstream of the reaction target and yielded event by event the position and angle of the incoming beam particles.

The experiment included close to 4π coverage for the light charged ejectiles. The two components of the double sided silicon strip detector TIARA, Barrel and Hyball, were placed at central and backward angles. Four MUST2 telescopes covered the forward angles. Tiara and MUST2 provided the necessary parameters for extracting excitation energy and angular distribution. The kinematic lines of the recoiling light particles are shown on Figure 3.1 in the energy and angle plane for the reactions of interest. The angular coverage of the particle detection is also indicated.

Around the target 4 clovers of EXOGAM were used for particle- γ coincidences in order to identify the populated state of the residue and disentangle the excited states. At the end of the beam line the Si-Si-CsI telescope CHARISSA was placed to detect heavy residues (although it was not used in the current analysis).

The energy loss, residual energy, angle and time of flight were measured in order to perform particle identification. The experimental set-up is displayed in Figure 3.2.

3.2 Secondary beam production at GANIL

3.2.1 Description of the LISE spectrometer

The development of radioactive beam facilities has boosted the investigation of the exotic nuclei and vice versa [55]. RIKEN (Japan), GSI (Germany), GANIL (France), NSCL (Michigan, USA),

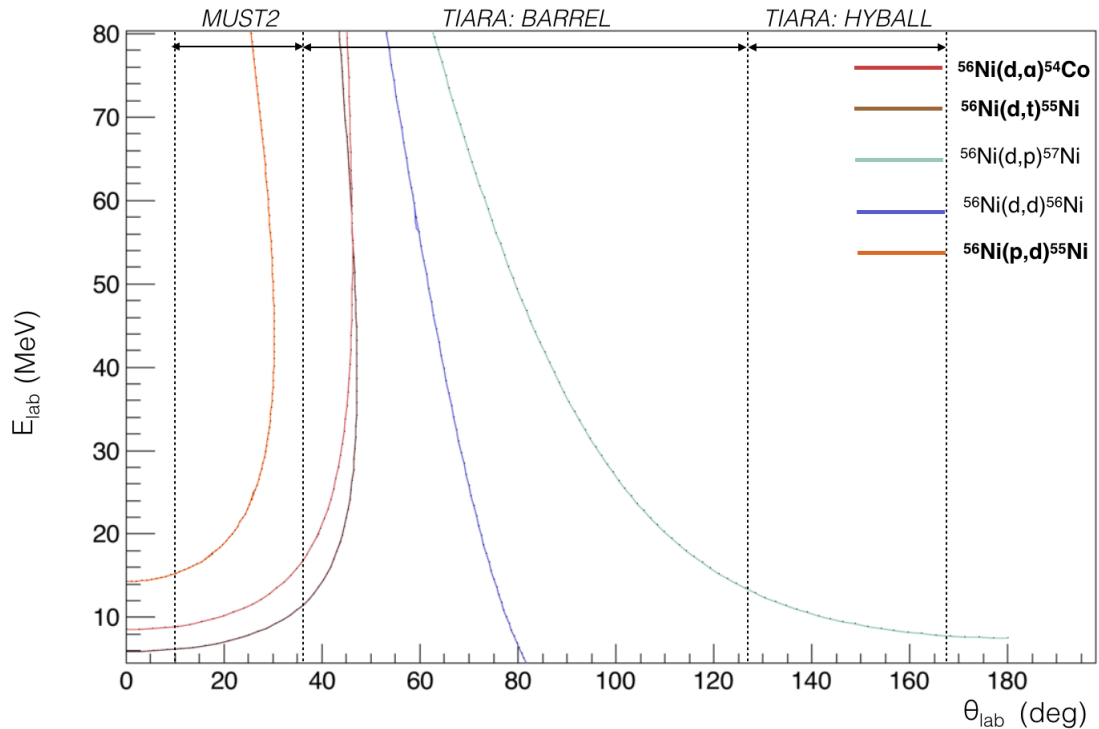


Figure 3.1: The Kinematic lines of the reactions of interest and the detector coverage

ISOLDE (CERN) are some of the most important facilities around the world. There are two different methods of producing radioactive beams in GANIL: the isotope separation on line (ISOL) technique and the in-flight separation technique [56]. In this work the latter has been used.

The experiment was performed by means of the LISE separator [57]. The LISE line in GANIL, allows the production of radioactive beams by fragmentation of the primary beam on the production target. A scheme of the LISE separator can be found in Figure 3.3. This spectrometer is achromatic between the object focal point (the production target) and the exit focal points (entry of rooms D4 or D6) where the experimental system can be placed. In other words, the position and angle of the particle at the focal point are independent of the energy of the particle. This allows the same time of flight regardless of the trajectory of the particle within the spectrometer.

The selection of the nucleus of interest among all the fragmentation products is carried out thanks to magnetic dipoles, a degrader and a Wien filter. The magnetic dipoles allow a selection in magnetic rigidity $B\rho$. However, this selection is not sufficient to select only the

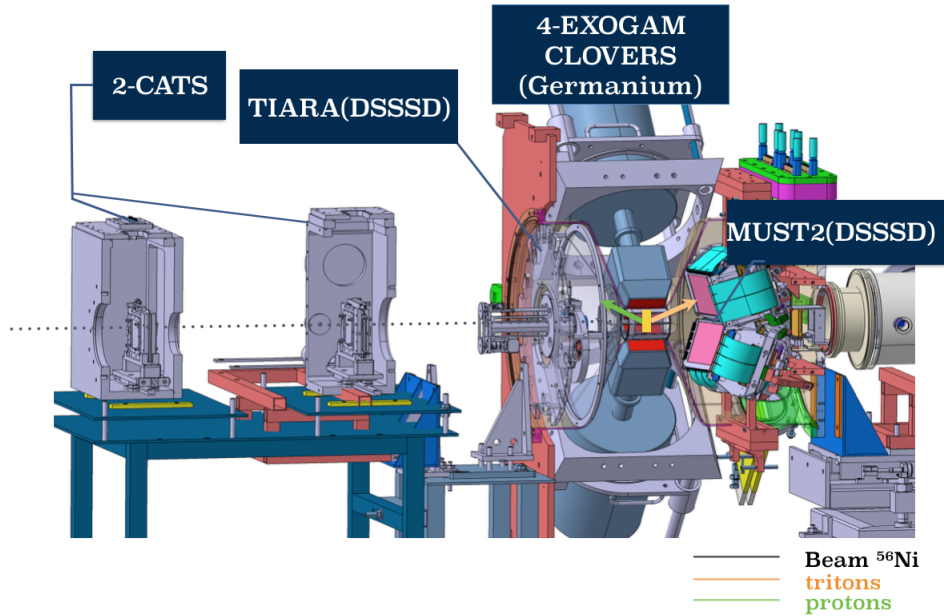


Figure 3.2: The experimental Set-up consisting of: CATS, TIARA, 4 EXOGAM Clovers around the target, MUST2 in forward angles and CHARISSA. The order of the detectors is with respect to the arrival of the beam from the left to the right. Illustration by E.Rindel.

nucleus of interest because several fragmentation products will have the same magnetic rigidity in the acceptance range the $B\rho$ of the spectrometer. This acceptance in magnetic rigidity can be adjusted thanks to a set of slits placed on the beam line (upstream of the degrader). A second selection is made by combining a second dipole with an achromatic degrader. The degrader is a thick material (Beryllium at LISE) that has a profile that allows the preservation of the achromatism of the spectrometer. The addition of a degrader on the beam line allows to slow down the fragments. The energy loss within the degrader is proportional to $\frac{AZ^2}{E}$, where A, Z and E stand for the mass, the nuclear charge and the energy of the nucleus of interest. The magnetic field of the second dipole is adjusted to select again the nucleus of interest. The combination of the degrader and the dipole allows a selection proportional in $\frac{A^3}{Z^2}$ which is made by using the exit slits. A third selection is made using the Wien filter. The Wien filter allows a selection in velocity thanks to the superposition of an electric field and an orthogonal magnetic field. Nuclei that have such a velocity that the magnetic and electric forces compensate each other are selected.

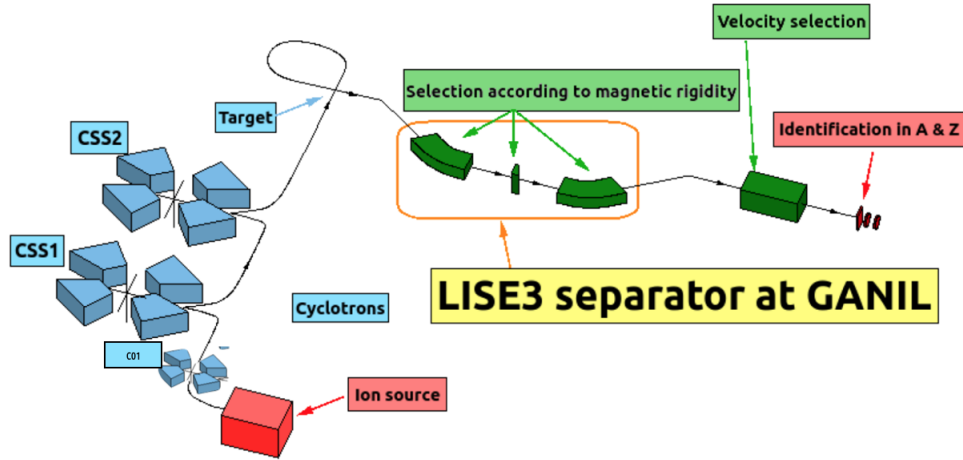


Figure 3.3: LISE Separator in GANIL

3.2.2 Secondary beam of ^{56}Ni

A primary beam of ^{58}Ni was produced by ionizing nickel atoms with an Electron Cyclotron Resonance Ion Source (ECRIS). The ions were accelerated, first by the C01 cyclotron and afterwards by CSS1 and CSS2, two separated sector cyclotrons, up to the energy of 74.5 A MeV and finally directed towards the CLIM rotating ^9Be target of 136.4 mg/cm^2 (1mm) thickness for fragmentation. The secondary beam of ^{56}Ni had an energy of 30 A MeV and a mean intensity of 10^5 pps.

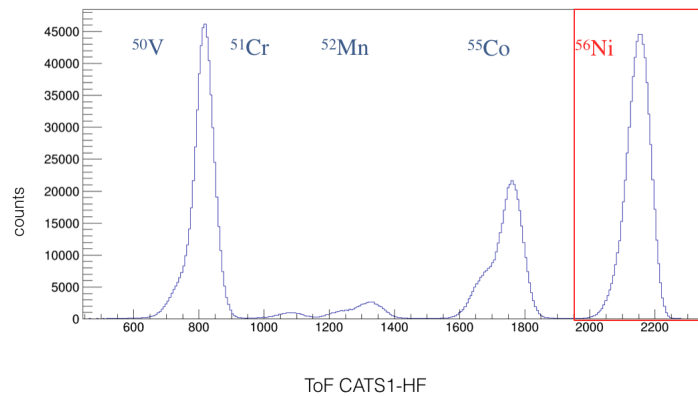


Figure 3.4: The separation of the different contaminants of the beam after the ToF selection

Due to multiple Coulomb scattering and straggling due to energy loss in the production target and the degrader, the fragmentation beams show a large energy and angular spread. This can

be diminished by using the slits at the dispersive plane of LISE at the expense of a reduction of the intensity of the beam. In our case the beam trajectory was measured event by event using the CATS detectors.

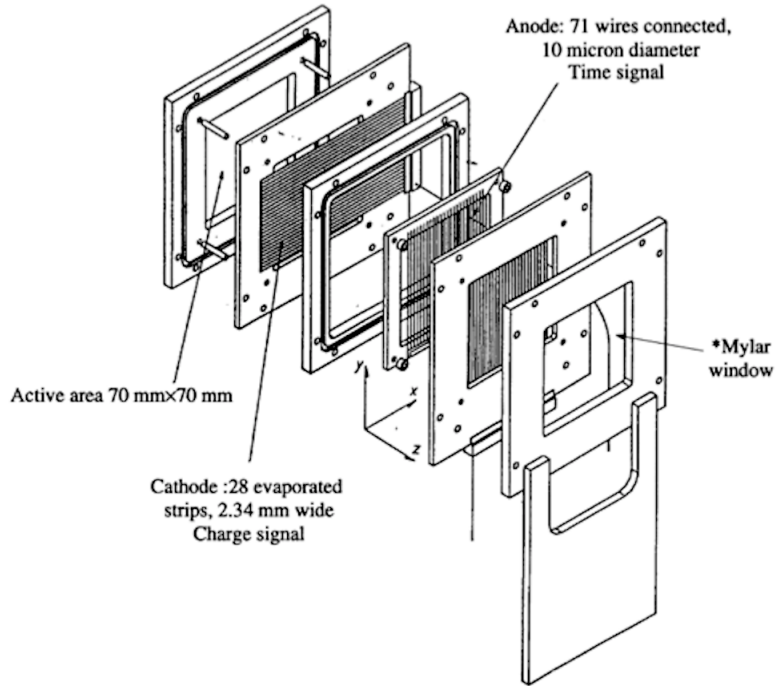


Figure 3.5: Schematics of a CATS detector

3.3 Beam Tracking Detectors: CATS

The accurate determination of the light particle emission angle is necessary in order to reconstruct the kinematics and therefore we place two CATS (Chamber A Trajectories of Saclay) detectors, at 1193 mm and 684 mm, upstream of the target. Thus, by performing path reconstruction we get information about the beam position on the target as well as the incident angle, with a good timing resolution of about 300 ps used for Time of Flight (ToF) identification.

The CATS are multi wire proportional chambers. The active area of the detectors is 70x70 mm². There are two Mylar foils 1.5 μm thick that contain the gas inside. At the center of the detector there is the anode which is made of 71 golden tungsten wires with a diameter of 10 μm and a distance of 1 mm from each other. On each side of the anode there are cathode planes at a distance of 3.2 mm. The cathode planes are segmented, containing 28 gold strips of 2.34 mm diameter and separated with 0.2 mm inter-strip. The schematic representation of a CATS detector can be seen in Figure 3.5 [58].

A high voltage between 600 and 800 V is applied on the anode to obtain a good resolution in time as well as a good collection by the cathodes of the charge carriers that are produced during the ionization of the gas while the ions pass through it. That allows us to obtain the position of the beam on the target with accuracy better than one millimeter. These detectors can withstand a count rate of up to about 10^5 particles per second with a beam that is spread over only a few wires.

3.4 Charged particle detection

3.4.1 Silicon Strip Detectors

For the charged particle detection the state of art is the silicon stripped detector (SSD). The SSDs cover a larger solid angle thus the statistics are high due to a large active area. Furthermore, the active area is segmented giving the possibility to measure the position of the particles. There are two kind of SSDs depending on the "approach" for providing the position of the hit along the strip: the double sided silicon strip detectors (DSSSD) and the position sensitive silicon strip detectors (PSSSD).

In the DSSSDs there are strips on the front and the back sides of the detector, in such a way (usually perpendicular to each other) that the hit position is determined by which strip was fired on the front and the back. Instead, in the PSSSDs strips are placed in one side and are made of a resistive material, which divides the charge collection giving rise to two signals that are taken at both ends of the strip.

3.4.2 TIARA

TIARA (Transfer and Inelastic All-angle Reaction Array) is a compact quasi 4π -position sensitive silicon array [59]. It is designed for direct reaction studies in inverse kinematics. In this experimental set-up it has been used for an angular range of 36° to 169.4° . Tiara consists in two separate detectors: the Hyball and the Barrel, both being used to give information about the

position and the deposited energy of the charged particles.

Hyball

The Hyball is made of 6 wedge shaped silicon strip detectors combined to create a circular shape with a hole in the middle (like a CD) so that the beam passes through see Figure 3.6. Each of the wedges is a $400\mu\text{m}$ thick double sided silicon strip detector (DSSSD) based on the 6-inch wafer technology and covers angles from 137° to 169.4° . Each wedge is divided into 16 ring-strips facing the target and 8 azimuth back sectors. The measured energy resolution for 5.5 MeV α -particles is typically 40 keV for the rings and 70 keV (FWHM) for the sectors.

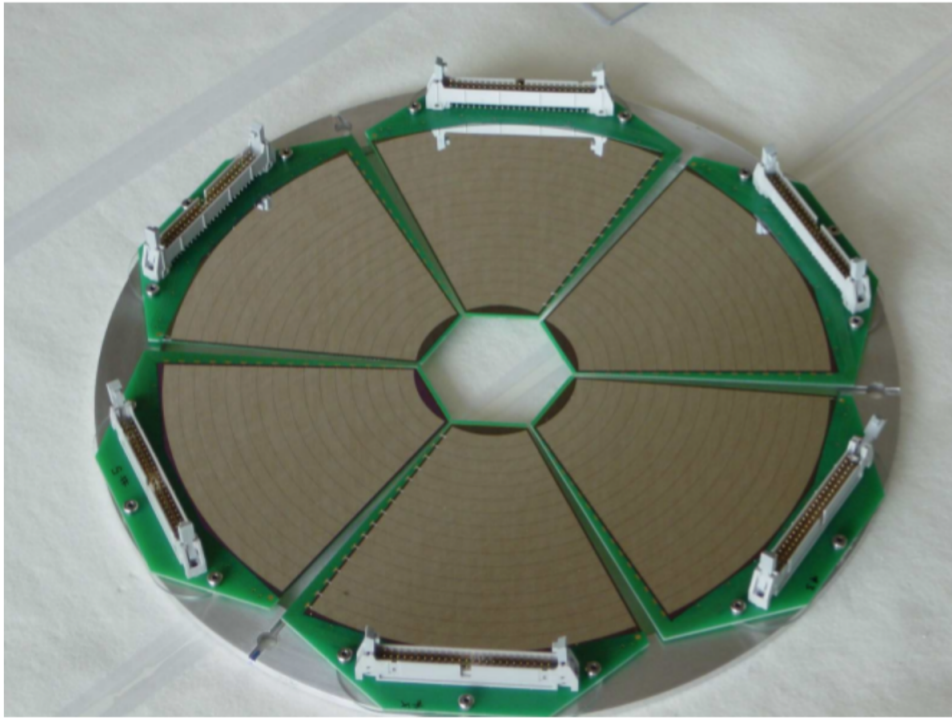


Figure 3.6: The Hyball part of the TIARA detector

Barrel

The Barrel consists of 8 resistive charge division detectors based on 6-inch wafer technology as well. They are assembled together so as to form an octagonal barrel around the target covering an angular range of 36° to 144° (Figure 3.7). The active area of the detectors is 94.5 mm long and

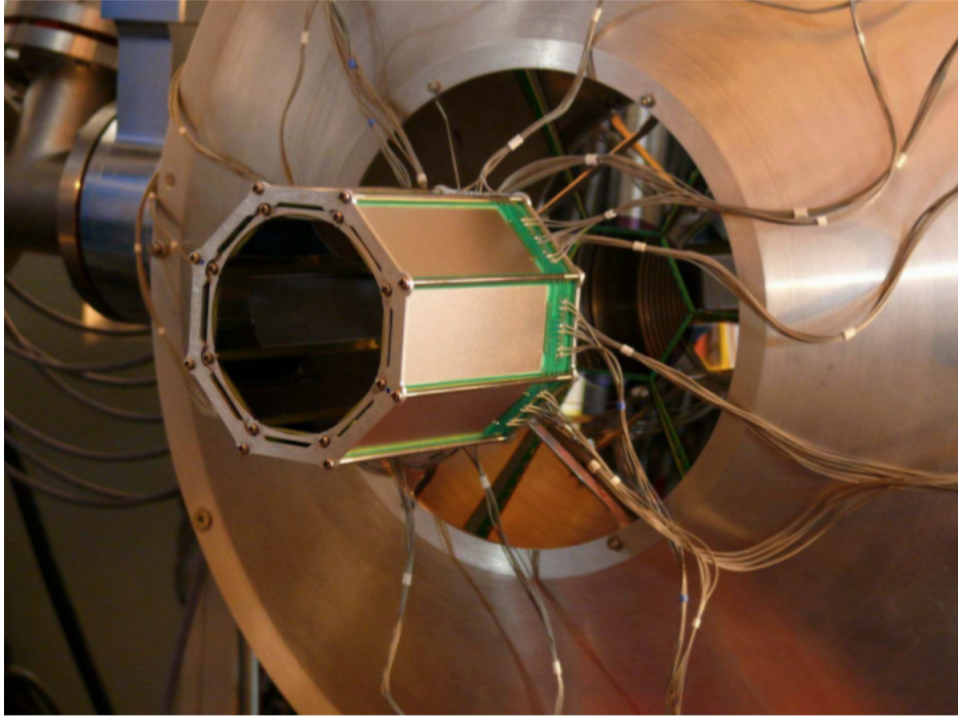


Figure 3.7: The Barrel part of the TIARA detector

22.5 mm wide with a thickness of $400\mu\text{m}$, which is segmented in four position-sensitive resistive strips along the beam direction. The strip pitch is 5.65 mm and inter-strip gap is $100\mu\text{m}$.

A second layer of $700\mu\text{m}$ thick silicon detector is placed outside of the octagonal barrel, forming an outer barrel. The Outer Barrel is segmented in the same way as the Inner one, with the difference that the Outer Barrel detectors are not position-sensitive since the information coming from the Inner one is sufficient.

The measured position resolution along the beam axis for 5.5 MeV α -particles is better than 1 mm and the energy resolution is 140 keV(FWHM).

3.4.3 MUST2

The MUST2 array [60] is the detector used to detect the light charged particles at forward angles. During our experiment 4 telescopes out of the 8 existing ones were used. They were placed 15 cm downstream of the target, covering an angular range from 10° to 40° . Each telescope consists of two different layers, the DSSSD and the Cesium Iodide (CsI) crystals. The particle identification can be done either by ΔE vs E for particles that reach the CsI or by E vs ToF, for particles that

stop in the first layer.

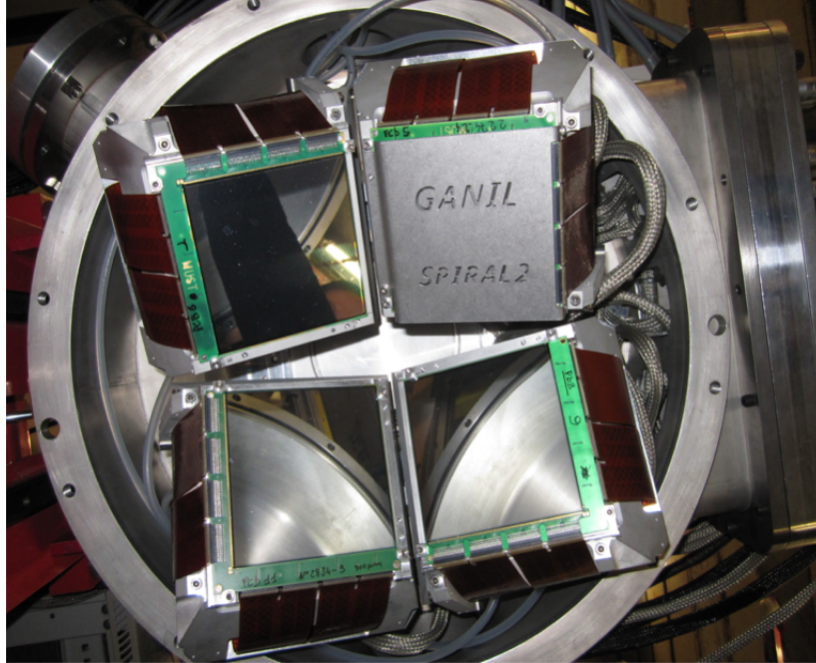


Figure 3.8: The MUST2 detector mounted in forward direction during the experiment- A mask is set on telescope number 3.

1st Layer

The DSSSD in the first layer is made of $300 \mu\text{m}$ thickness silicon and the active area of this detector is $98 \times 98 \text{ mm}^2$. On both sides of the silicon there is an evaporated layer of aluminum $0.7 \mu\text{m}$ thick. Each silicon is divided into 128 strips vertically and 128 horizontally. The strip pitch is 0.75 mm , thus the geometrical angular resolution is 0.15 degree at a distance of 15 cm . The typical energy resolution for one strip is 30 keV (FWHM) for $5 \text{ MeV } \alpha$ -particles, which translates into an overall resolution of 40 keV (FWHM) summing all strips. This layer provides us the information about the energy loss, the time as well as the position of the particle.

2nd Layer

The second layer consists of 4×4 CsI crystals with a thickness of 4 cm and an area of $30 \times 30 \text{ mm}^2$. The trapezoidal shape of the crystals limits the crossing of the particles from one crystal to another. The light produced by this scintillator during the passage of a particle is collected by

a photo diode at the back of each crystal. Each crystal is covered by a 3 μm aluminized Mylar sheet reflecting the light and thus isolating them optically from the others.

Electronics

The MUST2 detector electronics are based on ASIC (Application Specific Integrated Circuits) chips which are called MATE (MUST2 ASIC Time and Energy). At the back of each telescope there is a cooling system designed for the MUFEE (MUST Front End Electronics). The MATE, MUFEE and MUVI represent the full electronics of MUST2.

- (i) Each MATE treats 16 analog signals, it pre-amplifies the signals and divides them into two paths: time and energy. The “time” path is composed of a fast shaper, a leading edge discriminator and a time to amplitude converter (TAC). The “energy” path includes a slow shaper and a “track and hold” to get the maximum value. The outputs include analog levels for the time and energy and a logical trigger output.
- (ii) To treat the full information of the MUST2 telescopes one needs to use two MUFEE cards. The MUFEE card consists of nine MATE, the eight first ones correspond to the strip signals of the X and Y side respectively in the 2 MUFEE, while the last one can treat either the signals coming from the second layer of MUST2, the CsI crystals or another layer that has not been used here, the SiLi ¹. In total that gives 576 parameters that needs to be treated afterwards. With the use of these two cards the multiplexing and the data transmission to the ADC (Analog to Digital Converter) is being achieved. In addition these cards play also the role of the power supply (bias) distributor for the telescopes and the low voltage for the MATE. Finally, there is inside a pulse generator to test and calibrate the electronics.
- (iii) The MUVI card is placed in a VXI crate outside the chamber of the detectors and is responsible for the reading of the MUFEE card, the encoding of the data and the transmission of the data to the acquisition in case of a triggered event. Furthermore it passes the stop signal, usually coming from CATS, to the TAC of the MATE. Typically this card can be also used for additional filtering such as the pedestal subtraction.

In this experiment MUST2 was the main detector for the measurement of the one neutron transfer reaction: $^{56}\text{Ni}(p, d)^{55}\text{Ni}$ and $^{56}\text{Ni}(d, t)^{55}\text{Ni}$, as well as the $^{56}\text{Ni}(d, \alpha)^{54}\text{Co}$ two nucleon transfer reaction.

¹SiLi: Layer of MUST2 telescope of 4.5 mm Lithium drifted silicon, segmented in 8 pixels.

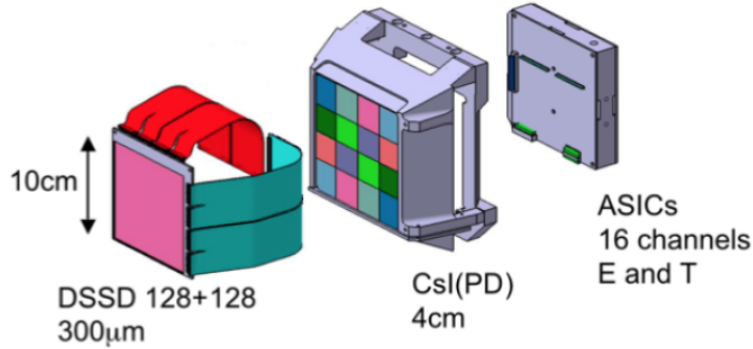


Figure 3.9: The scheme of the layers of MUST2: 1st layer DSSD , 2nd layer CsI and last the integrated MUFEE boards.

3.5 Recoil detection

3.5.1 CHARISSA telescope

One element of the CHARGed particle Instrumentations for Solid State Array (CHARISSA) was placed at zero degrees angle. It was planned to be used for the identification of the heavy residue of the beam after the reactions. Generally, it is used for particle identification reasons by energy loss methods. CHARISSA consists in three different parts. The first part of the detector is a 65 μm thick DSSSD, with an active area of 50x50 mm² and 16 strips on each side [61]. The experimental resolution achieved is around 150 keV(FWHM) in energy for α-particles of 5.5 MeV. The second part is a 500 μm thick DSSSD, with the same size and segmentation in the same way as the previous one. For α-particles of 5.5 MeV, the measured energy resolution is 110 keV(FWHM). The third and last layer is a 25 mm thick CsI crystal scintillator with an active area of 49x49 mm² which is used to stop the incoming particles and measure the residual energy. For α-particles of 5.5 MeV, the energy resolution obtained is 230 keV (FWHM). During the ⁵⁶Ni beam time the CHARISSA telescope was not used as planned.

3.6 γ-ray detection

The information of the γ-spectroscopy of the residual nucleus can significantly improve the information that we get for the structure of this nucleus, although the efficiency is low compared to the particle detection. We use it in order to identify the populated state of the residue and

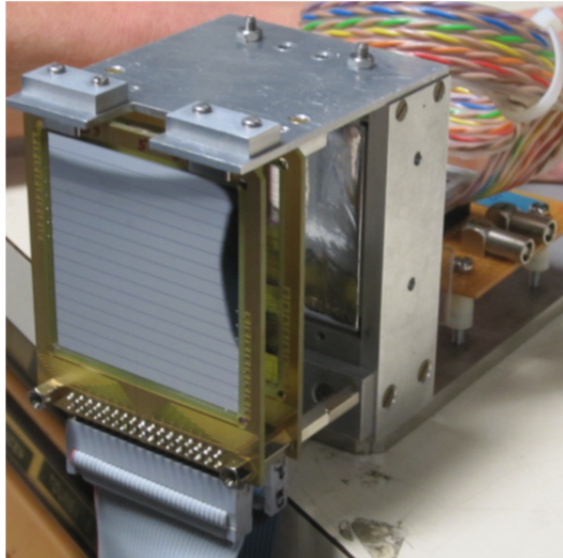


Figure 3.10: The CHARISSA detector

disentangle the excited states with respect to a simple particle measurement. The limited energy resolution from the particles measurement, can be alleviated using the measured γ -ray energies. The way that the γ detection is used in our experiment gives us information about the absolute ratio in between the populated states.

3.6.1 EXOGAM

EXOGAM (EXOtic GAMma) is a germanium detector for the detection of γ photons in spectroscopy experiment at GANIL [62]. This detector has a very good energy resolution, of the order of 3 keV (FWHM) at 1 MeV with a source of ^{152}Eu . It consists in its total configuration of 16 "clover" modules (Figure 3.11) thus covering almost 4π . However, in our experiment, only 4 clovers were used, arranged in a ring shape at 90° . Each clover consists of four germanium crystals (measuring 90 mm long and 60 mm in diameter) cooled by the same cryostat. Each crystal has a central contact measuring the deposited energy and this crystal is itself electronically divided into four segments (Figure 3.11) measuring the energy deposited in the segment.

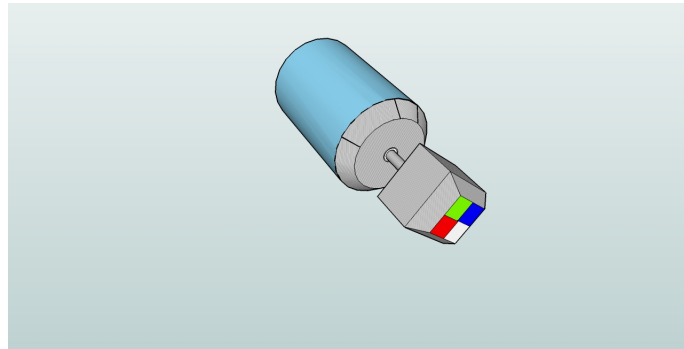
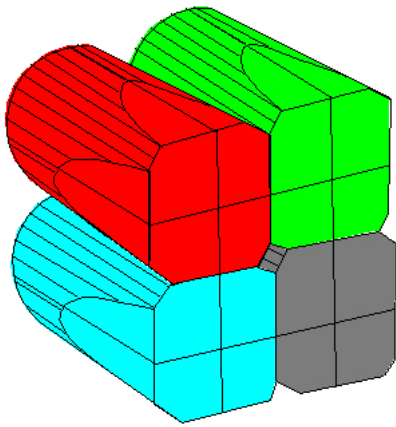


Figure 3.11: Schematic representation of an EXOGAM Clover and Segments

The clovers are positioned in such a way (see Figure 3.11) that the front face of the crystals is about 5 cm from the target. This proximity to the source and the size of the crystals maximizes the efficiency of detection. Since in our experiment γ rays from the nucleus of interest are emitted in flight, it is necessary to correct the Doppler shift. After correction, the energy resolution is approximately 80 keV.

4

Data Analysis

Contents

4.1	Data Analysis Overview	54
4.2	Beam Particle Selection	55
4.3	CATS	55
4.3.1	Calibration	56
4.3.2	Beam path reconstruction	56
4.3.3	Beam reconstruction at target position	57
4.3.4	Reconstruction validation	59
4.4	Targets	60
4.5	Time and Energy Calibration	61
4.5.1	MUST2: Energy and Time Calibration	61
4.5.2	DSSSD Time Calibration	63
4.6	Particle Identification	64
4.6.1	Hit on target condition	64

4.6.2	Light Particle Identification for forward angles	67
4.6.3	TIARA-Hyball Energy Calibration	68
4.6.4	EXOGAM Energy calibration	70
4.7	Energy Losses	73
4.8	Simulation for the reactions of interest	73
4.8.1	Kinematic lines and resolution	74

4.1 Data Analysis Overview

To be able to extract all the experimental results from the reactions of interest, such as the kinematic lines and the excitation energy of the reaction residues we need to follow procedures described below:

- (i) Selection of the beam by using time of flight.
- (ii) Reconstruction of the beam impact on target by using the CATS detectors and reconstructing techniques.
- (iii) Energy and Time calibration of the MUST2 detector for information on the light particles in forward angles.
- (iv) Particle Identification techniques by using Time of Flight vs Energy matrices and the Wien filter information.
- (v) Energy calibration of the TIARA detector-Hyball for information on the light particles in backward angles.
- (vi) Energy calibration, efficiency corrections as well as Doppler correction for the 4 EXOGAM clovers.
- (vii) Energy loss corrections for obtaining the incident energy of the reactions.
- (viii) Post-experiment simulations provide valuable information for the next analysis steps.

4.2 Beam Particle Selection

The secondary beam of ^{56}Ni was produced by fragmentation of ^{58}Ni in a secondary beam of ^{56}Ni with an average intensity of 10^5 particles per second. In the secondary beam, there were present more than one N=26 isotones that can be seen in Figure 4.1 from left to right we find: ^{50}V , ^{51}Cr , ^{52}Mn , ^{55}Co and ^{56}Ni . This HF-CATS time of flight graph, measured between the cyclotron radio-frequency and the first CATS detector, is a very useful parameter since it is the main measurement governed by the flight path before the reaction target, and therefore provides an excellent tool to select the beam particles. We applied the following condition $\text{TAC-CATS1} > 1900$ in order to select only the secondary beam of interest.

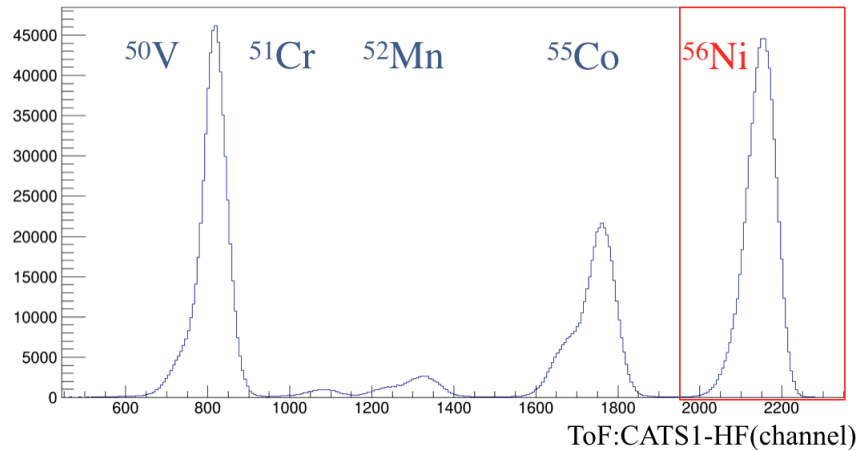


Figure 4.1: Time of Flight in between the HF and the CATS1 shown all the isotones that were present in the beam. In the red box we see the particles of the beam that we are interested in, ^{56}Ni .

4.3 CATS

The information we have about the beam position is extracted by the analysis of the CATS detectors as mentioned in 3.3. In this section, we will discuss the alignment method applied for the analysis. To get the hit position, the relative gain between strips is needed. Thus, a relative calibration with the use of a pulser was performed.

4.3.1 Calibration

A pulse generator has been used, sending the pulse to the anode of the detector. It creates an induced charge on the two cathodic strip planes of the detector. By varying the amplitude of the signal delivered by the generator we obtain different peaks of which we can determine the position and the resolution (σ) of the signal thanks to a Gaussian fit.

It is possible that when a strip is fired all other strips are also recorded, with most of the time the information being noise. The sum of this kind of events appears as a peak around zero, that is called *pedestal*. The pedestal is fitted with a Gaussian in order to get the channel number and subtract it from the data to set the zero. The position of the pedestal is noted as P_i and its sigma σ_i for each strip i . After subtraction of the pedestal, a second-order fit is performed, according to the following equation for each strip i for the calibration of the charge Q_{cal} :

$$Q_i^{cal} = \alpha_i(Q_i^{raw} - P_i)^2 + \beta_i(Q_i^{raw} - P_i) + \gamma_i \quad (4.1)$$

Where α , β and γ are the fit parameters of the calibration for each strip i . We define a threshold (Th) for each strip of the detector by using the mean and sigma of the pedestal peak and that can be described as follows:

$$Th = P_i + n\sigma_i \quad (4.2)$$

where $n=5$. Only signals with a value above this threshold are considered in the analysis.

4.3.2 Beam path reconstruction

The algorithms that determine the charge centroid can be classified in two categories: those that perform calculations of the center of gravity of the charge distribution and the other that assumes that the charge distribution can be described with an analytical function (Gaussian, Lorentzian or squared hyperbolic secants.) In this work, the algorithm used for the analysis was the squared hyperbolic secants method. The analytical function that describes the position of the charge of one strip by the squared hyperbolic secants algorithm is the following [58, 63]:

$$P = \frac{A}{\pi} \tanh^{-1} \left(\frac{\sqrt{\frac{Q_m}{Q_{m+1}}} - \sqrt{\frac{Q_m}{Q_{m-1}}}}{2 \sinh\left(\frac{d\pi}{A}\right)} \right) \quad (4.3)$$

where,

$$A = \frac{d\pi}{\cosh^{-1}\left(\frac{1}{2}\left(\sqrt{\frac{Q_m}{Q_{m+1}}} + \sqrt{\frac{Q_m}{Q_{m-1}}}\right)\right)} \quad (4.4)$$

In the above formula we consider $d = 2.54 \text{ mm}$ the distance between two strips, m is the strip with the larger charge (or the strip of interest), $m - 1$ and $m + 1$ the neighboring strips. The calibrated charge of each of those strips is noted with Q and so we have Q_m , Q_{m-1} and Q_{m+1} respectively.

The position extracted by the use of the analytical technique, will be fitted afterwards by the use of the Gaussian method to determine the centroid of the position with better precision.

4.3.3 Beam reconstruction at target position

By taking into account the position of the two CATS detectors in the beam axis (CATS1 at -1193 mm and CATS2 at -684 mm), and if the target is perpendicular to the beam as shown in Figure 4.2, then the $(X_{\text{target}}, Y_{\text{target}})$ position is:

$$X_{\text{target}} = X_1 + \frac{(X_2 - X_1)}{t} \quad Y_{\text{target}} = Y_1 + \frac{(Y_2 - Y_1)}{t} \quad (4.5)$$

where $t = \frac{l+L}{l}$ and L is the distance between CATS2 and the target and l the distance between the two CATS.

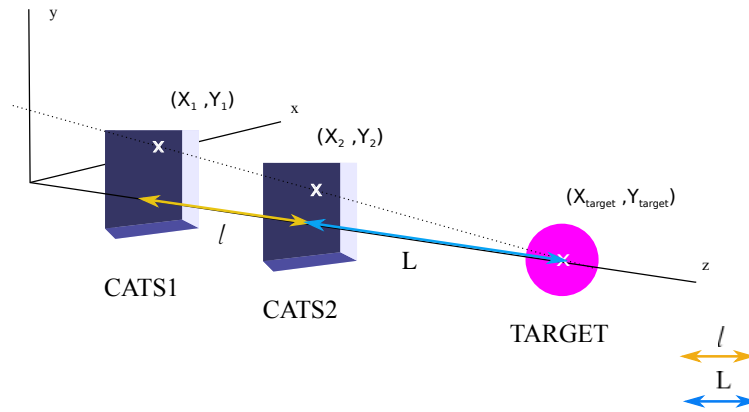
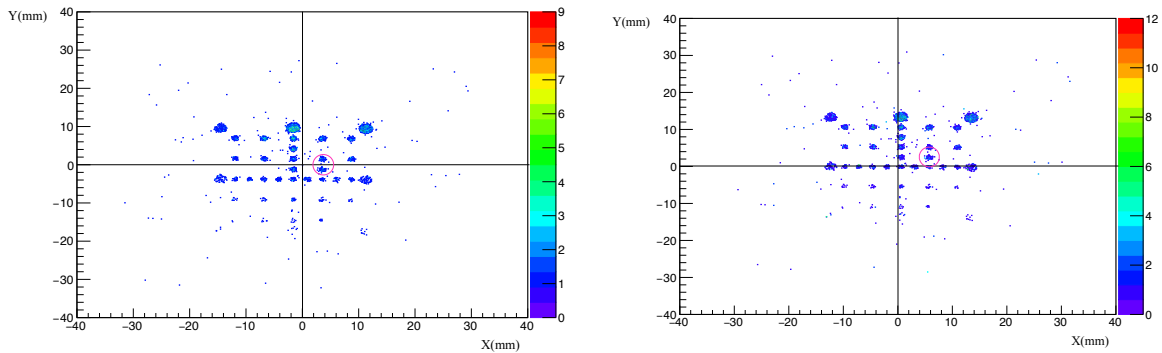


Figure 4.2: Schematic representation of the beam reconstruction on target position

Mask on CATS

During this experiment, and only for a few runs, a mask was placed in front of the first CATS detector. Ideally we would like to have placed masks on both CATS and most importantly on the target position. The position of the mask has been given by the surveyor with respect to the beam axis. Thus, the central wire of each CATS should be aligned on the center of the mask to be at $(0,0)$ on (X,Y) . The asymmetric pattern of the mask reveals a point on the positive X and Y axis side that doesn't exist on the negative side noted with a pink circle in Figure 4.3a which shows the reconstruction of the mask on the first CATS detector. By reconstructing the image of the mask on the second CATS detector and following the orientation that the "mark" reveals, we can now calibrate the position of the two detectors with respect to the center of the mask Figure 4.3b. The first validation comes when we plot the mask reconstruction on the target and the center of the mask is located as well at the $(0,0)$ point as can be seen in Figure 4.4.



(a) The mask placed in front of CATS1, without any position calibration (b) The mask placed in front of CATS1, after position calibration.

Figure 4.3: Mask reconstruction on CATS1 with uncalibrated position (a) and after position calibration (b)

Corrections

The previous position was obtained assuming that the CATS detectors were centered on the beam axis. However, a correction has to be included in order to account for any possible misalignment of the detectors. Although a surveyor has measured the detector positions by laser alignment, the corrections have been determined empirically to achieve the most accurate reconstruction of the beam at the target position.

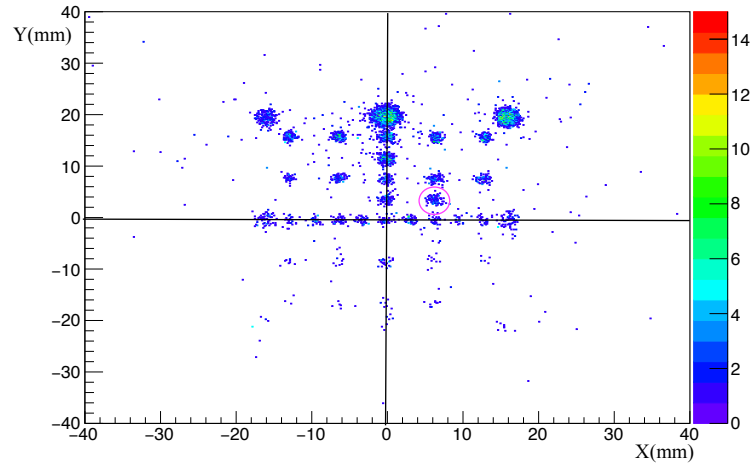


Figure 4.4: The mask placed in front of CATS1, reconstructed on target position

The final corrections for the X,Y of the CATS detectors that we took into account in this work are presented in the following Table 4.1.

	CATS1	CATS2
$X(mm)$	2.3	3.5
$Y(mm)$	-2.8	3.5

Table 4.1: Corrections used during the analysis for CATS1 and CATS2

4.3.4 Reconstruction validation

In order to cross check the reliability of the corrections that we took into account for the position of the two CATS detectors individually, it is necessary to obtain the position of the two CATS as a function of the rest of the set-up to obtain a reliable reconstruction. We can consider the beam profile as a Gaussian the tails of which hit the MUST2 corners which are closer to the target in addition to the target of interest. Thus, by performing a superposition between the impact matrix of the MUST2 telescopes (black shade in Figure 4.5) and the projection of the beam at the corners of the MUST2 (colored dots in Figure 4.5), it is clear that the MUST2 corners hit by the beam (color) overlap with the MUST2 corners from the impact matrix (black) thus we conclude that the reconstruction using the beam is reliable.

The white gaps on the MUST2 telescopes shown in the figure correspond to non-working strips of the DSSSD. In the following section, 4.6.3 information about the status of the strips of

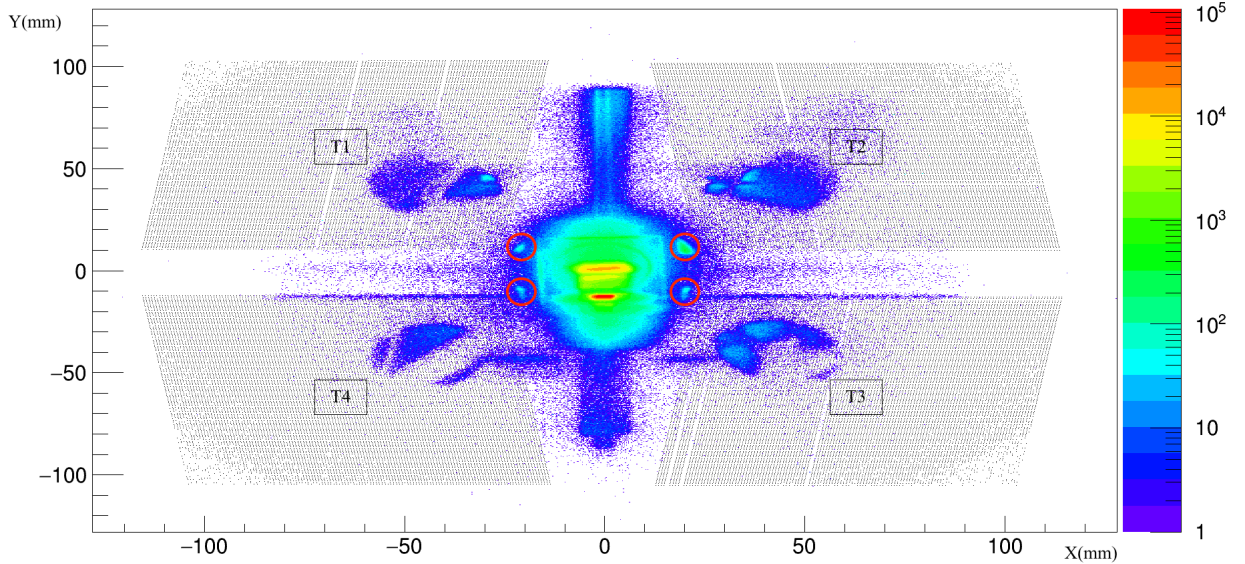


Figure 4.5: Overlay of the MUST2 telescope impact matrix (in black) with the projection of the beam on target at the corners of MUST2 (color). The number of each telescope is indicated upon the corresponding detector.

MUST2 and the TIARA-Hyball during this experiment will be presented.

4.4 Targets

For this experiment, three different kinds of targets were used. The main targets were CH_2 and CD_2 targets. In addition, there was a ^{12}C target for estimating the carbon background present in the reactions. For that purpose, the thickness of the ^{12}C was chosen to be roughly equivalent to the carbon (C) that the CH_2 and CD_2 targets contain. The thicknesses provided by the manufacturer as well as the corresponding transfer reactions can be seen in the following Table 4.2.

Target	Thickness (mg/cm^2)	Reaction Studied
CH_2	4.0, 6.8	(p,d), (p, ^3He)
CD_2	7.0	(d,t) (d, α), (d,p)
^{12}C	2.8	Background

Table 4.2: Targets used during the experiment

4.5 Time and Energy Calibration

4.5.1 MUST2: Energy and Time Calibration

DSSSDs Energy Calibration

The DSSSDs consist of 128 strips on each side of the detector, the X and the Y signals. These signals are read-out by two MUFEE cards and are of different polarities. For that reason, the X signals which are of positive polarity are coded from the channel number 8192 to 16384, while the Y signal of negative polarity is coded from 8192 to 0. The channel that corresponds to the zero energy is the channel 8192. Thus, the pedestal of the different channels is measured before the experiment and realigned between them in the *Data Acquisition System* (DAS) to be the channel 8192. The energy loss of the particle in the material (ΔE) depends on the mass A, the charge Z and conversely of the energy E of the particle according to the relation of Bethe-Bloch, here approximated:

$$\Delta E \sim \frac{AZ^2}{E} \quad (4.6)$$

A three- α source (^{239}Pu , ^{241}Am , ^{244}Cm) was used to calibrate all the strips at the beginning and at the end of the experiment. This source produces three main α lines at 5.157, 5.486 and 5.805 MeV, plus three satellite peaks. Each main peak and their satellites were fitted by a sum of Gaussian function for each strip of the DSSSD in order to find a relation between the channel and the energy.

$$E_{DSSSD} = \alpha + \beta E_{CH} \quad (4.7)$$

where E_{CH} is the energy from the corresponded channel and E_{DSSSD} the calibrated energies, and α and β are the calibration parameters. The typical resolution is 40 keV FWHM.

CsI Energy Calibration

The calibration of CsI crystals differs from that of the DSSSDs. The calibration of the CsI depends on the type of the detected particle. When a particle stops in the CsI crystal, it produces light that is collected by a photodiode. This production of light is specific to each particle thus it does not allow us to perform a unique calibration for all particles.

Since the DSSSDs are calibrated in energy, it is possible to construct an identification matrix of the ΔE_{DSSSD} (the energy loss in the DSSSD detector) as a function of E_{CsI} (energy deposited

in the channel CsI crystal) for each of the CsI crystals of each MUST2 telescope. By performing a graphical cut on the desired particle in the matrix of identification and adjusting the hyperbolic shape of it using an inverse function with A, B, C free parameters according to the following equation, we can get a relationship between the energy loss in the DSSSD and the energy in the corresponded channel in the CsI.

$$\Delta E_{DSSSD} = A + \frac{B}{E_{CsI} - C} \quad (4.8)$$

Using a suitable energy loss table (here ATIMA used in LISE ++), we can, for a certain type of particle, know the energy deposited in the crystal of CsI from the energy lost in the DSSSD. At high energy, the uncertainty about the energy calibration is very important because the more a particle gains higher energy, the less energy it will lose in the DSSSD. At these high energies occurs a phenomenon of light absorption by the crystals called quenching. This requires using a nonlinear calibration as shown in Figure 4.6 where the blue curve shows the calibration of a CsI crystal using an adjustment with a third order polynomial fit. By knowing the energy in the DSSSDs we can now plot particle identification matrices as shown in Figure 4.7.

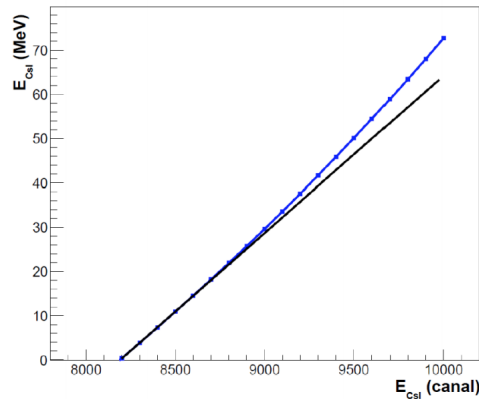


Figure 4.6: Graph representing the calibration function of a CsI crystal (blue) for the deuterons. The calibration function is non-linear at high energy (linear behavior in black).

In this work, the CsI calibration has been used for deuteron identification and the analysis of the (p,d) reaction.

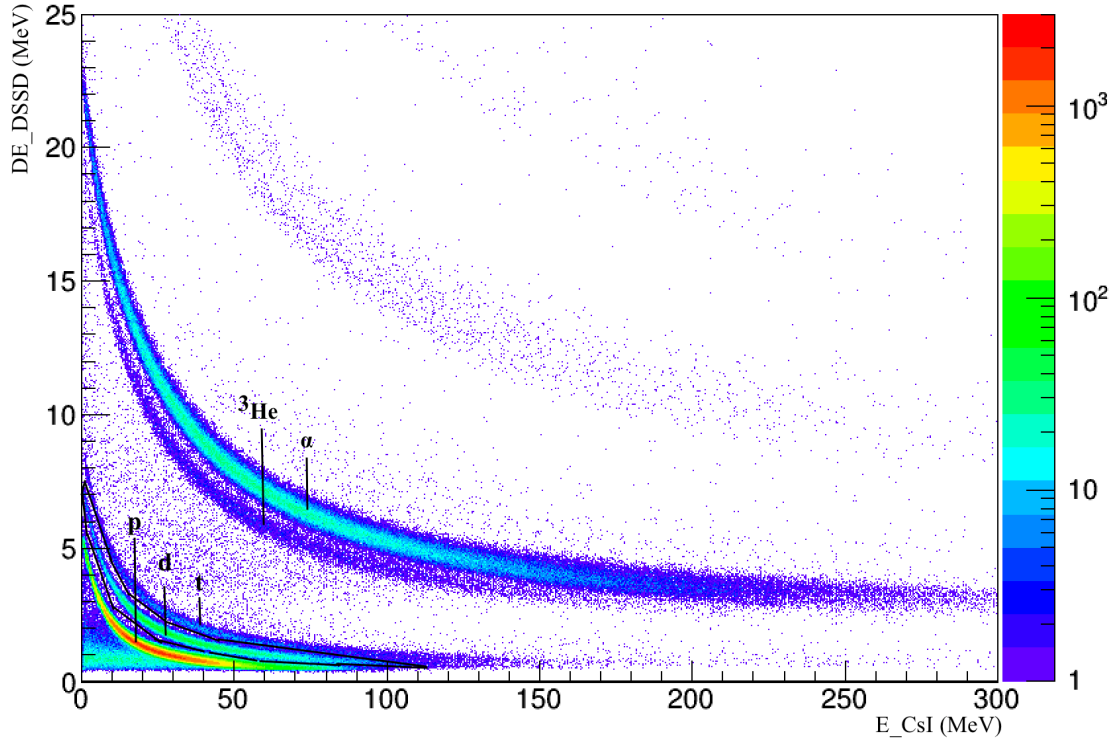


Figure 4.7: Particle identification matrix $\Delta E_{DSSSD} - E_{CsI}$.

4.5.2 DSSSD Time Calibration

For the time calibration purposes, a time calibrator module has been used generating a start and stop signal for each strip of the detector. The stop signal is delayed compared to the start signal by a different number of fixed periods in order to cover the whole spectra range. In this case, the time range was 640 ns divided into 10 ns periods. A second order calibration was applied. A typical spectrum can be seen in the Figure 4.9 .

After the use of the time calibration there are some strips of the same telescope that are misaligned like for example in Figure 4.8. By plotting the projection of the punch through for each strip we can get the exact position of the punch through and shift the time spectrum such as every strip has the same ToF-punch through point.

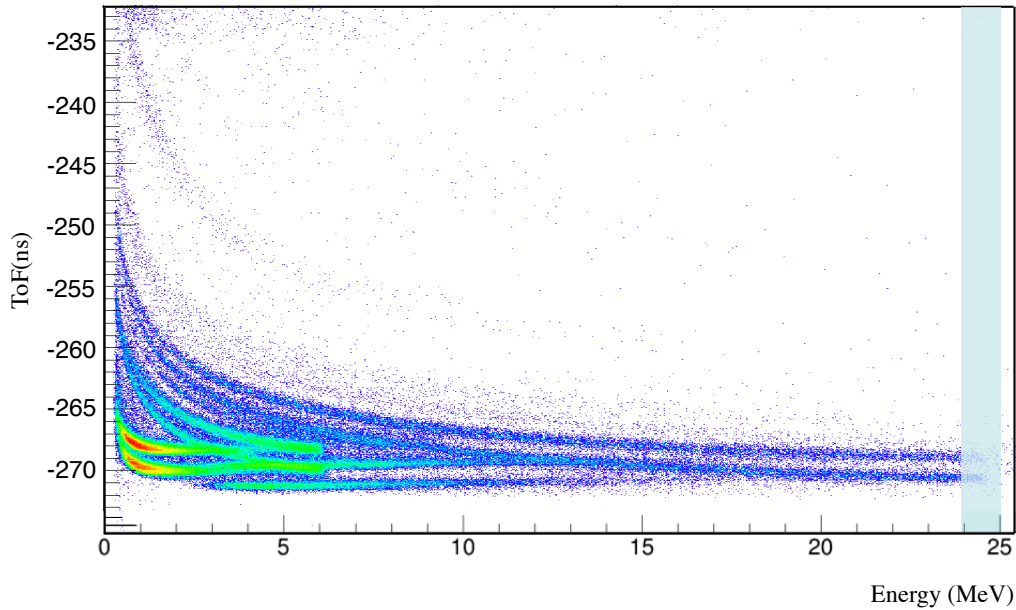


Figure 4.8: Time of flight particle identification for Telescope 3 of the MUST2 detector. Some of the strips appear to be misaligned. The light blue area indicates the punch through of the α particles at 25 MeV.

4.6 Particle Identification

In this section we will see how we select the beam particles on the target and the light ejectiles of the reactions that are of interest. In addition to the choice of particles in the forward direction, made using the MUST2 detector and the ToF process, the selection at the backward angles is made by using more than one detectors.

4.6.1 Hit on target condition

In addition to the position measurements and incident angle of incoming ions, the beam position reconstruction on the target plane discussed in section 4.6.1 serves the purpose of developing a condition for selecting the events that reached the target.

The Wien Filter from the Lise separator [65] was used during the experiment. Wien Filter, also known as velocity selector, is a device consisting of perpendicular electric and magnetic fields that can be used as a velocity filter for charged particles. In this case the Wien Filter separates vertically as can be seen in Figure 4.11 all the contaminants of the beam. The events closer to

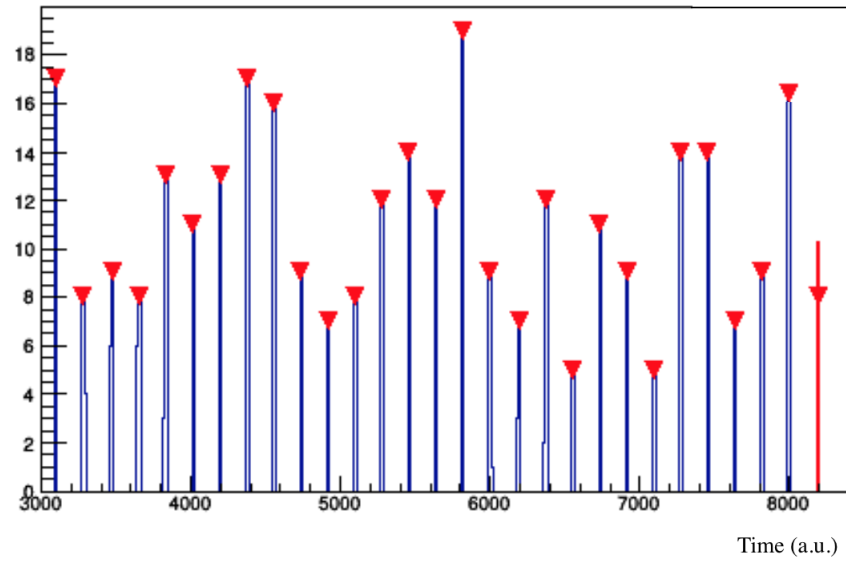


Figure 4.9: Time calibrator peak for telescope 2. The period between two peaks is 10 *ns*.

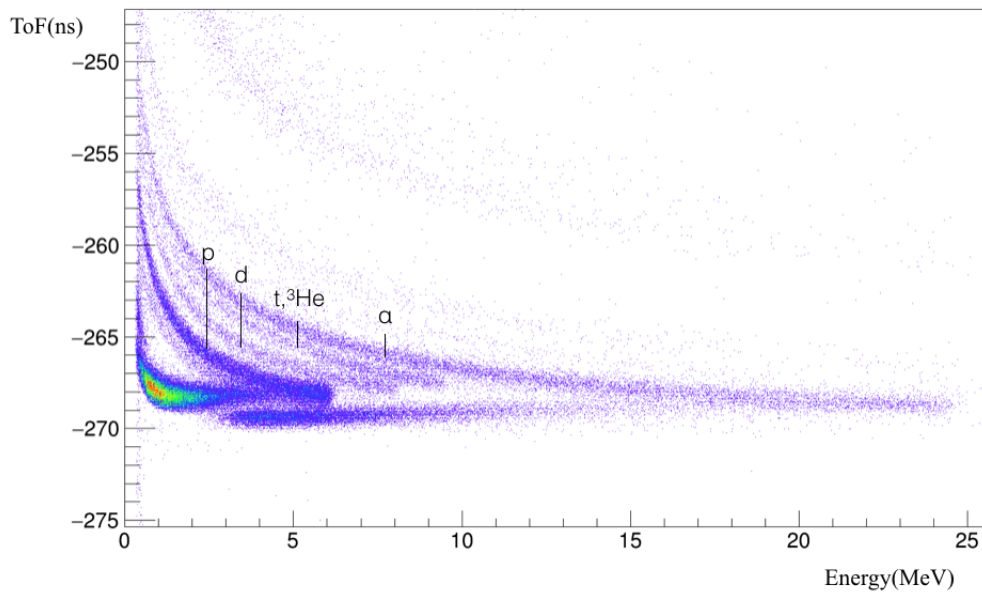


Figure 4.10: Light Particle identification of forward angles with the MUST2 Telescopes

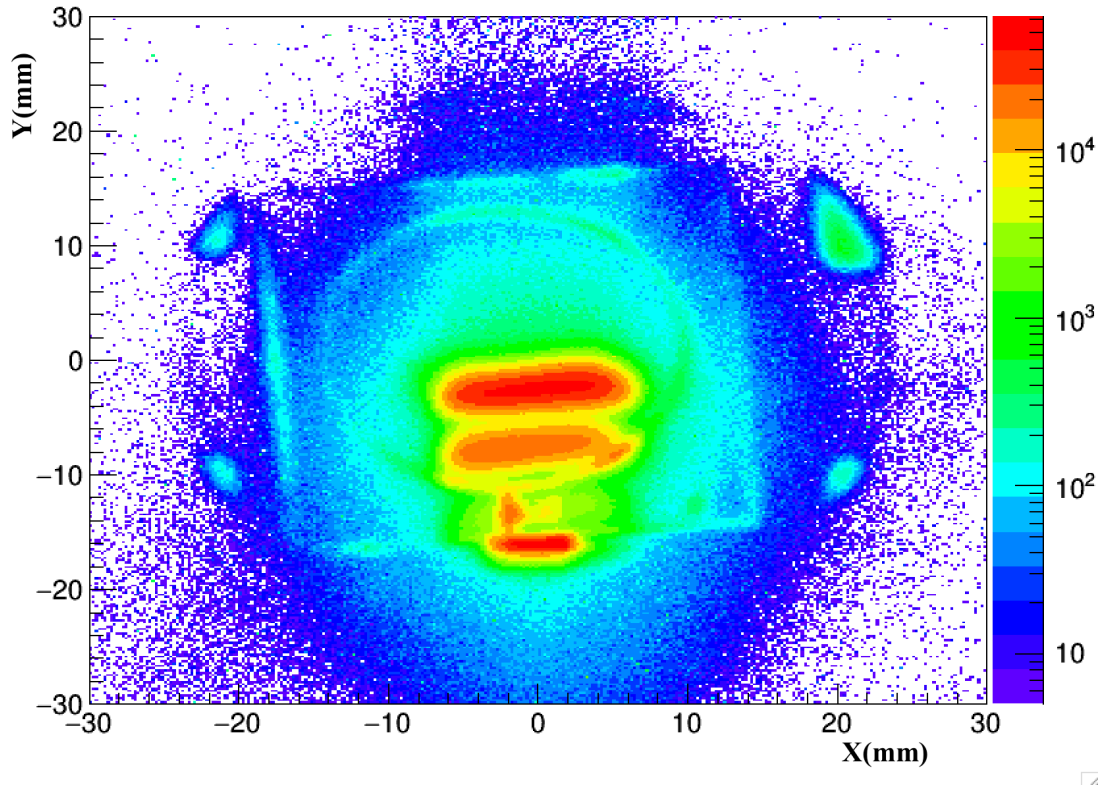


Figure 4.11: Reconstruction of the beam on the target position. Visible in this picture are the contaminants of the beam vertically separated.

the center of the target correspond to the ^{56}Ni beam. The time of flight selection mentioned before removes the contaminants. In addition, a gate on the X-Y position was applied as can be seen as a black circle in Figure 4.12 in order to remove any reaction on the target frame.

The Figure 4.12 corresponds to the runs with the CD_2 target. One can notice that on the left side the frame of the target appears tilted, further details on how this difficulty was further investigated can be found in Appendix A.

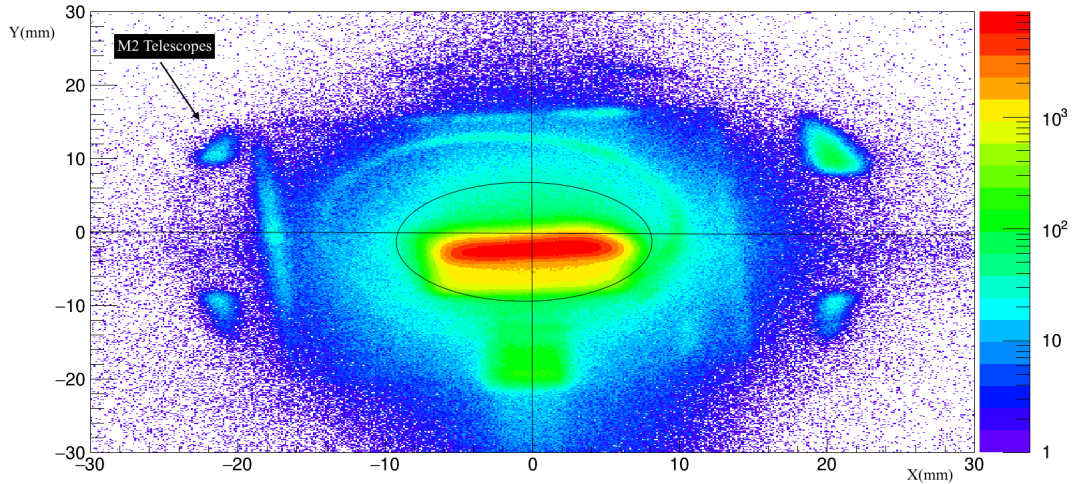


Figure 4.12: Reconstruction of the beam on the target position for ^{56}Ni selection. Visible in this picture are the corners of MUST2 as well as the unexpected phenomenon of tilted target that we faced.

4.6.2 Light Particle Identification for forward angles

MUST2-Time of flight selection

The relationship between the time of flight t , the energy E and the flight path distance L of particle of mass m is given by:

$$E = \frac{1}{2}mu^2 = \frac{1}{2}m \left(\frac{L}{\Delta t} \right)^2 \rightarrow \Delta t = \sqrt{\frac{mL^2}{2E}} \propto \sqrt{A} \quad (4.9)$$

The Time of Flight helps us to identify the light particles according to their A . In the ToF vs E spectrum of Figure 4.10 we can identify the light particles in forward direction that hit the MUST2 detector. While we use only the events of the first layer of the DSSSDs by selecting zero events in the CsI crystals, the residual punchthrough is still visible in this PID spectrum due to the fact that the CsI crystals have a smaller geometrical coverage. Thus some of the light particles go through the first layer of MUST2 without entering the second layer afterwards. For a same total energy E for instance, an ^3He and a ^3H have the same time of flight. However in our case, the ^3He has smaller energy than the ^3H in the reaction exit channel and the separation of the two is not required for the next analysis steps.

4.6.3 TIARA-Hyball Energy Calibration

In the backward angles, the particles of interest are the protons. For particle identification, we performed a ToF-E technique. The E calibrations have been performed using the same double-sided 3α -source placed at the target position as for the MUST2 detector. This source produces three main α lines at 5.157, 5.486 and 5.805 MeV as seen before, plus three satellite peaks that are hardly resolvable with TIARA.

The energy spectrum of each strip is fitted with a combination of three Gaussian functions to take into account the three main α peaks. A typical spectrum can be seen in Figure 4.13. Once the peak centroids have been determined, we assume a linear relationship between the ADC channel number and the energy deposited:

$$E = \alpha + \beta E_{CH}, \quad (4.10)$$

where E_{CH} is the corresponded channel and E the calibrated energies, and α and β are the calibration parameters.

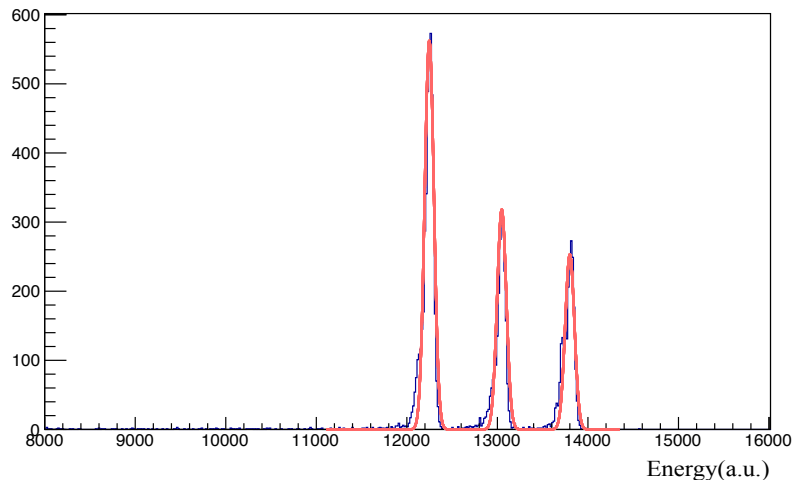


Figure 4.13: 3 alpha peaks for the Tiara calibration and the Gaussian fit

From the calibration already we can find out which strips of the silicon detector were well functioning during this experiment and which not. In Figure 4.14 one can see the impact matrix of the TIARA-Hyball detector, the six wedges are visible, though the figure does not allow us to distinguish in between sectors and rings easily. In addition, the identification and the statistics at the backward angles did not allow us to go further with the analysis of TIARA.

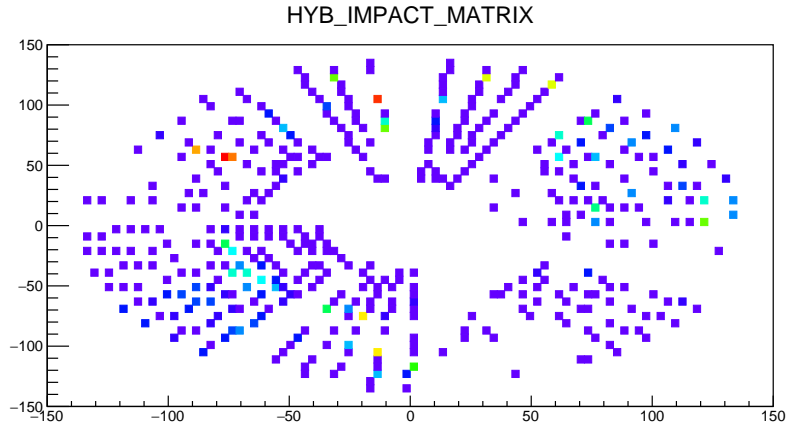


Figure 4.14: TIARA- Hyball impact matrix that shows all 6 wedges, rings and sectors.

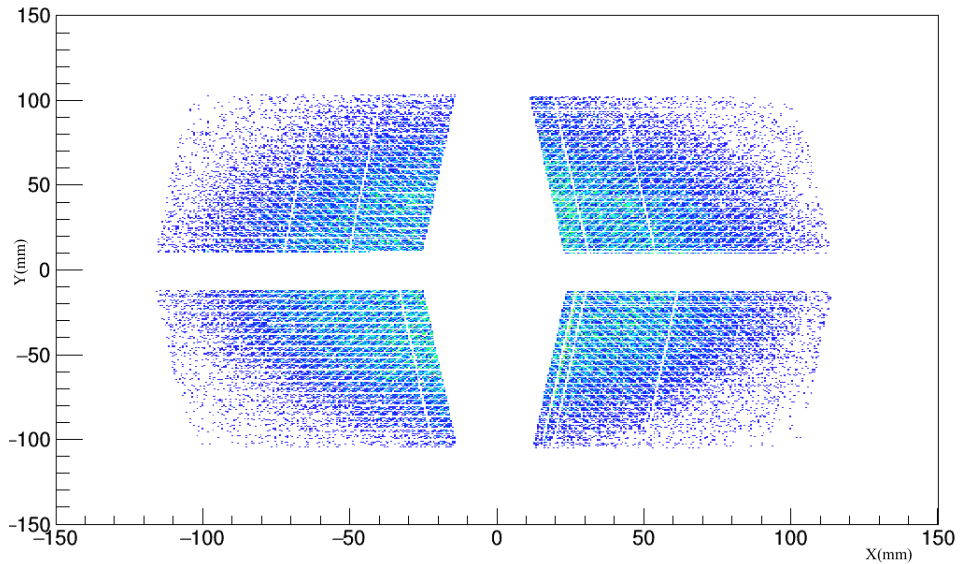


Figure 4.15: MUST2 detector impact matrix, for all four telescopes.

Working strips MUST2 and TIARA-Hyball

By looking at the two impact matrices of the two different silicon detectors Hyball and MUST2 we can now give a brief report on the condition of the detectors during the experiment. In general, one could conclude that both the detectors were in good condition with the worst case being the Ring side of the Hyball with 24% non-working strips.

The exact numbers of the working and non-working strips for the MUST2 telescopes can be

seen in Table 4.3 and Table 4.4.

	T1	T2	T3	T4
<i>X – side</i>	124/128	124/128	126/128	123/128
<i>Y – side</i>	123/128	126/128	122/128	128/128

Table 4.3: Number of working strips over the total number of strips on each side of all the telescopes of the MUST2 detector.

	W1	W2	W3	W4	W5	W6
<i>Ring – side</i>	11/16	11/16	12/16	12/16	11/16	9/16
<i>Sector – side</i>	7/8	8/8	8/8	8/8	5/8	8/8

Table 4.4: Number of working strips over the total number of strips on each side of all the wedges of the TIARA-Hyball detector.

4.6.4 EXOGAM Energy calibration

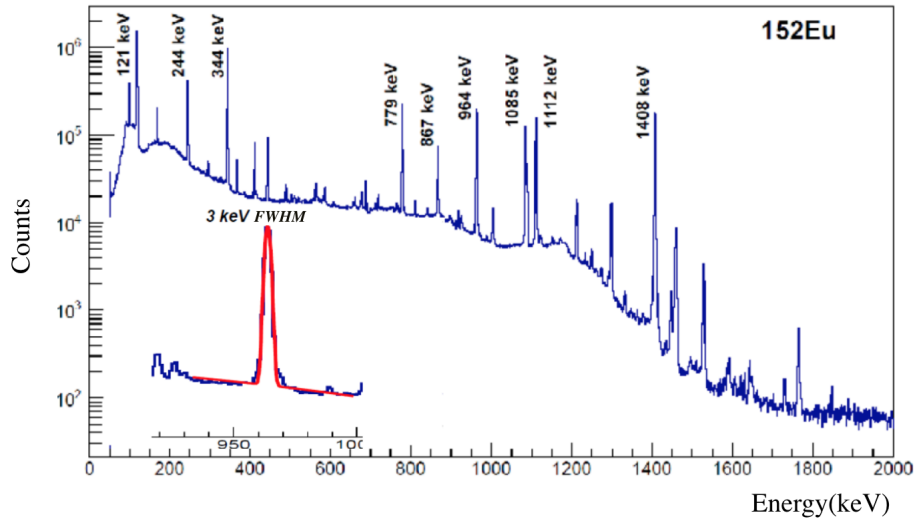
The γ spectrum analysis adds information about the population of the heavy residue excited states. Thus, it is necessary to proceed to the calibration of the γ -detector EXOGAM and take into account the add-back of all crystals.

For energy calibration purposes a ^{152}Eu source has been used, placed at the target position. The 9 γ peaks of the source are spread over a wide range enhancing in that way the reliability of the calibration. The positions of the peaks and the corresponding energies were plotted (Table 4.5 and Figure 4.16) and the calibration parameters were extracted by a second-order polynomial fit.

Add Back and Efficiency correction

Since the probability that a γ -ray will interact more than twice in the same clover is small, we only took into account events with a maximum multiplicity of two for the same clover. Taking into account events with a multiplicity 2 by finding the location of the interaction and reconstructing the initial energy of the γ ray makes it possible to obtain a better photopeak detection efficiency and better signal-to-noise ratio. The add-back mode was used taking into account the 2 γ -rays only of neighboring crystals and not the diagonal ones. To know the initial energy of the γ -ray, it is sufficient to sum up the energies that are detected by the central contacts (ECC) of the

Energy (MeV)	Intensity
0.1218	28.67
0.2447	8.37
0.3443	27.65
0.4111	2.29
0.4440	3.15
0.7789	12.99
0.8674	4.26
0.9641	14.54
1.0858	10.15
1.1120	13.44
1.4080	20.86

Table 4.5: Energies and intensities of the γ -rays emitted from an ^{152}Eu source.Figure 4.16: γ spectrum of the ^{152}Eu source used for the calibration of the EXOGAM clovers. Resolution is noted to be 3keV.

two fired crystals. Thanks to this treatment, the efficiency increases from 6% to 8% at 1 MeV, Figure 4.17 presents the detection efficiency as a function of the energy. These experimental points are adjusted according to the function below:

$$e = e^{a_0 + a_1 \ln \frac{E}{E_0} + a_2 (\ln \frac{E}{E_0})^2} \quad (4.11)$$

where a_0, a_1, a_2 and E_0 are the adjustment parameters.

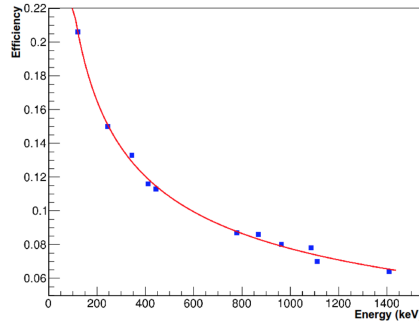


Figure 4.17: Efficiency curve for all EXOGAM clovers after the add-back. Errors are smaller than the points.

Doppler correction

A lower energy will be measured for a γ -ray hitting the detector at backward angles while the γ -rays that are emitted forward will deposit a higher energy. This phenomenon is known as Doppler shift. There is another phenomenon that may occur that is the Doppler broadening. Doppler broadening is the spread in measured energy caused when γ -rays from moving nuclei are observed using a stationary detector whose opening angle is large enough to accept varying angles of incidence. The effect gets worse as the velocity of the nucleus increases and as the detector size (and hence opening angle seen by the projectile nucleus) is increased. Corrections of the Doppler broadening are not included and that may explain the 80 keV resolution that we get instead of the 3 keV nominal one. The energy that we observe is given as follows:

$$E_{det} = \frac{E_0}{\gamma (1 - \beta \cos(\theta))} \quad (4.12)$$

where E_{det} is the energy detected by EXOGAM, E_0 the energy of the emitted γ radiation, θ the angle between the direction of the emitter nucleus and that of the emission of the γ -ray and γ and β the relativistic Lorentz factors. All measured energies are therefore corrected according to the above equation. During the runs of this experiment we used different β due to slightly different beam tuning in between the target changes and are presented in the Table 4.6.

Beam	Target	β
^{56}Ni	CD_2	0.245
^{56}Ni	CH_2	0.263

Table 4.6: The β of the beam that was used during the runs of each target.

4.7 Energy Losses

The recovery of the initial energy of the target-like ejectile is required. Hence, we need to take into account the dead layer of the silicon detectors as well as the kinetic energy loss that the particle has in the target. The nominal dead layer thickness was $1\ \mu\text{m}$ of silicon and $0.5\ \mu\text{m}$ of aluminium, respectively, for the Barrel and the Hyball, as well as $0.7\ \mu\text{m}$ of aluminium for each MUST2 telescope. As for the target, we consider only half the thickness assuming that on average the reaction takes place in the middle of the target. The effective thickness of the target and the detector dead layer is calculated on an event by event basis depending on the beam interaction point and the scattering angle. Then, the energy losses in the detector dead layer and the target are estimated using energy loss tables, for instance LISE++ [66] or GEANT4 [67] tables, in order to recover the initial energy of the ejectile. Thus the final measured energy in the laboratory system E_{lab} will be equal to:

$$E_{lab} = E_{Must2} + E_{loss}(target) + E_{loss}(deadlayer) \quad (4.13)$$

The energy loss tables used for the reconstruction of the energies were extracted by the GEANT4 simulations that we made by using the NPTOOL framework [68]. For each reaction and each target, a different simulation has been made generating those GEANT4 energy loss tables and found to be in agreement with tables extracted by LISE++. More details about the simulations can be found in the following section.

4.8 Simulation for the reactions of interest

In this section we present the results obtained by simulations done after the experiment using the NPTOOL framework [68]. NPTool (Nuclear Physics Tool), is an open source data analysis and Monte Carlo simulation package for low-energy nuclear physics experiments. The NPTool package aims to offer an unified framework for preparing and analysing complex experiments, making an efficient use of Geant4 and ROOT [69] toolkits. In this work we performed post-

experimental simulations, where we took into account the real beam position, as well as the measured position of the detectors and target. Consequently, we can compare the simulated data with those obtained from the experiment.

4.8.1 Kinematic lines and resolution

We performed the analysis of the simulations for all the reactions of interest in this work by using a flat cross section. For the initial information on the beam energy and position we had to provide the experimental resolutions. The energy of the beam measured during the experiment

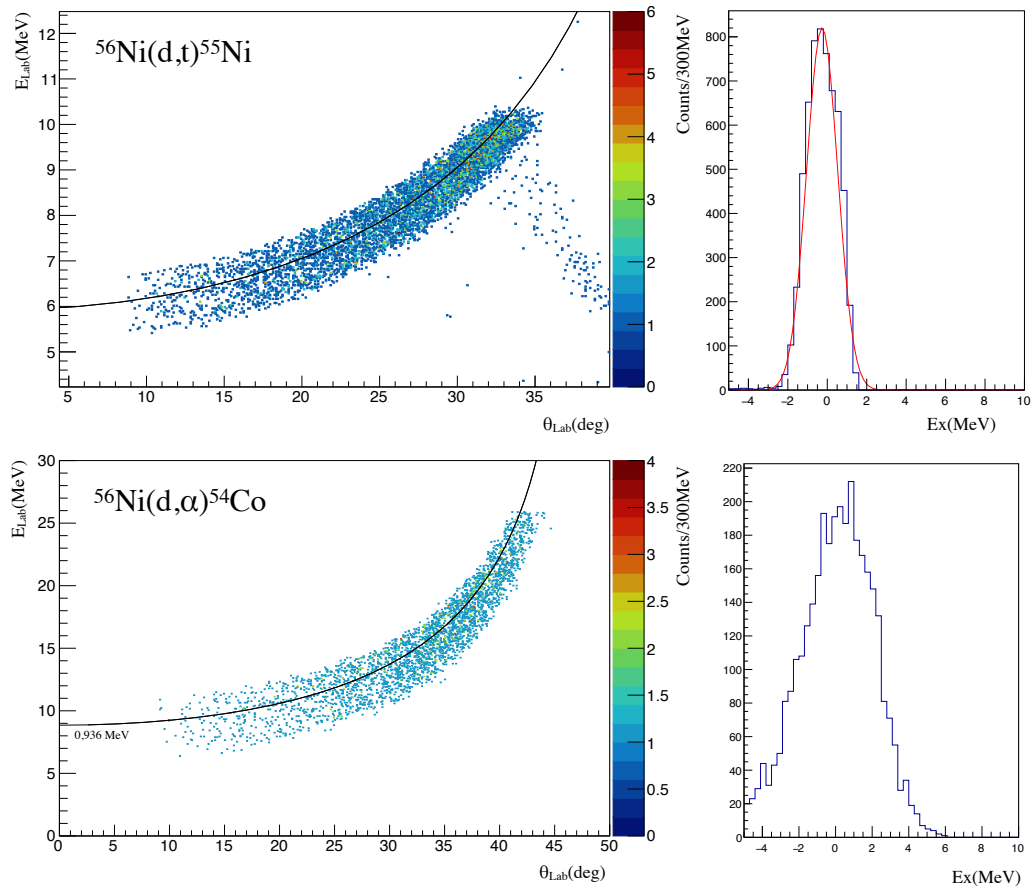


Figure 4.18: Left: Simulated kinematic lines for the (d,t) and (d, α) reaction. Right: The corresponding excitation energy spectra. The Gaussian fit on the (d,t) ground state provides the expected energy resolution.

was $E_{\text{Beam}}=1703$ keV, while we also took into account a $\sigma = \pm 26$ keV corresponding mostly on

the energy resolution of the CATS detectors that are not being simulated. Additionally, an error in the angle was also included with $\sigma = \pm 1^\circ$. The detector resolution is also included with the MUST2_{DSSSD} having an energy resolution of 52 keV (FWHM), the CsI resolution being 188 keV (FWHM) and the time resolution of the detector is 500 ps. For the (d,t) and (d, α) reactions we use the CD₂ target (7 mg/cm²). Similarly, for the (p,d) reaction we used the CH₂ target (6.9 mg/cm²). By the kinematic line information we can additionally estimate the straggling effect

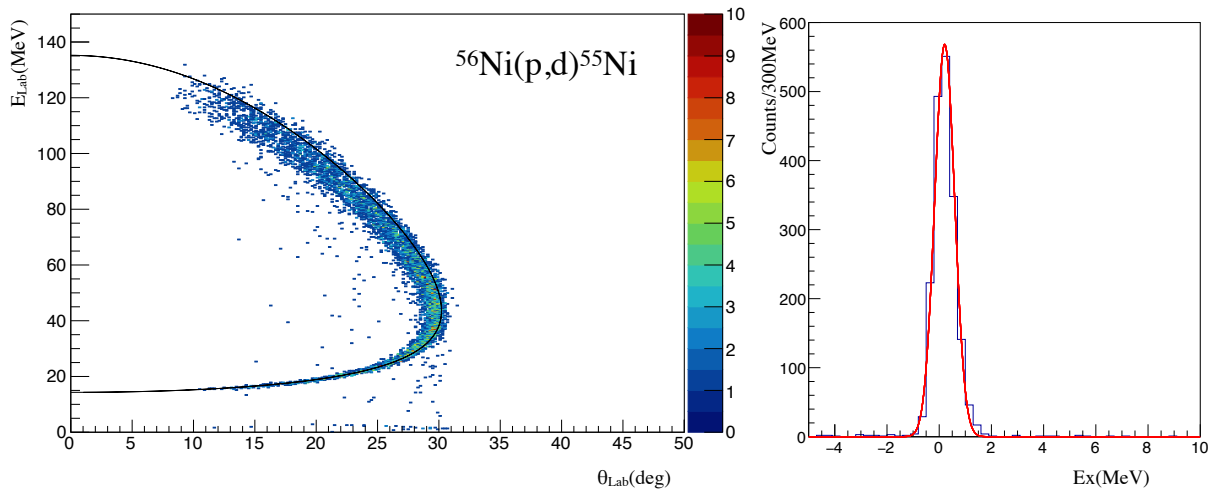


Figure 4.19: Left: Simulated kinematic line for the (p,d) reaction. Right: The corresponding excitation energy spectrum. The Gaussian fit on the (p,d) ground state provides the expected energy resolution.

of the light particles with respect to their energy. In the following Figure 4.18 we present the kinematic lines (d,t) and (d, α) reaction that are expected to show the most of this effect. The kinematic line of the (p,d) reaction is presented in Figure 4.19.

On the right side of each figure we present the excitation energy spectrum. From the excitation energy spectra we can obtain information about the expected energy resolution of the ground states for the (d,t) and (p,d) reaction. In the following table Table 4.7 we present the reactions of interest and the corresponding resolutions obtained by the simulations. For the (d, α) reaction the simulation has been done for the 0.936 MeV first excited state.

Reaction	Target	σ (keV)	FWHM
(d,t)	CD_2	800	1620
(p,d)	CH_2	450	940

Table 4.7: The σ of the ground state obtained by simulation for each of the reactions.

5

Results and Discussion

Contents

5.1	The (p,d) & (d,t) reactions	79
5.1.1	Kinematic Lines	80
5.1.2	Excitation Energies	81
5.1.3	Particle-Gamma Coincidences	82
5.1.4	Background Subtraction	87
5.1.5	Angular Distribution	88
5.1.6	Theoretical Analysis	91
5.1.7	Results	98
5.1.8	Discussion	99
5.2	The $^{56}\text{Ni}(\text{d},\alpha)^{54}\text{Co}$ reaction	105
5.2.1	Kinematic Lines and Excitation Energy spectra	105
5.2.2	Background Subtraction	105
5.2.3	Upper Limit Cross Section	108
5.2.4	Discussion	110

Part I

One nucleon-transfer reactions

5.1 The (p,d) & (d,t) reactions

In this chapter, we present the kinematics of the light ejectiles as well as the excitation energy spectra of the heavy ejectiles for the different one nucleon transfer reactions that we have studied. These data are the result of the various analysis steps described in the previous chapter 4. We provide information on the background associated with each of these reactions, based on the contribution of the carbon in each target.

The angular distributions for the one neutron pick up reactions are presented as well and are being compared with Distorted Wave Born Approximation (DWBA) calculations. The ratio in between the calculation and the experimental result gives us the spectroscopic factor of each energy level as discussed in chapter 2, leading on conclusions about the hole- and particle-states populated by this reaction in the residual nucleus. Finally we discuss the results, adding information on the $N = 28$ shell closure.

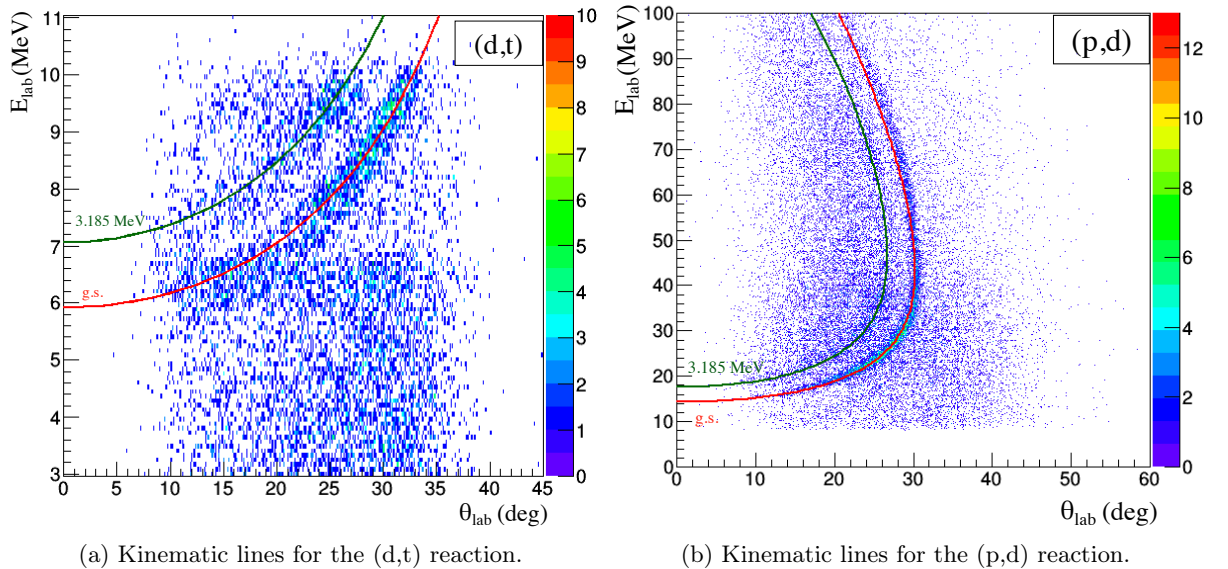


Figure 5.1: Kinematic lines of one-nucleon transfer reactions. Left: for the (d,t). Right: of the (p,d) reactions. Red line is the theoretical expected kinematic line for the ground state while with green the excited state of 3.185 MeV is being depicted.

5.1.1 Kinematic Lines

The kinematic lines are unique for any two-body reaction. They give the identification of the residue and consequently the identification of the populated levels (see section 2.4). Hereby, we present the kinematics obtained for the one nucleon transfer reactions (d,t) and (p,d) at 30 MeV per nucleon on a 7 mg/cm² CD₂ and 6.8 mg/cm² CH₂ target respectively (see Figure 5.1a and Figure 5.1b).

These kinematics link the energy and the scattering angle of the triton and the deuteron accordingly at the output channel and depict the energy conservation and momentum of the reaction in the laboratory system.

The tritons are selected in the first layer of the MUST2 telescopes using the ΔE -T spectrum, while for the deuterons we take into account also the energy in the CsI crystals by means of the DE- E_{CsI} spectrum. In the two figures (Figure 5.1a and Figure 5.1b), the experimental kinematic lines of the one nucleon transfer reaction show the population of the ground state and also allows us to compare the two different reactions populating the same nucleus ⁵⁵Ni. In these figures, with red and green we identify the calculated in theory ground state and 3.185 MeV excited state respectively. For the (p,d) reaction we have a full coverage of the MUST2 telescopes. Consequentially, we cover all the angles in the center of mass system for the (p,d) reaction in comparison with the (d,t) reaction in which only a range of 5°–17° are covered in the center of mass.¹

By the theoretical relativistic kinematics of the two reactions we can calculate the *L matching* for each of them by using the following equation:

$$L \approx (k_t - k_d)r_0A^{1/3}, \quad (5.1)$$

for the (d,t) reaction and:

$$L \approx (k_d - k_p)r_0A^{1/3}, \quad (5.2)$$

for the (p,d) reaction. Where k is related to the initial and final impulses by $p = \hbar k$ and with $r_0A^{1/3}$ the radius of the target nucleus. In this formula, we consider that the reaction takes place on the surface of the target nucleus of the direct reaction assumption. The L matched for each of the reaction calculated with p in MeV/c, $\hbar c = 197\text{MeV fm}$ and $r_0 = 1.25\text{ fm}$, can be seen in Table 5.1 for the ground state of each reaction and $\theta=0^\circ$. This is an approximation since at 30 MeV per nucleon incident energy the reaction is also sensitive to the interior of the nucleus,

¹The rest of the information on the (d,t) reaction lies on the Barrel, part of TIARA detector which was not analysed here.

	(d,t)	(p,d)
$L_{matched}$	$1.67 \approx 2$	$0.18 \approx 0$

Table 5.1: L matching for the (d,t) and the (p,d) reaction for the ground states and $\theta=0^\circ$ forward angle.

particularly in the case of the (p,d) reaction.

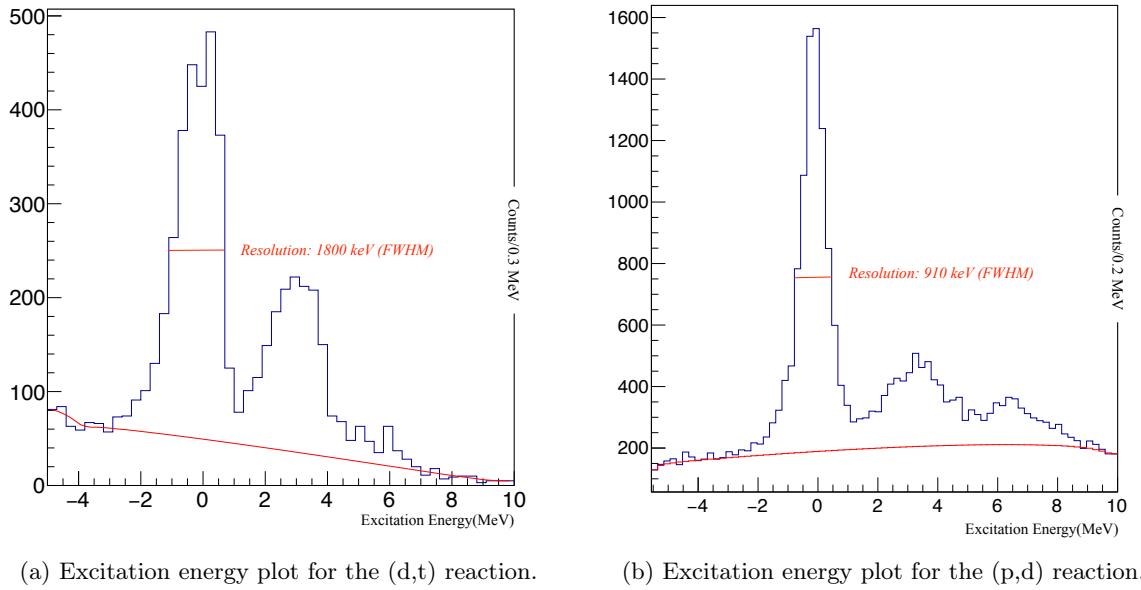


Figure 5.2: The excitation energy plots for both one nucleon transfer. With red, the carbon background contribution is indicated and at the FWHM the resolution of each ground state. More about the carbon background subtraction can be found in section 5.1.4.

5.1.2 Excitation Energies

The excitation energy of the residue heavy nucleus is calculated by taking into account the energy losses in the target as well as in the detector, more details can be found in the previous chapter in section 4.7.

For the (d,t) reaction the excitation energy spectrum is shown in Figure 5.2a. The separation in between the ground state and the excited states is clear with the ground state peak resolution being 1.8 MeV (FWHM) and in a relatively good agreement with the simulation if we consider the uncertainty on the beam energy resolution in the simulations. The CD_2 target has a thickness

of 7 mg/cm^2 , this adds the effect of straggling of the light ejectile in the target and that is why the energy resolution is not the one expected for MUST2 detector.

For the (p,d) reaction the excitation energy spectrum from Figure 5.2b shows the ground state separated from the excited states as well, with the energy resolution of the ground state of 910 keV (FWHM). Due to their larger energy the deuterons reach the second layer of the detector, which affects the final resolution for these particles ($\Delta E = \sqrt{\Delta E_{DSSD}^2 + \Delta E_{CSI}^2}$).

In both spectra the energy resolution does not allow separation between the excited states. From the list of levels of ^{55}Ni taken by the national nuclear data center NNDC and shown in Figure 5.3 we obtain information about the excited states of ^{55}Ni from previous experiments. Not much is known for this nucleus and additionally, the known energy levels are separated only for a few hundreds of keV. The database is quite sparse concerning ^{55}Ni and many spin assignments are not confirmed. A recent study of $^{56}\text{Ni}(p,d)$ was published by B. Tsang's team at MSU using the HIRA detector in coincidence with the S800 spectrometer [26]. Their data allow them to extract the spectroscopic factors of the ground state, the two first excited states are tentatively assigned to the $2p_{3/2}$ and $2s_{1/2}$ single particle state configuration. The result was obtained solely by particle identification and as mentioned in the paper the energy resolution did not allow the identification of the higher states. The levels and spin assignment obtained by this experiment can be seen in Table 5.2. The energy assigned to the third expected particle state still requires further discussion and investigation.

To improve this result and particularly the energy resolution, we need to use particle- γ coincidences to identify the main populated states.

E(Level)	J^π	L	Comments
0.0	$7/2^-$	3	Configuration: $1f_{7/2}$ hole state
2.09	$3/2^-$	1	Configuration: $2p_{3/2}$ particle state
3.18	$1/2^+$	0	Configuration: $2s_{1/2}$ hole state
(3.752)	$3/2^+$	2	Configuration: $1d_{3/2}$ hole state

Table 5.2: Experimental information on the states $1f_{7/2}$, $2p_{3/2}$ and $2s_{1/2}$ as presented in the ^{56}Ni paper by A.Sanetullaev et al. [26].

5.1.3 Particle-Gamma Coincidences

The heavy residue is considered to de-excite and emits γ photons instantly. However, this heavy residue has a certain velocity with a certain β . According to the theory of special relativity, the heavy residue not being stopped, the distribution of γ photons will not be isotropic in the

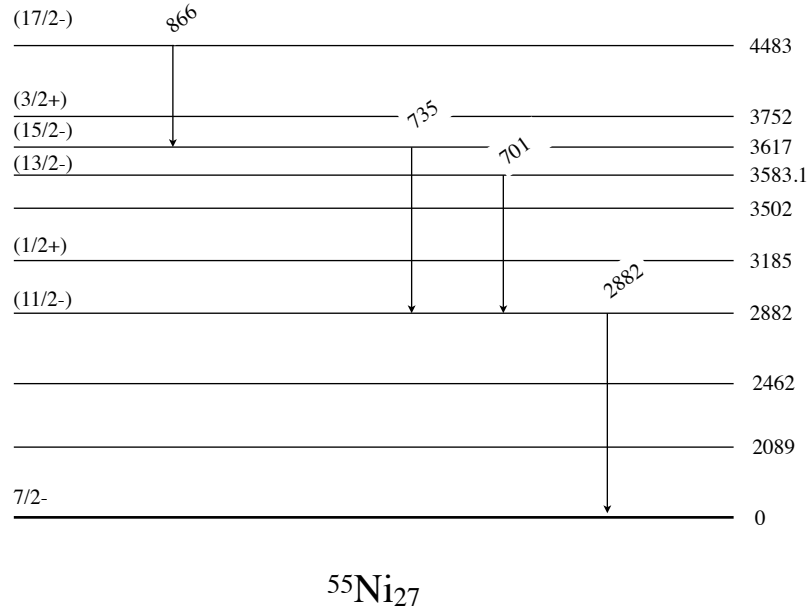


Figure 5.3: Level scheme of ^{55}Ni based on the national nuclear data center (NNDC) and the known γ -rays from the evaluated data.

reference system of the laboratory because of the Lorentz boost. According to [70], the emitted angles of γ tracks in the laboratory reference frame (θ_{lab}) at the angles of emission of the photons in the reference frame of the nucleus (θ_{nuc}) are being associated according to:

$$\cos(\theta_{lab}) = \frac{\cos(\theta_{nuc}) + \beta}{1 + \beta \cos(\theta_{nuc})} \quad (5.3)$$

Depending on the type of transition (M1,E1) the angular distribution of the γ will be different. The γ efficiency will also be modified accordingly. In our case, we did not correct for these effects because the spins of the states are not well assigned. We took into account a larger uncertainty $\pm 10\%$ in the population of the state to account for the missing information.

By gating on excitation energy for the energy range 1.5 MeV to 4.5 MeV, we can identify the γ -ray corresponding to each energy level transition that each of these reactions populates in the particle- γ coincidence spectrum in Figure 5.4. Some of the γ photons resulting from transitions between excited states of ^{55}Ni (Figure 5.3) are well identified on the spectrum with a resolution of 80 keV.

For the (d,t) and (p,d) reactions we observe the following transitions:

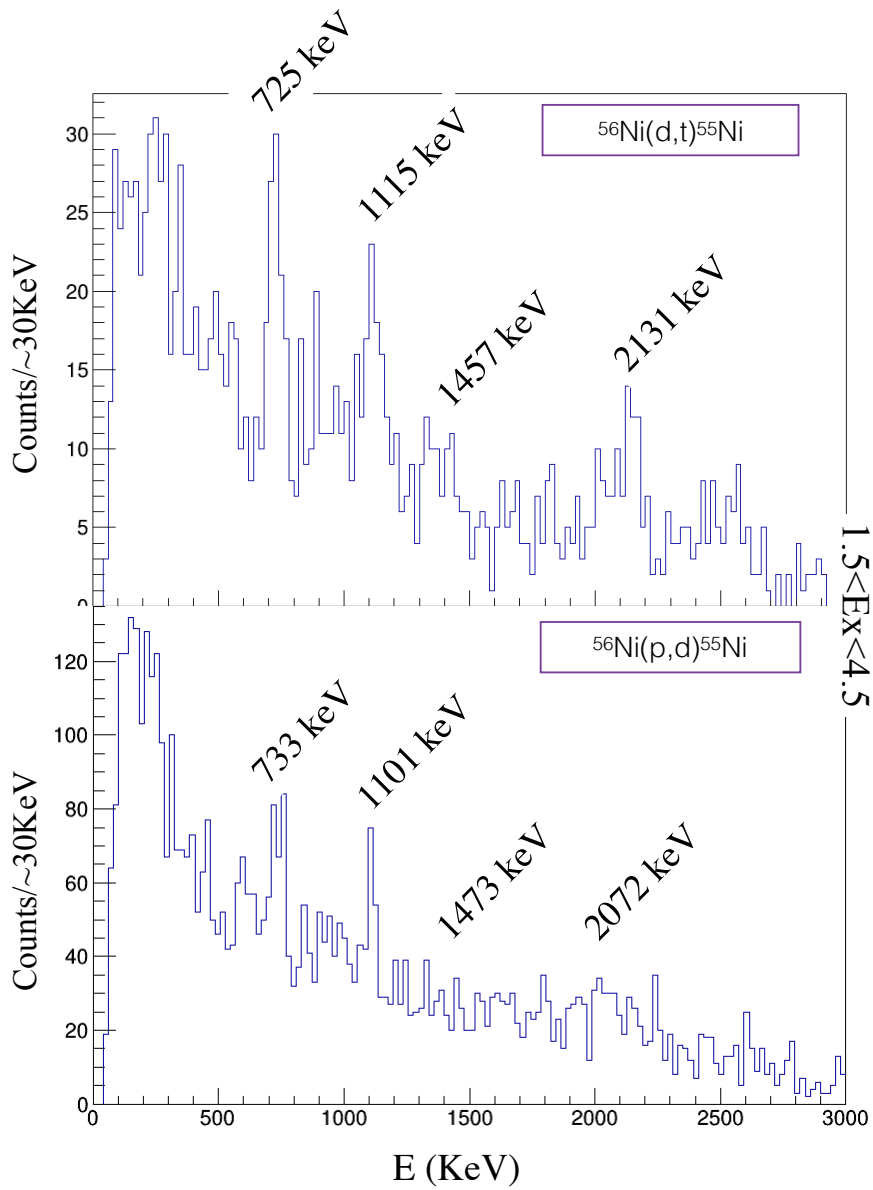


Figure 5.4: Particle-Gamma coincidences for both one nucleon transfer reactions. (no efficiency correction)

- 735 keV: While both the 701 keV and the 735 keV γ -rays are known already (Figure 5.3) the mean of the Gaussian fit for this peak corresponds to the 735 transition.

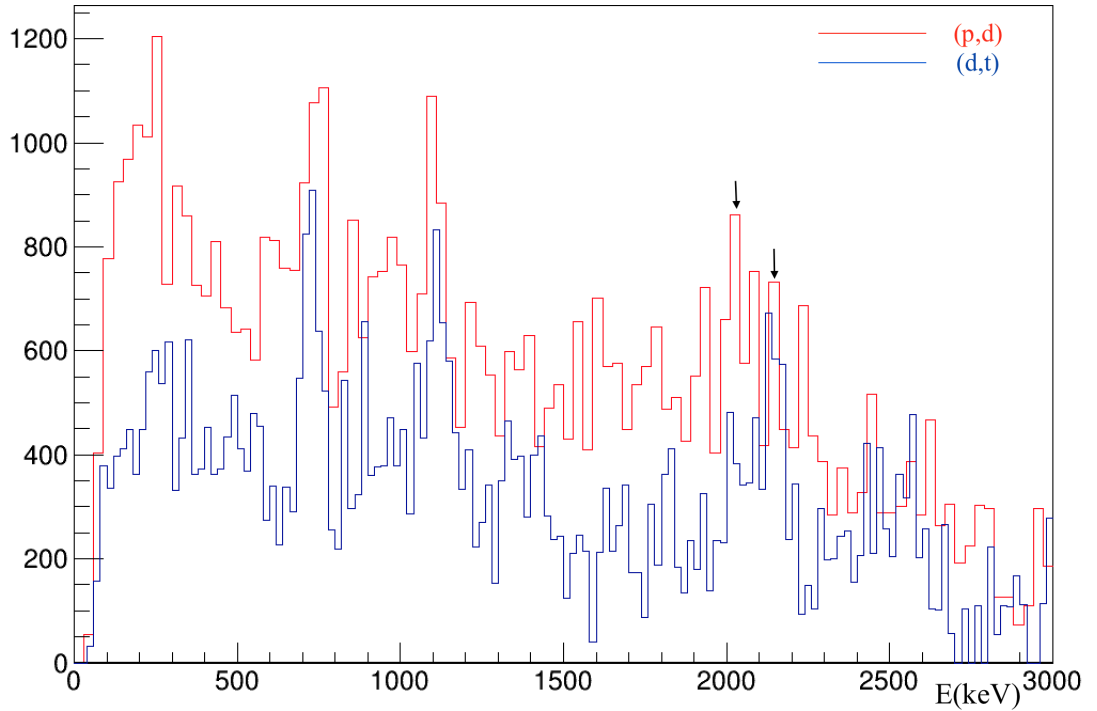


Figure 5.5: Both Gamma Spectra efficiency corrected and superimposed. The (d,t) reaction is scaled to be 3 times more to be comparable with the (p,d) statistics. With black arrows we note the 2100 keV peak and a probable doublet that its information are unknown.

- 1100 keV: Even though the level that this transition originates from 3.185 MeV is known and its spin assignment has been also addressed in the recent publication of A.Sanetullaev *et al.* [26] the γ -ray is not part of the evaluated data.
- 1450 keV: This transition is mostly visible in the γ -triton coincidence for the (d,t) reaction and not for the (p,d) reaction. While the two reactions end up in the same nucleus the transitions favored in each of them might differ due to the angular momentum selectivity.
- 2100 keV: The γ -ray corresponding to the direct decay of the $2s_{1/2}$ state to the ground state is being fed by the 1100 keV and is clearer in the (d,t) spectrum than in the (p,d). One can also observe at least one more peak in the region close to 2200 keV. We are not able to identify the corresponding energy due to the lack of information in ^{55}Ni (Figure 5.5).
- 2882 keV: There are some small hints of the 2882 keV peak in the γ -deuteron coincidence for the (p,d) reaction. This γ -ray, has been already observed and included in the nuclear

data base but in this experiment the population seems too small to conclude. The fact that it is also at the end of the efficiency curve does not help its observation.

We identify 3 clear separated γ -rays, the 735, 1100 and 2100 keV. Among those only the one at 735 keV is indicated in NNDC level scheme. Nevertheless, the corresponding level has been assigned with a very high spin from a previous experiment using the isobaric analog technique [71]. By means of the transfer reaction the most populated states should be the ones that correspond to the single particle states and especially by looking into the L matching of the (d,t) reaction we find that the reaction favors L=2 transitions at the forward angles. Since the information about the spin assignment is noted with parenthesis in NNDC, in this work we suggest this 735 keV γ -ray corresponds to the $d_{3/2}$ expected state. The observed γ -rays 1100 keV and 2100 keV in coincidence with the light particles correspond to the transitions in between the first and second excited states in ^{55}Ni . Based on the level scheme of ^{55}Ni from NNDC, the 1100 keV and 2100 keV transitions are not in the validated data but the peaks are present in the γ spectrum obtained. By using this information provided by the γ -rays we exploit the finer energy resolution of the γ -ray detector compared to the resolution in excitation energy by the charged particle detector.

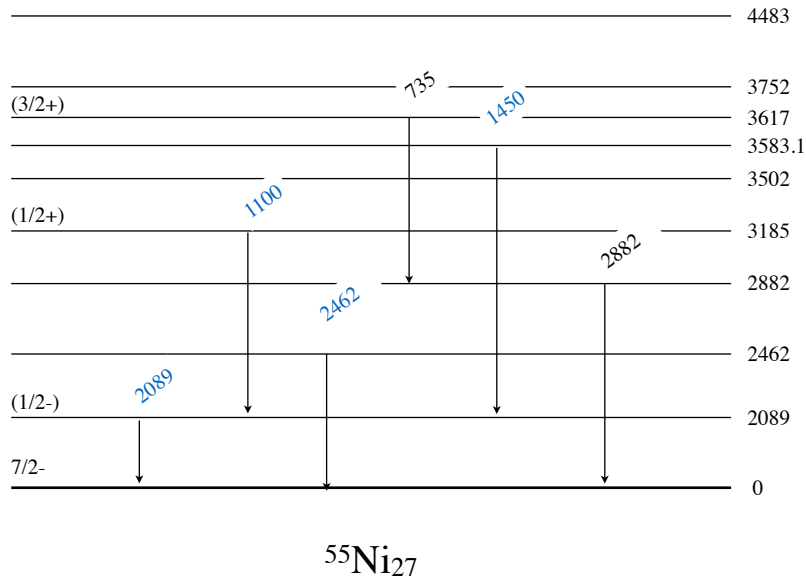


Figure 5.6: Levels and γ -rays observed in this experiment. The new ones are indicated with blue and the ones already known with black.

As a check we obtain no γ -rays in coincidence with the ground state, as can be seen in

Figure 5.7 for the (d,t) reaction and that can confirm that we have selected the state populated by our reaction. The γ yields are obtained by a Gaussian fit which gives the number of counts that are used to calculate the relative population for each state. An example of the Gaussian fit on the 725 keV γ -ray can be seen in Figure 5.8. To compare with the particle information of the ground state we correct from the γ efficiency that have been already detailed in the previous chapter 4.

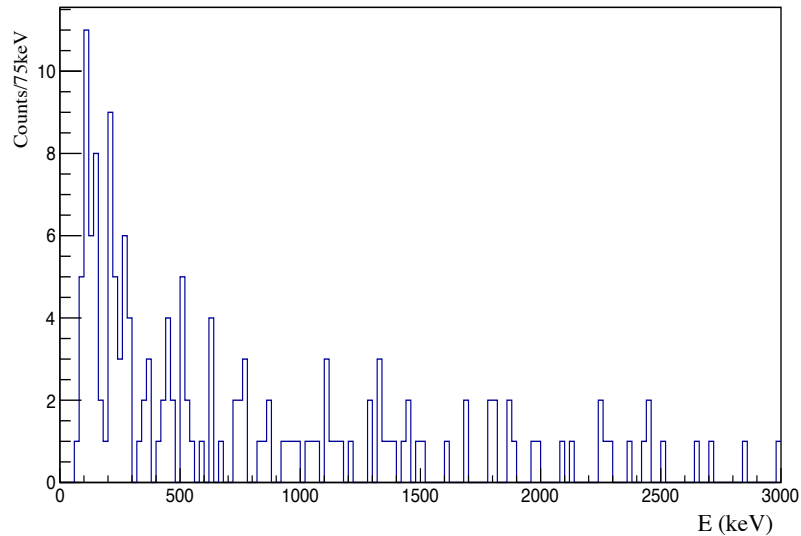


Figure 5.7: γ spectrum gated on the ground state for the (d,t) reaction.

5.1.4 Background Subtraction

During the experiment, measurements with a carbon target were performed to estimate possible contamination by events resulting from the reaction of the ^{56}Ni beam on the carbon of the CD_2 and CH_2 targets that emitted a triton or a deuteron accordingly at forward angles. The shape of the carbon background can be modeled satisfactorily at low excitation energy ($-5 \text{ MeV} < E_x < 5 \text{ MeV}$) by a first-order polynomial as a function of the excitation energy for the angular range corresponding to the MUST2 telescopes. In the following analysis, we will always subtract this fitted carbon background to obtain the excitation energy spectra from the MUST2 telescopes. We can also reasonably assume that the observed contribution for negative excitation energies comes from reactions on carbon.

It is of great importance to subtract the background over the angular range that we use for the extraction of the angular distribution. Thus, we fit the shape of the carbon background analyzed

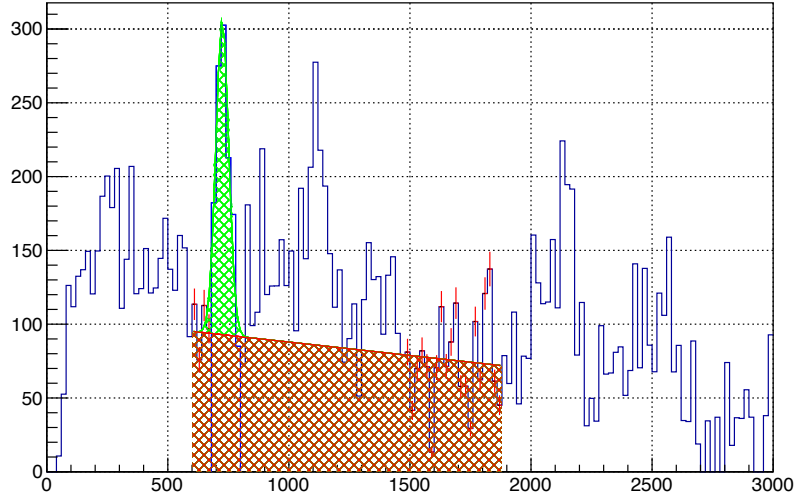


Figure 5.8: Efficiency corrected γ spectrum with an example of the Gaussian fit on the 725 keV peak.

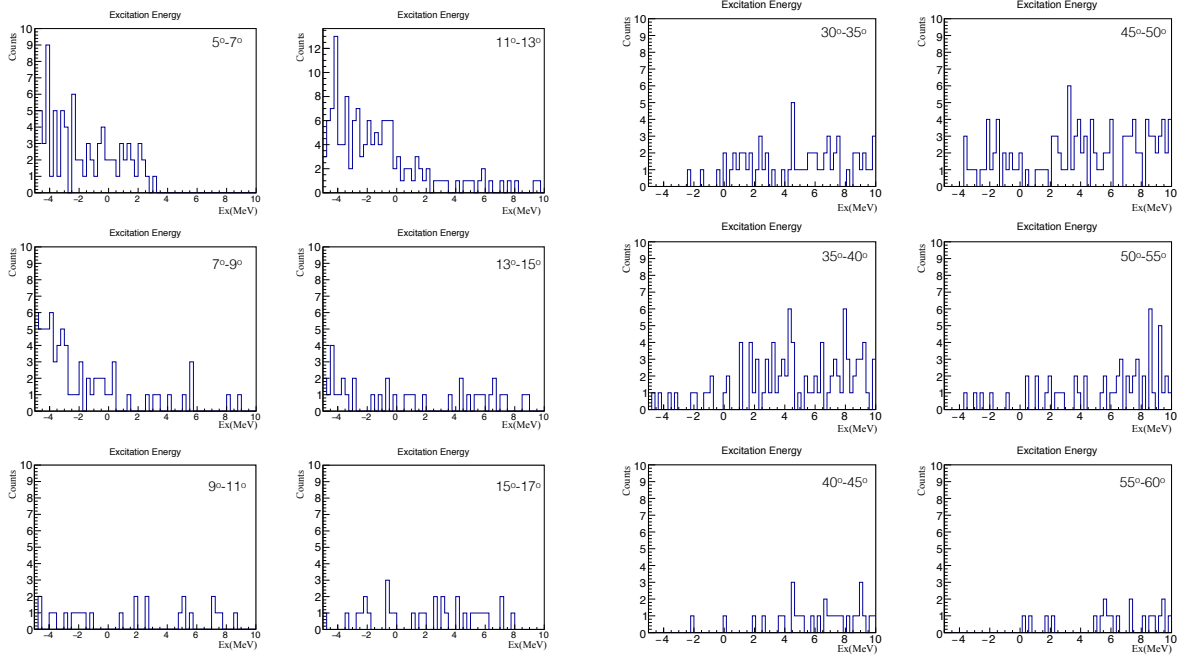
for the (d,t) and the (p,d) reaction. In Figure 5.9a, there is the example of the (d,t) excitation energy for the angular range $5^\circ-17^\circ$ angle with a step of 2° in the center of mass on the carbon target and in Figure 5.9b there is the example of the (p,d) excitation energy for the angular range $30^\circ-60^\circ$ angle with a step of 5° in the center of mass on the carbon target. We observe that the C background changes angle by angle so we fit it accordingly for each angular range. Additionally, we can use the C target to confirm that the γ transition taken into account in the previous section 5.1.3 originate indeed by the one nucleon transfer reactions. Thus, we observe in Figure 5.10, the γ spectrum obtained and in this spectrum, there are no peaks corresponding to the studied transitions of ^{55}Ni .

5.1.5 Angular Distribution

We want to measure the differential cross section for $N_{^{56}\text{Ni}}$ incoming beam particles hitting a target with N_{target} protons or deuterons per cm^2 . The differential cross section is given by:

$$\frac{d\sigma}{d\Omega} = \frac{N(\theta_{\text{CM}})}{N_{^{56}\text{Ni}}N_{\text{target}}\epsilon_{\text{det}}\Delta\Omega} \quad (5.4)$$

Where $N_{^{56}\text{Ni}}$ the number of nuclei of the beam that reach the target after passing through



(a) Excitation energy of (d,t) reaction analyzed for a Carbon target in a θ_{cm} range.

(b) Excitation energy of (p,d) reaction analyzed for a Carbon target in a θ_{cm} range.

Figure 5.9: Carbon excitation energy plots for theta cm range from 5-17 with a step of 2° for the (d,t) and $30^\circ-60^\circ$ with a step of 5° for the (p,d) reaction.

CATS1 and CATS2 given the information from the TAC ².

ϵ_{det} corresponds to the geometric efficiency of MUST2 which we determine from simulations and in that case we can extract it from:

$$\epsilon_{det} = \frac{N_{det}(\theta_{CM})}{N_{sim}(\theta_{CM})} \quad (5.5)$$

with $N_{det}(\theta_{CM})$ the number of particles detected from MUST2 and $N_{sim}(\theta_{CM})$ the number of particles generated in a given angular interval and for given excitation energy. In this work we determine the $\epsilon_{det} \times \Delta\Omega$ for a given angular interval and for the reaction of interest by using a Monte-Carlo simulation carried out with the framework NPTool [68] :

²The TAC gives the time of flight, measured between the cyclotron radio-frequency and the first CATS detector.

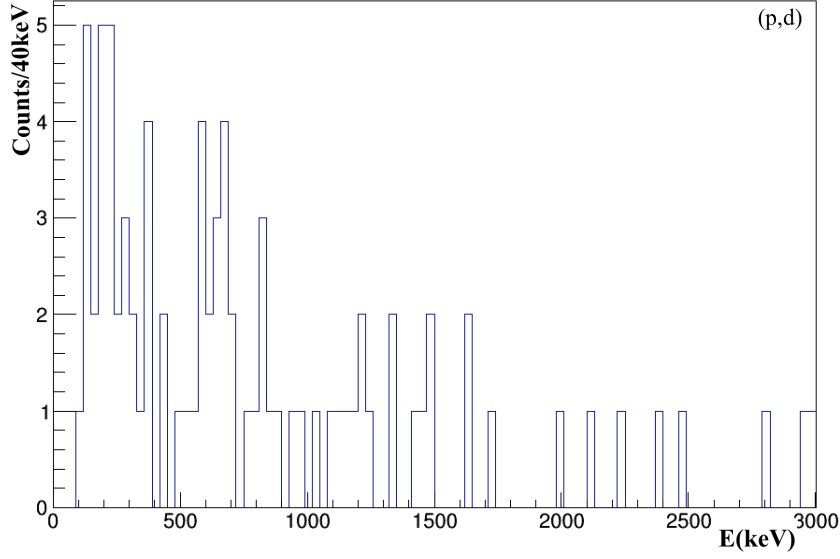


Figure 5.10: Deuteron- γ coincidences with the carbon target. The gammas of interest are not visible in this spectrum.

$$\epsilon_{det} \times \Delta\Omega = 4\pi \frac{N_{det}(\theta(CM))}{N_{sim}(4\pi)} \quad (5.6)$$

In that case $N_{sim}(4\pi)$ corresponds to the total number of particles generated by the simulation for the given reaction for an isotropic emission.

Uncertainties

The uncertainties that contribute in the calculation are mostly statistical from the number of detected particles and the beam number, and can be described as:

$$\left(\frac{d\sigma}{\sigma}\right)^2 = \left(\frac{dN}{N}\right)^2 + \left(\frac{dN_{56Ni}}{N_{56Ni}}\right)^2 + \left(\frac{dN_{target}}{N_{target}}\right)^2 \Rightarrow d\sigma^2 = \sigma^2 \left[\left(\frac{dN}{N}\right)^2 + \left(\frac{dN_{56Ni}}{N_{56Ni}}\right)^2 + \left(\frac{dN_{target}}{N_{target}}\right)^2 \right] \quad (5.7)$$

$$d\sigma = \sigma \sqrt{\frac{1}{N} + \frac{1}{N_{56Ni}} + \frac{1}{N_{target}}} \quad (5.8)$$

Then additional uncertainties may come from the target thickness since it is not measured during the experiment but taken from the manufacturer. Thus, we take into account a systematic error of 10% due to the estimated target thickness and due to the fact that the exact position of the

target is also estimated by taking into account the tilt towards the beam axis.

Population of the levels of interest

For measuring the $N_{det}(\theta_{CM})$, number of particles detected in MUST2 in a certain angular interval we plot the excitation energy for a certain θ_{CM} range for a certain step. As said before for the (d,t) reaction we can measure the excitation energy that leads to the angular distribution from 5° to 17° angular range and we select a step of 2° as it can be seen in Figure 5.11. A combination of Gaussian fits is used to verify the parameters extracted by the γ -rays by drawing the integral of each state, following the expression below:

$$I = D\sqrt{2\pi}\sigma A, \quad (5.9)$$

where $D = \frac{\Delta x}{b}$, in which Δx the width and b the binning of the spectrum, σ and A the Gaussian parameters. For the ground state we use the expected σ from the simulation since the resolution of the peak is in good agreement at the FWHM. As for the excited states, we used the σ obtained from the ground state. For the (p,d) reactions we have full angular coverage starting from 10° and that allows us to measure the excitation energy and the angular distribution from 10° to 60° as seen in Figure 5.12 and Fig 5.13. For the fit of each state in both reactions, we use the additional information given from the particle- γ coincidences to identify each excited state. In the case of the (p,d) reaction, we use the information provided by the relative population of the γ -rays to adjust the limits of the maximum and minimum expected yields for each excited state in the particle spectra.

The three first populated states taken into account are shown in the level scheme of ^{55}Ni (see Figure 5.6). More accurately, we use as parameters for the Gaussian fit the energies of the states obtained by the particle- γ coincidences, the width obtained from the ground state. Additionally, for the (p,d) reaction, we limit the integral as a function of the relative population obtained from the γ -rays. In Figure 5.12 one can see the excitation energies on left and the corresponding particle- γ coincidence on the right. The measured angular distributions can be seen in Figure 5.14a for the (d,t) and Figure 5.14b for the (p,d) reactions.

5.1.6 Theoretical Analysis

Distorted Wave Born Approximation

To be able to model transfer reaction cross sections several types of models have been developed, a description of which can be found in many previous thesis [72, 73] and various sources with

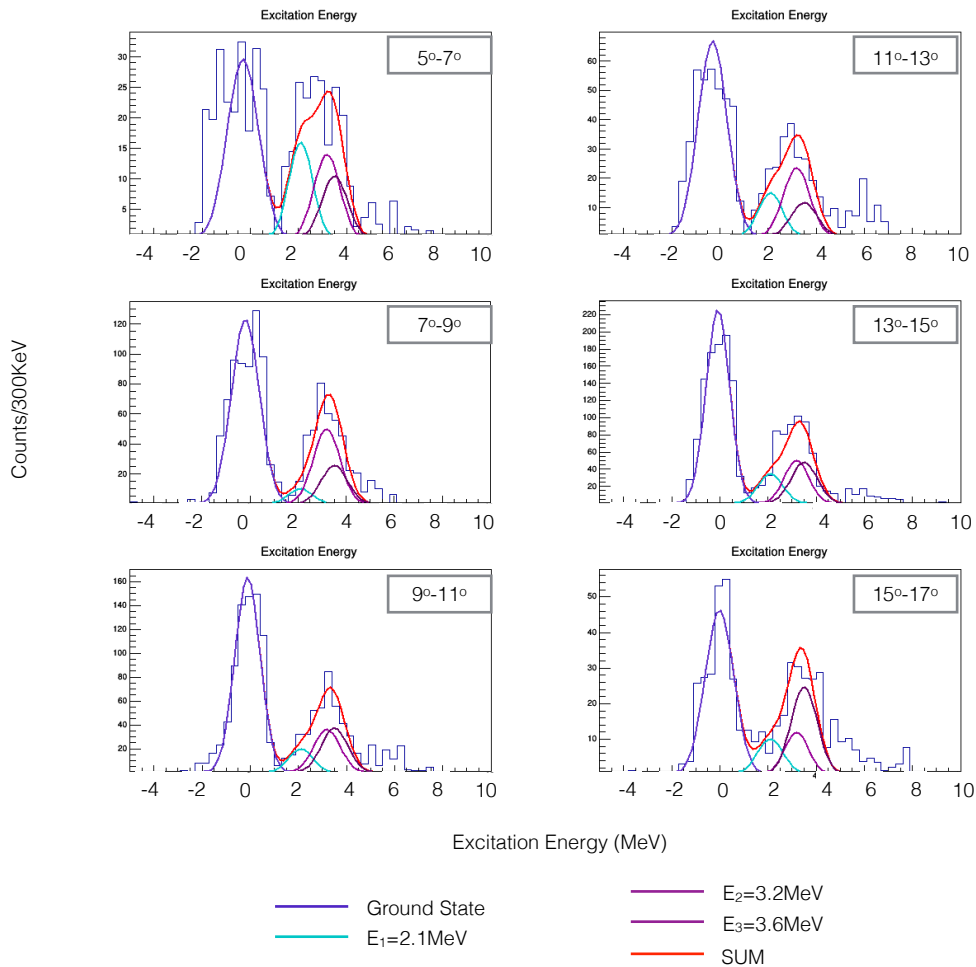


Figure 5.11: Gaussian fit on the excitation energy spectrum for the (d,t) reaction

one of the most typical ones being the *Direct Nuclear Reactions* textbook [74]. The *Distorted Wave Born Approximation* or else DWBA is one of the models which assumes that the biggest part of the reaction is carried out by the elastic diffusion in the entrance channel and the exit channel. The rest of the reaction channels are treated as a perturbation of the elastic channel. As seen by now we describe the transfer reaction of an A nucleus on a deuteron target as $A(d,t)B$ for example, where t the light ejectile and B the residue nucleus. The differential cross section of the above reaction can be described as:

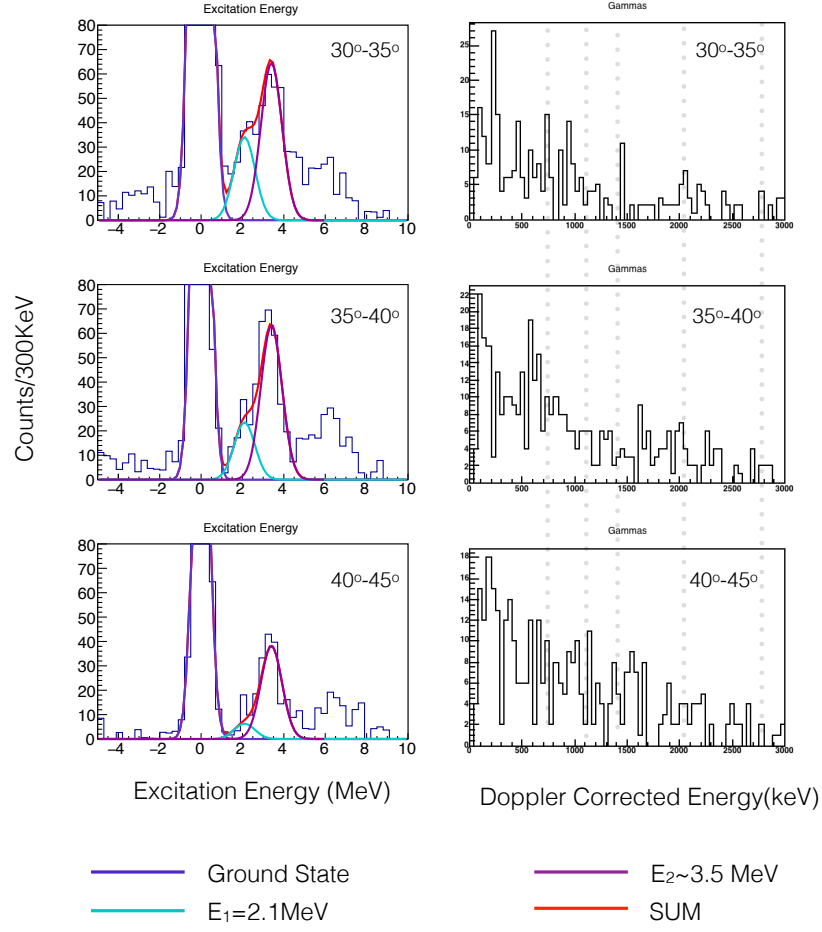


Figure 5.12: Excitation energy plot and particle- γ coincidence for the (p,d) reaction for energy range 30° - 45° with a step of 5° .

$$\frac{d\sigma}{d\omega} = \frac{\mu_A \mu_B}{2\pi \hbar^2} \frac{k_A}{k_B} \frac{1}{2(S_A + 1)(S_d + 1)} \sum_{m_{B,t,A,a}^s} |T_{f_i}^{m_B^s, m_t^s, m_A^s, m_d^s}|^2 \quad (5.10)$$

Where T_{f_i} is the transition matrix element of the considered reaction, μ_A and μ_B are the reduced masses of the input and output channels, k_A and k_B the respective pulses. $S_{A,d}$ are the spins of A and the deuteron and the m^s are the projections of the spin of the different particles taking part in the reaction. The Hamiltonian of the entrance channel can be written:

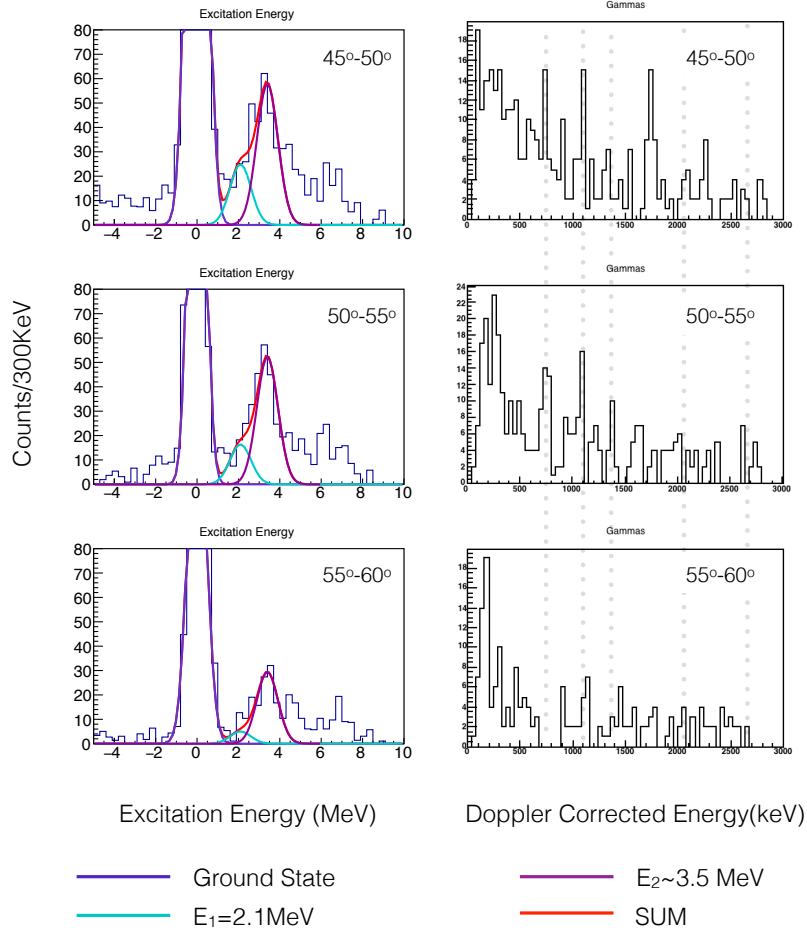


Figure 5.13: Excitation energy plot and particle- γ coincidence for the (p,d) reaction for energy range 45° - 60° with a step of 5° .

$$H = H_d + H_A + K_{Ad} + V_{Ad} \quad (5.11)$$

Where H_A and H_d are the intrinsic Hamiltonians of the nucleus A and the deuteron, K is the kinetic operator and V_{Ad} is the potential of the interaction between the A and the deuteron. This potential is broken down in elastic and inelastic parts:

$$V_{Ad} = U_{Ad} + W_{Ad} \quad (5.12)$$

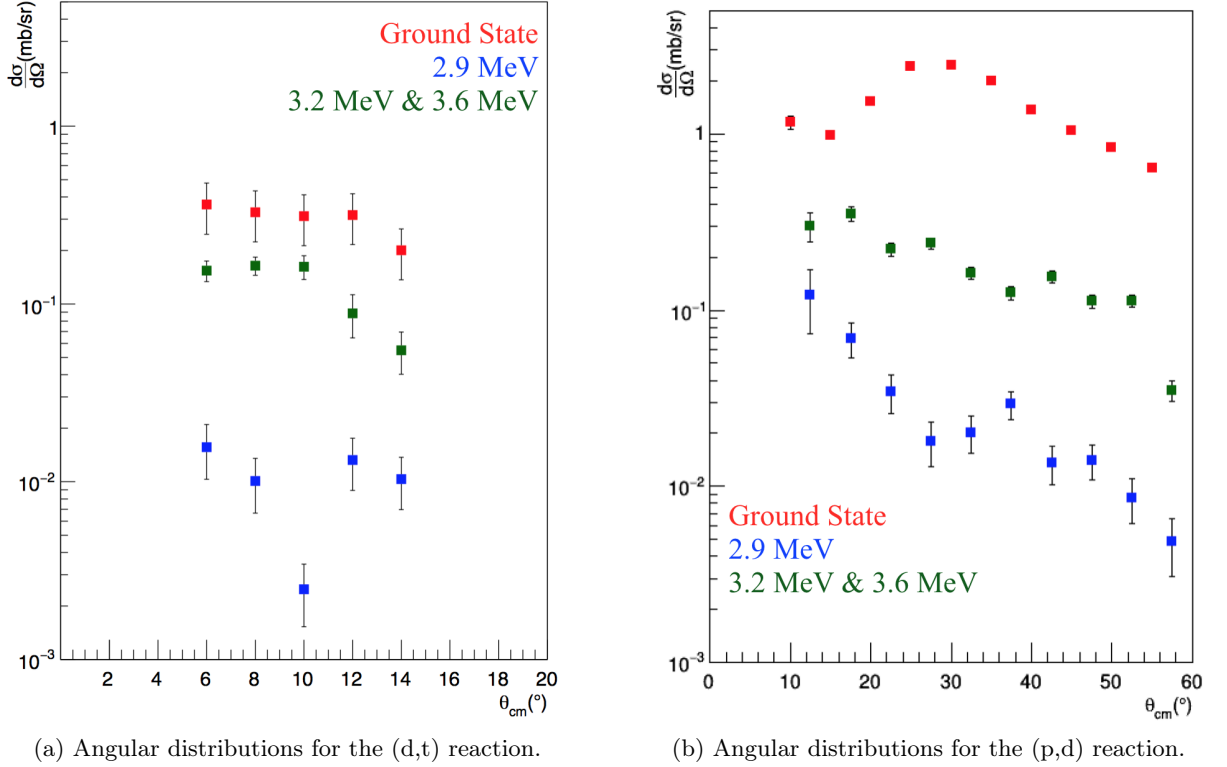


Figure 5.14: Angular distributions for the one nucleon transfers, for the ground state $f_{7/2}$, 2.09 $2p_{3/2}$, 3.185 $2s_{1/2}$ together with the 3.6 $d_{3/2}$

Where U_{Ad} is the optical potential describing the elastic diffusion of nucleus A over the deuteron and W_{Ad} the corresponding residual potential. The distorted waves for the entrance channel are described by χ_{Ad}^{\pm} and correspond to the elastic diffusion:

$$(K_{Ad} + U_{Ad}) | \chi_{Ad}^{\pm} \rangle = \epsilon_{Ad} | \chi_{Ad}^{\pm} \rangle \quad (5.13)$$

In the same way one can express the distorted waves for the output channel. The transition matrix element is then defined by:

$$T_{fi} = \langle \Psi_{Bt}^- | W_{Ad} | \chi_{Ad}^+ \Phi_A \Phi_d \rangle \quad (5.14)$$

where Φ_A and Φ_B are the eigenvalues of the intrinsic Hamiltonians H_A and H_d , respectively and Ψ_{Bt}^- is the state of the total Hamiltonian on the exit channel. Finally, we can describe the entrance nucleus as the residual plus a neutron ($A = B + n$) and thus the potential of the residual

nucleus is commonly reduced to the deuteron-neutron interaction potential expressed in:

$$W_{Ad} = V_{Ad} - U_{Ad} = V_{nd} + (V_{Bd} - U_{Ad}) \simeq V_{nd} \quad (5.15)$$

Afterwards, we can express the matrix element as:

$$T_{f_i}^{DWBA} = \langle \chi_{Bt}^- \Phi_B \Phi_t^- | V_{dn} | \chi_{Ad}^+ \Phi_A \Phi_d \rangle \quad (5.16)$$

Without entering in the detail of the formalism, we can see in this last expression the distorted waves in the entrance and exit channels $\chi^+(R)$ and $\chi^-(R)$ which are calculated with the optical potentials deduced from global parametrisations over different nuclei and energies. We had in fact no elastic diffusion measurements available to fit with other parameters. $\langle \Phi_B | \Phi_A \rangle$ which is the overlap between the n and the residual nucleus. The wave function of the neutron in the nlj state in the nucleus A is calculated in a Woods Saxon potential whose depth is adjusted to reproduce its binding energy. $\langle \Phi_t | V_{dn}(r) | \Phi_d \rangle = D(r)$ is the range function of the deuteron-neutron interaction potential. It has been calculated in the finite range approximation. We have checked that a microscopic description including the S and D states for the d does not change that much the results at these incident energies.

The file presented in appendix B illustrates the structure of a FRESKO input file in the case of the (d,t) reaction and we can see its different &FRESKO, &PARTITION, &POT, &OVERLAP and &COUPLING parts. The parameter iter=1 selects the first order DWBA equivalent calculation for this coupled reaction channels (CRC) code. The parameters kind=7, ip1=1, ip2=-1, ip3=5 describe respectively the finite range option, the prior form, the full complex remnant term calculation and the optical potential taken for this last calculation.

Optical Model

The parameters taken from the optical model potentials for the input and output channel of the DWBA calculations are presented in the following tables Table 5.5 and Table 5.6. For the (d,t) reaction the parameters extracted for the deuteron have been constructed by the sum of the a proton nucleus and a neutron nucleus potential at half the incident energy that is usually called *Adiabatic Distorted Wave Approxiamtion* or ADWA, while the $A = 3$ particle parameters have been taken from the optical potential from Pang et al. [75]. For the (p,d) reaction the parameters of the optical potential used in input channels for the proton are those obtained from the global potential CH89 [76] and for the output channel the parameters of the optical potential used for the deuteron are those obtained from the global potential [77]. In order to take into account the

breakup of the deuteron, the imaginary part of the potential RW0 for the volume term has been set at 5.645 MeV instead of 0.645 MeV in the (p,d) reaction.

Terms	Real			Imaginary		
	V_0 (MeV)	R_{V_0} (fm)	a_{V_0} (fm)	W_0 (MeV)	R_{W_0} (fm)	a_{W_0} (fm)
<i>Volume</i>	90.838	1.191	0.690	5.495	1.220	0.630
<i>Surface</i>	-	-	-	11.467	1.220	0.630
<i>Spin – Orbit</i>	11.800	1.026	0.630	-	-	-

Table 5.3: Input channel parameters for the (d,t).

Terms	Real			Imaginary		
	V_0 (MeV)	R_{V_0} (fm)	a_{V_0} (fm)	W_0 (MeV)	R_{W_0} (fm)	a_{W_0} (fm)
<i>Volume</i>	114.466	1.174	0.84	3.155	1.271	0.84
<i>Surface</i>	-	-	-	17.295	1.271	0.84

Table 5.4: Output channel parameters for the (d,t).

Terms	Real			Imaginary		
	V_0 (MeV)	R_{V_0} (fm)	a_{V_0} (fm)	W_0 (MeV)	R_{W_0} (fm)	a_{W_0} (fm)
<i>Volume</i>	47.065	1.191	0.690	2.147	1.220	0.690
<i>Surface</i>	-	-	-	6.096	1.220	0.69
<i>Spin – Orbit</i>	5.9	1.026	0.630	-	-	-

Table 5.5: Input channel parameters for the (p,d).

Terms	Real			Imaginary		
	V_0 (MeV)	R_{V_0} (fm)	a_{V_0} (fm)	W_0 (MeV)	R_{W_0} (fm)	a_{W_0} (fm)
<i>Volume</i>	89.0	1.170	0.748	5.645	1.325	0.690
<i>Surface</i>	-	-	-	12.146	1.325	0.69
<i>Spin – Orbit</i>	6.67	1.070	0.660	-	-	-

Table 5.6: Output channel parameters for the (p,d).

5.1.7 Results

Hereby, we find the experimental angular distributions measured for the (d,t) reaction in Figure 5.15a and (p,d) reaction in Figure 5.15b. We identify the ground state $f_{7/2}$ with red, the particle state $2p_{3/2}$ with blue and finally the mixture of the two next hole-states $2s_{1/2}$ and $d_{3/2}$ with green.

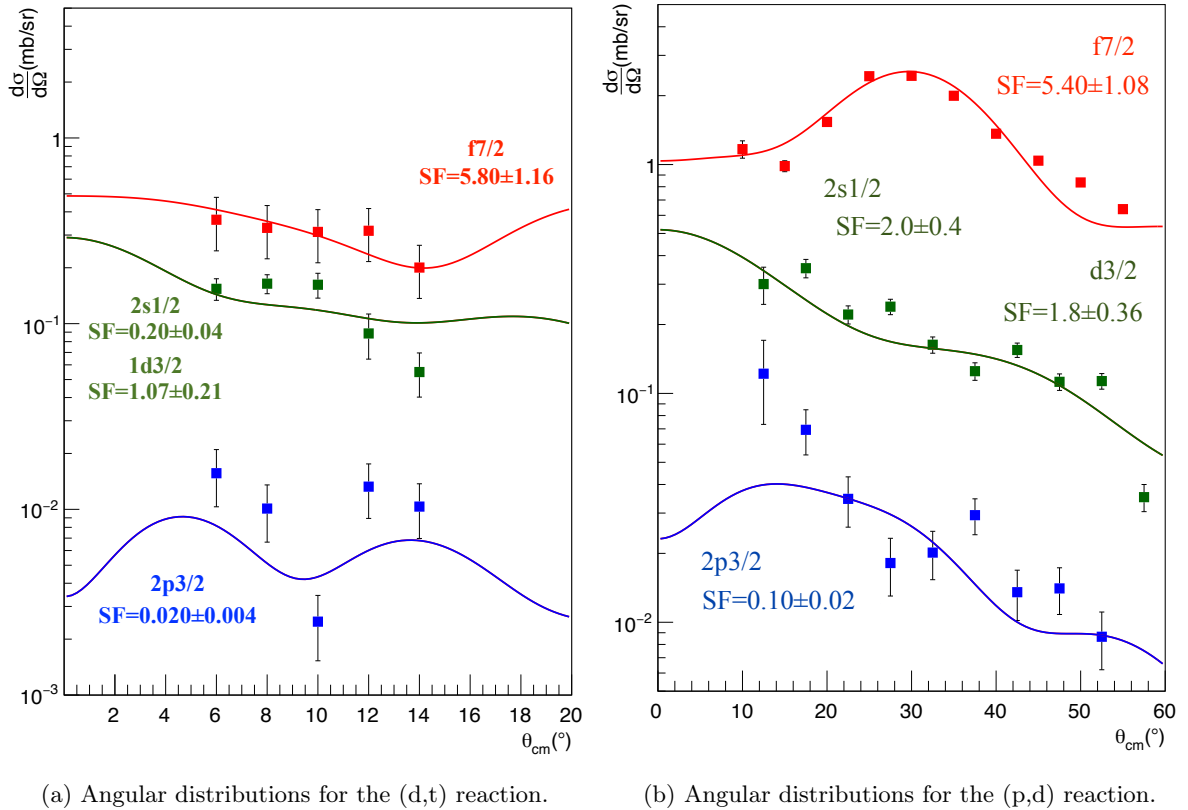


Figure 5.15: Angular distributions for the one nucleon transfers, for the ground state $f_{7/2}$, 2.09 $2p_{3/2}$, 3.185 $2s_{1/2}$ together with the 3.6 $d_{3/2}$

In both cases we compare with DWBA calculation that leads to the extraction of the spectroscopic factors (see chapter 2). The spectroscopic factor is obtained by the ratio between the experimental differential cross section and that calculated DWBA approximation using the FRESKO code [78]. The uncertainties on the spectroscopic factor come mainly from the fact that the model is dependent on the optical models giving a 20% error to be taken into account [79, 80]. Thus, the statistical error becomes negligible.

The angular distribution of the ground state can be well described by a $\ell = 3$ shape. The peak at around 30° degrees is well reproduced in (p,d) measurement, giving confidence in the $7/2^-$ spin assignment. In addition, a large spectroscopic factor is obtained of 5.8 ± 1.16 from the (d,t) and 5.4 ± 1.08 for the (p,d) in the errors of previous studies for the ground state of the (p,d) reaction.

A spectroscopic factor of 0.020 ± 0.004 is obtained for the $3/2^-$ state from the (d,t), while 0.10 ± 0.02 from the (p,d) reaction, while here as well there is compatibility in the slope with the DWBA model especially the reproduction of the deep in the 10° for the (d,t) reaction. This state, having a very small spectroscopic factor with respect to $2j + 1$ (here 4), agrees with the result that the ground state is not 100% $f_{7/2}$, and hints the possibility of 2p-2h excitation towards the $2p_{3/2}$ shell. The population of this state by transfer is not a direct process, since the nucleon is removed from the ground state, so an absolute interpretation for this state is difficult to be made.

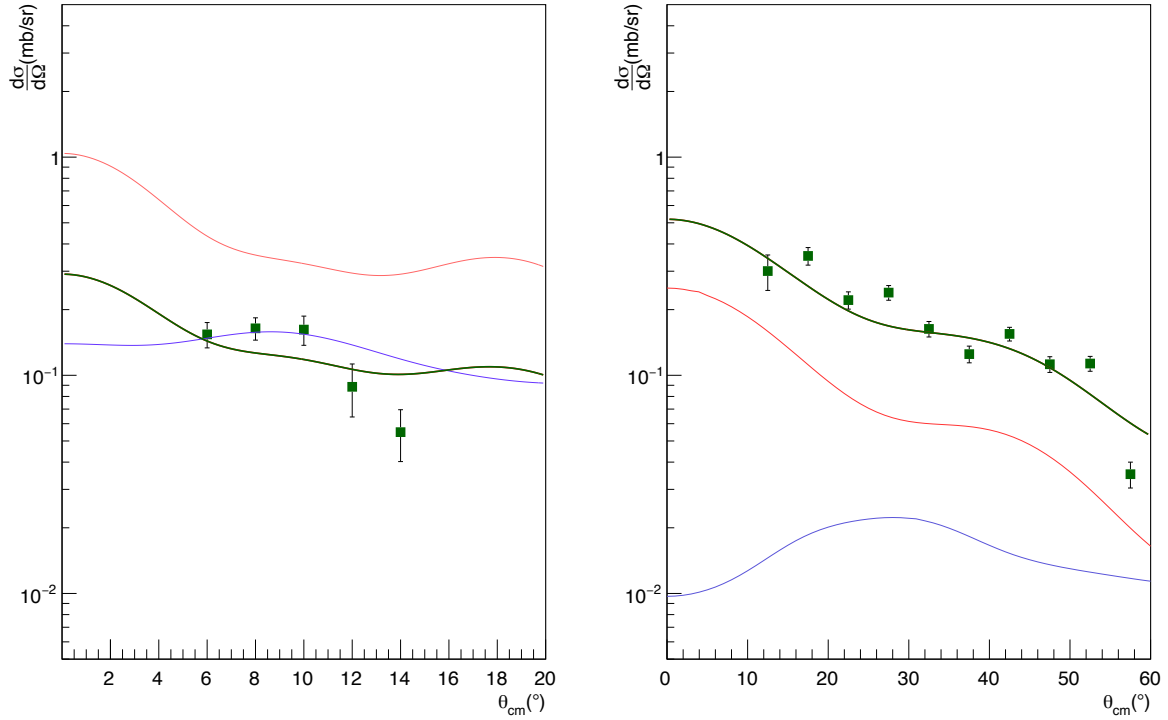
For the two next states we assign them to spins $1/2^+$ and $3/2^+$ respectively from the particle-gamma analysis. They correspond to a neutron hole configuration in the $2s_{1/2}$ and $1d_{3/2}$ orbitals respectively. Since the disentangle of the two states has proven to be a delicate task, we consider that both states contribute in the angular distribution and fit with the DWBA by taking into account both contributions for the best χ^2 as can be seen in Figure 5.16. In that case we find a dominance of the $2s_{1/2}$ state with the maximum spectroscopic factor being 2.0 ± 0.4 , over the $1d_{3/2}$ which contributes with a spectroscopic factor of 1.80 ± 0.36 instead of 4.

5.1.8 Discussion

The spectroscopic factors of the ground state and the three first excited states of ^{55}Ni have been extracted. They can be compared with previous measurements published in [26] as well as the shell model calculations from the same work (see Table 5.7).

State	E_{exp} (MeV)	E (MeV)[26]	E_{SM1}^* (MeV)	$SF_{exp}^{(p,d)}$	$SF_{exp}^{(d,t)}$	SF [26]	SF_{SM1}
$1f_{7/2}$	0.0	0.0	0.0	5.4 ± 1.0	5.8 ± 1.2	6.7 ± 0.7	6.75
$2p_{3/2}$	2.1	2.09	1.89	0.10 ± 0.02	0.020 ± 0.004	0.19 ± 0.03	0.13
$2s_{1/2}$	3.2	3.18	3.039	2.0 ± 0.4	0.20 ± 0.04	1.0 ± 0.2	1.57
$1d_{3/2}$	3.617	(3.752)	3.309	1.8 ± 0.4	1.07 ± 0.21	-	2.88

Table 5.7: Experimental and calculated information on the $f_{7/2}$, $2p_{3/2}$, $2s_{1/2}$ and $d_{3/2}$ states. Where E_{exp} (MeV) and SF_{exp} indicated the results of this work.



(a) DWBA calculation for the contribution of 3.185 MeV and 3.617 MeV in (d,t) reaction.

(b) DWBA calculation for the contribution of 3.185 MeV and 3.617 MeV in (p,d) reaction.

Figure 5.16: The contributions of 3.185 MeV $2s_{1/2}^{-1}$ state together with the 3.617 MeV $1d_{3/2}^{-1}$ state in the DWBA calculation.

g.s.. We obtain large spectroscopic factors for the $1f_{7/2}$ contribution to ground state. It shows a high occupancy of the level with the valence nucleons. The fact that it doesn't get the maximum strength shows that there is strength in the higher energy states. Combined with the information about the 1st excited state, it contains a small admixture of a valence neutron in the $2p_{3/2}$ orbital.

3.6 MeV This state with angular momentum $L=2$ is identified as a neutron hole $d_{3/2}^{-1}$ state contribution. providing additional information comparing to the previous studies. That being from the particle- γ coincidences disentangle but also the wider angular coverage. The measured SF for this state is 1.8 ± 0.4 which only exhaust 50% of the full strength in the single part (Figure 5.16). Thus, it is expected that some of the strength must lie higher in energy. However,

the level scheme is not enough well known and we do not populate these higher states to be able to extract the full strength.

2.1 MeV This first excited particle-state has a very small spectroscopic factor of the order of 0.1 ± 0.01 instead of the 4 that it should have if the state had a full strength. This result is also consistent throughout the fp shell as can be seen by the comparison of the experimental results for intermediate mass nuclei with $Z=20$ to $Z=28$. While the information of each nucleus originates from a different experiment [81, 82, 83], most of the reaction mechanisms used are the same as well a similar energy at which the reaction takes place (Figure 6.1). The SF of these $N=27$ isotones reveal a trend in the $N=27$ isotones for low lying $2p_{3/2}$ spectroscopic factors, suggesting similar core structures in those nuclei.

3.2 MeV For the $1/2^-$ we get the maximum available spectroscopic factor for a $2s_{1/2}$ contribution, meaning that the level is fully occupied. The result is in good agreement with previous studies in the fp shell and more precisely with the ^{48}Ca results [84], studied by ^{48}Ca (p,d) and ^{48}Ca (d,p) reactions. In the latter, the $2s_{1/2}$ state has full strength in most of the $N=27$ isotones.

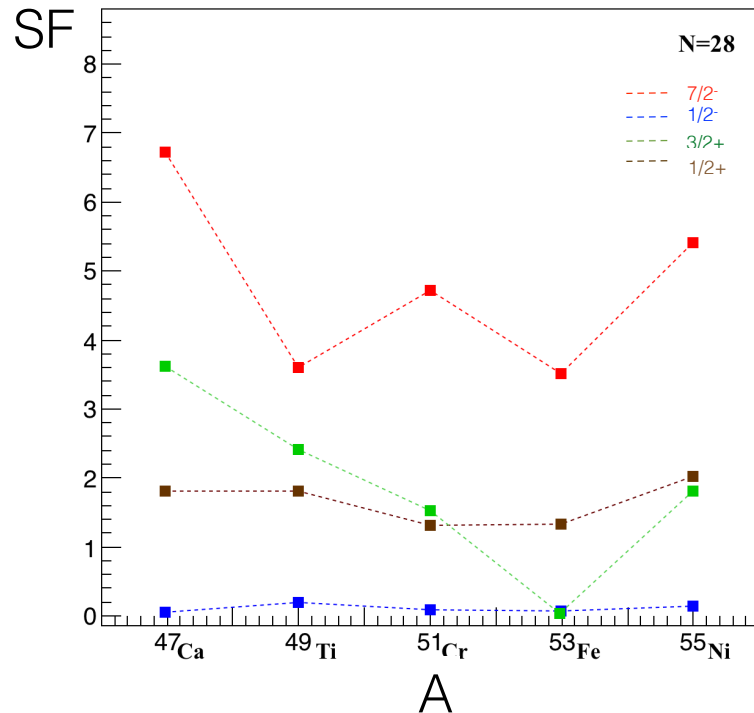


Figure 5.17: Systematics of spectroscopic factors in the fp shell obtained by ENSDF (the error bars are not provided in the literature) as well as measurements for ^{55}Ni obtained by this work.

Evolution of hole-states in N=28

One of the purposes of the experiment was to observe the changes in spectroscopic factors as we move towards the edge of the valley of stability. Figure 5.17 shows the spectroscopic factors for N = 27 isotones in the fp shell. For the nuclei with shell closure at Z= 20 (^{48}Ca) and Z = 28 (^{56}Ni) we observe higher SFs. The lowering of SFs for nuclei between those nuclei can be partly explained by the fragmentation of SF to isobaric analog states with the same spin and parity values.

One can use the information of the neutron occupancy to express the nuclear surface by the Fermi distribution like it has been done for ^{40}Ca and ^{48}Ca . We use the spectroscopic information obtained for the $f_{7/2}$ and $s_{1/2}$ contribution, where the SF are large enough to consider that most of the strength is there. For the information above the Fermi surface we use the data from the (d,p) reaction from the work of Rehm *et al.* [21]. This study carries rather big uncertainties, nevertheless it provides some reference for an estimate of the Fermi surface. In Figure 5.18, the neutron occupation numbers are plotted in the Y-axis (SF/(2J+1)) for hole-states versus the single particle energies in the X-axis following the same idea as it is shown in Uozomi *et al.* [14, 15].

The diffuseness parameter obtained for ^{56}Ni is $\Delta = 2.1 \pm 0.4$. The Fermi surface of ^{56}Ni appears to be rather soft and can be compared with the one of ^{40}Ca .

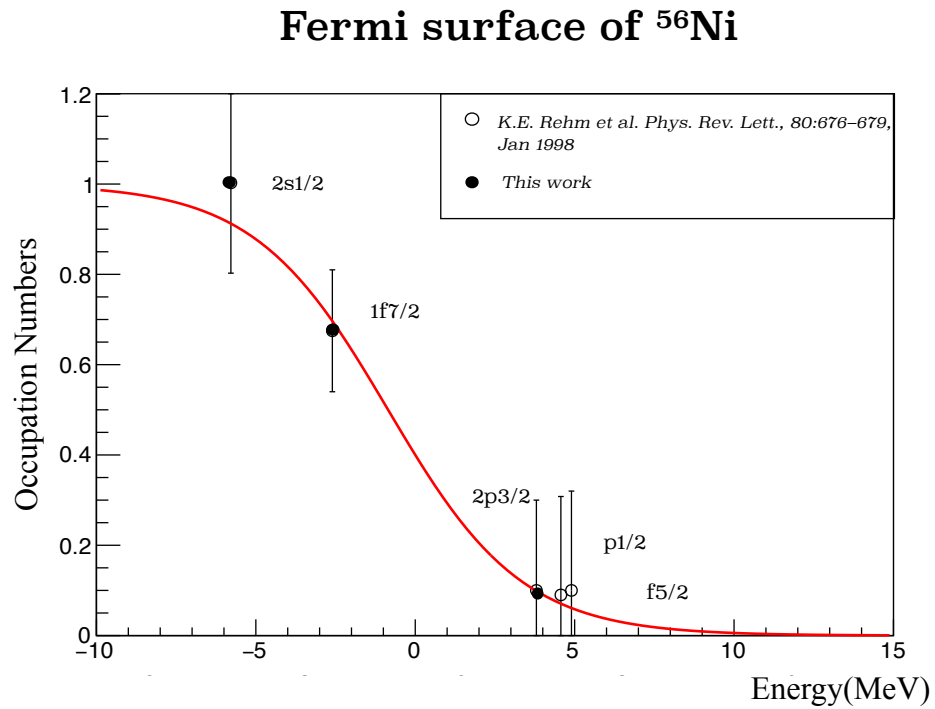


Figure 5.18: Occupation probabilities for neutron shells in ^{56}Ni . The black points are the experimental results, and solid lines the Fermi distribution. Below the fermi surface are the results obtained from this study and above results obtained from the literature. [21] The error bars correspond to the theoretical errors of 20% in the evaluation of the SF.

Part II

Two-nucleon transfer reaction

5.2 The $^{56}\text{Ni}(d,\alpha)^{54}\text{Co}$ reaction

In the case of the two-nucleon transfer the analysis and the data treatment remains the same as for the one nucleon transfer reactions. Consequently, the calibrations as well as the methods of beam alignment and selection still remain the same. The light ejectiles selected in this case are the α particles, which stop in the first layer of the MUST2 detector. The expected cross sections are proven to be low as well as the overall statistics for the two-nucleon transfer reaction, as the break up of the carbon that consist in the target adds background in the final excitation energy spectrum.

5.2.1 Kinematic Lines and Excitation Energy spectra

Kinematics

The reduction of the spectrum of the angle versus the angle in the laboratory system already shows the contamination of the reaction of interest with background coming from the amount of carbon in the 7 mg/cm^2 CD_2 target and can be seen in Figure 5.19. Meaning that the subtraction of the background will play an important role in the analysis of this reaction. The calculated kinematic line that we expected is presented with orange for the first excited state, which is known to be at 0.936 keV. Additionally, we do not accept any event from the CsI crystals since the α -particles of interest do not reach the second layer of MUST2.

Excitation Energy

The spectrum shown in Figure 5.20 corresponds to the excitation energy spectrum and it is being governed by the carbon break up and that is also visible by the fact that there is a high number of counts on the negative energies. Having already validated and calibrated the detectors by the previous analysis we explain the negative counts as background.

5.2.2 Background Subtraction

The subtraction is being done by taking into account the exact portions of carbon atoms in the target as well as the duration of the runs, the flux and the overall cross section.

The formula that gives the the number of counts for a given cross section is the following:

$$N_{counts} = \sigma * \Phi * N_{target} * \epsilon \quad (5.17)$$

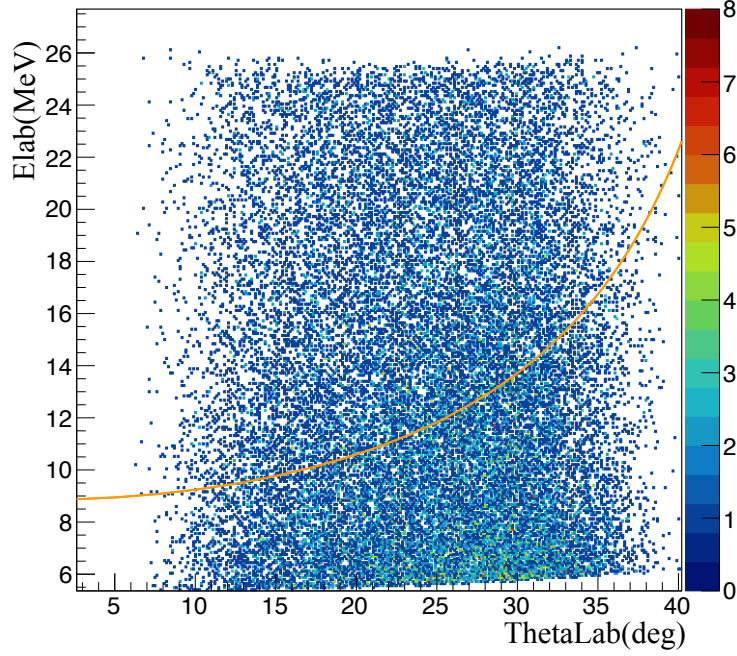


Figure 5.19: Angle-Energy plot for the (d,α) reaction.

Where N_{counts} are the number of events measured for a reaction coming from this target, σ corresponds to the cross section of the reaction, Φ is the flux of the beam, N_{target} is the number of atoms in the target/cm² and ϵ is the efficiency of the detection.

For the N_{target} :

$$N_{target} = n * N_A, \quad (5.18)$$

where n the mol of carbon in the target and N_A the Avogadro constant. And for n :

$$n = \frac{m}{M_r}, \quad (5.19)$$

where m the mass in gr and M_r the molar mass in $\frac{gr}{mol}$. Thus, for each target $N_{^{12}C} = 1.4 \times 10^{20}$ atoms/cm² and $N_{CD_2} = 2.6 \times 10^{20}$ atoms/cm².

The $N_{counts}^{CD_2}$ for the number of carbon in the CD_2 and $N_{counts}^{^{12}C}$ for the ^{12}C target is calculated

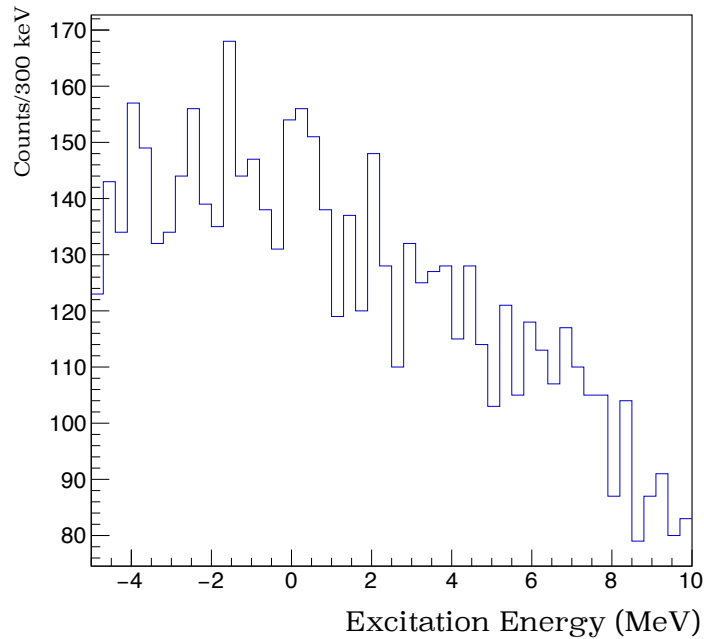


Figure 5.20: Excitation energy spectrum of the (d,α) reaction on a CD_2 target.

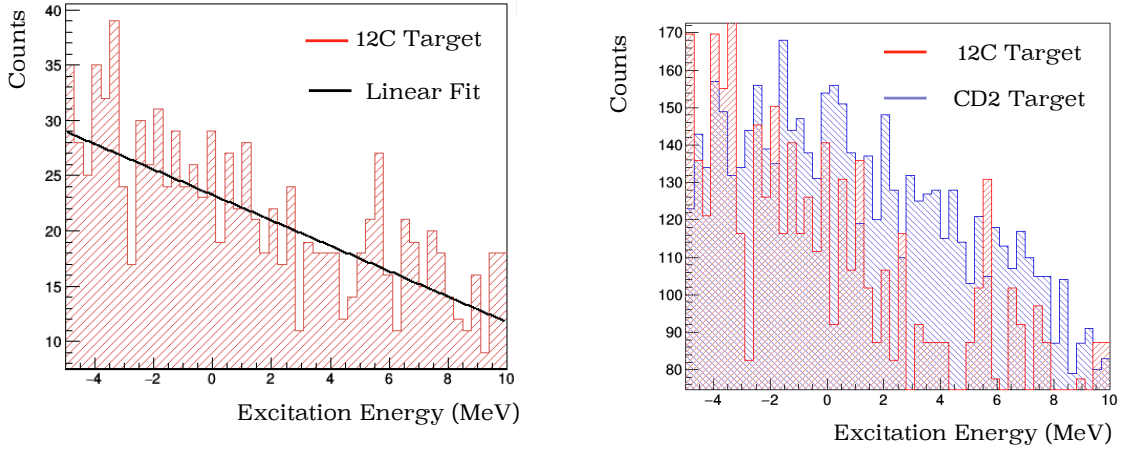
as:

$$\frac{N_{counts}^{CD_2}}{N_{counts}^{^{12}\text{C}}} \approx 8 \quad (5.20)$$

Thus, we find that there is 8 times the carbon of ^{12}C in the 7 mg/cm^2 of CD_2 . There are two different methods used for the subtraction of the background.

- (i) The first method requires the parametrisation of the shape of the carbon background or else, a fit. We can choose a first order polynomial function to reproduce in general the shape of the carbon, as it can be seen in Figure 5.21a. Afterwards, we can use the same shape for fitting the excitation energy spectrum and remove it.
- (ii) In the second case, we know from previous transfer reaction studies and since the calibrations and positions have been already validated by the one-nucleon transfer analysis, that the negative part of the excitation energy spectrum must correspond in noise or else events coming from the background. Thus, by taking the integral in the negative part (for instance -2 to -4 MeV) we are able to adjust the two spectra (see Figure 5.21b).

The methods give approximately the same result within the statistical errors. The spectra resulting from those subtractions can be seen in Figure 5.22.



(a) The excitation energy spectra for the ^{12}C target fitted with the first order polynomial. (b) Excitation energy spectrum of the (d,α) reaction on a CD_2 target and on ^{12}C target in red.

Figure 5.21: Excitation energy spectrum of the (d,α) reaction on the C target with the first order fitting on the left and Excitation energy spectrum on a CD_2 target and on carbon target with red.

Comments on the excitation energy spectrum

On the level scheme of ^{54}Co from the NNDC [52] there is an isomeric state observed with higher spin and isospin $T=0$, like the first excited state of interest Figure 2.15. By transfer reaction in medium energies (of 30 MeV per nucleon) a priori we shouldn't be able to populate this isomeric state. For that reason it was not included for the analysis of the $(p,^3\text{He})$ reaction. If the reactions populate this isomeric state it should be visible in the excitation energy spectrum of the (d,α) reaction since it is selective in $T=0$ states only. One thing we can conclude by looking at the energy spectrum is that there is no state populated around zero and at 0.192 MeV where the isomeric state is expected. The absence of the state of interest allow us only to extract an upper limit on the cross section.

5.2.3 Upper Limit Cross Section

To calculate the total cross section we follow the same equation and steps as for the angular distribution in the previous section 5.1 in subsection 5.1.5 with the difference that in this case we consider the full angular range, since the kinematic lines cover all the angles. The solid angle

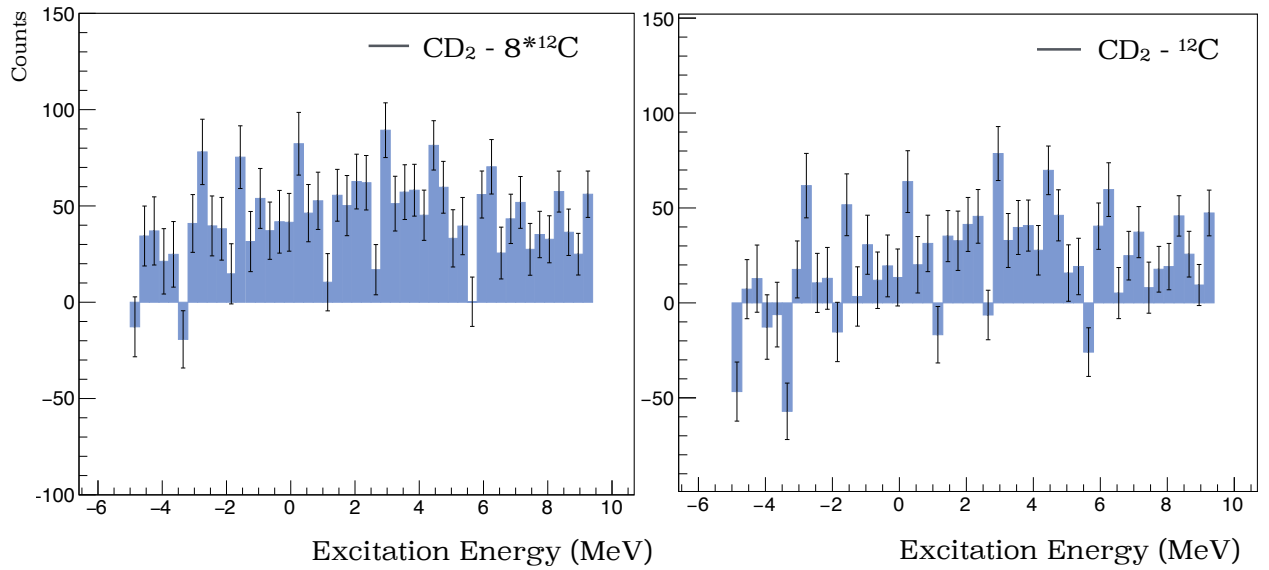


Figure 5.22: Excitation energy spectrum of the (d,α) reaction on a CD_2 target after subtraction of the carbon contamination in the target. Left: Excitation energy spectrum of the (d,α) reaction on a CD_2 target with the C subtraction with fit method. Right: Excitation energy spectrum of the (d,α) reaction on a CD_2 target with the C subtraction with integral method.

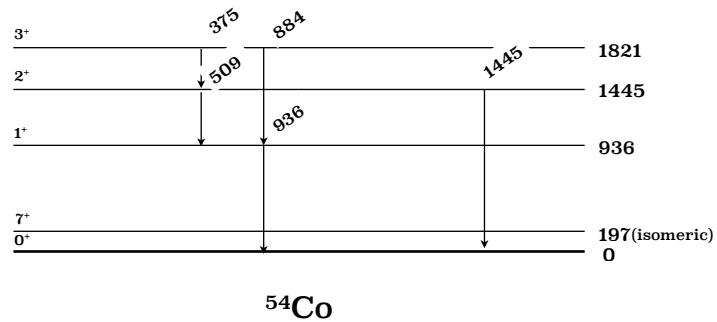


Figure 5.23: Level scheme of ^{54}Co based on NNDC [52] information.

that the detector MUST2 covers has been calculate and taken into account as follows:

$$\Omega = 4 * \arcsin(\sin a \sin b), \quad (5.21)$$

With a and b described below:

$$a = \arctan\left(\frac{w}{2d}\right) \qquad b = \arctan\left(\frac{h}{2d}\right) \qquad (5.22)$$

The distance to the detector is noted as d in the relation 5.22 and is equal to 150mm, the detectors active height is noted with $h=200$ mm and the detector active width is noted with $w=250$ mm if we sum all four MUST2 telescopes. Finally, the solid angle of the detector is equal with $\Omega = 1,4sr$. The upper limit cross section for the first excited state of ^{54}Co is then $\sigma_{tot}=3\mu b$. It is found to be one order of magnitude smaller than what we find with the $(p,^3\text{He})$ reaction, which was found to be $\sigma(1^+) = 11.5 \mu b$ for the first excited state [50].

5.2.4 Discussion

In the case of a direct transfer mechanism of a np pair, the cross section of the transfer of a pair is related to the number of np pairs present in the nucleus. The transfer probes the collectivity of the state, distinguishing between rotational and vibrational behavior of pairing. Already from the $(p,^3\text{He})$ reaction the cross section corresponding to the strength of T=0 channel is lower than what was expected. With the $(p,^3\text{He})$ reaction we measured the ratio of the cross section of the transfer to the ground state over the cross section of the first excited state of ^{54}Co . In that way, the relative strength was obtained between the isovector and isoscalar np pairing and it is equal to $\frac{\sigma(0^+)}{\sigma(1^+)} = 6.3_{-0.8}^{+2.8}$. The lower limit is obtained by considering the maximum population of the T=0 and the minimum of the T=1. With the (d,α) we do not expect to populate the ground state of ^{54}Co . Not populating the first excited state is an indication that in this case the reaction has lower cross section than the one expected. The non-existence of the expected isomeric state can confirm the ratio extracted from the $(p,^3\text{He})$. In addition, the very low cross section extracted for the $\sigma(1^+) = 11.5\mu b$ is in relatively good agreement with the information that we got from the first excited state with the $(p,^3\text{He})$. With the additional information, it is clear now that in the fp -shell the strength is being dominated by the spin-orbit term for being able to investigate further the np- pairing interactions one should look in the larger shells like for example the $g_{9/2}$.

6

Conclusions

In this twofold study of the ^{56}Ni nucleus, we investigated the robustness of the $N=28$ shell closure next to stability, as well as the np pairing in the $N=Z$, fp shell closure. The method used for both studies is the direct reactions in inverse kinematics. The experiment was performed in 2014 in GANIL, France by using a secondary beam of ^{56}Ni produced by fragmentation and purification. The complete set-up consisted of a variety of detectors providing information for both particle and γ detection.

6.1 One-nucleon transfer

With the one-nucleon transfer reaction we obtained the spectroscopic factors for the ground state and the three excited states corresponding to the removal of a neutron in the $1f_{7/2}$, $2p_{3/2}$, $2s_{1/2}$ and $1d_{3/2}$ via the (d,t) and (p,d) reactions. The combined information from particle- γ coincidences, allowed us to enrich the level scheme of ^{55}Ni and disentangle the different energy levels. We investigated the evolution of the $N=28$ shell gap by comparing spectroscopic factors obtained by previous measurements all along the fp shell for the $N=27$ isotones with $Z=20$ until $Z=28$. The common behavior for the magic ^{47}Ca and ^{55}Ni nuclei unravels the strength of the

N=28 shell closure throughout the nuclear chart. The SF obtained for the ground state and the 3.185 MeV levels of ^{55}Ni carry all the strength of the corresponding single particle states, $1f_{7/2}$ and $2s_{1/2}$, allowing us to get the information below the Fermi surface of ^{56}Ni . By taking into account the previous measurements for the ^{57}Ni nucleus by Rhem *et al.* [21] we drew the whole Fermi surface which appears to be rather soft, with a high diffuseness parameter ($\Delta=2.4$ MeV) comparable with the one obtained for ^{40}Ca .

Perspectives

New measurements above the Fermi surface of ^{56}Ni are of great importance. Firstly, the already existing ones come with a rough estimated uncertainty of 50% on the SF and there is room for improvements.

Secondly, there are several models that predict an intrusion of the $2p_{1/2}$ and the $2p_{3/2}$ valence orbits of ^{56}Ni . Although ^{57}Ni has a large density of excited states from 2 to 4 MeV a use of good γ tracking device can solve the disentanglement with the use of particle- γ coincidences to identify the populated states, as it has been done in this work. Even though with this experiment we had in hand all the complimentary reactions the identification at the backward angles was very difficult to be done since it required the use of the single layered TIARA detector and we couldn't rely on the statistics. Thus, a new measurement with an upgraded experimental set-up can provide the missing information.

Lastly, there is a great theoretical interest for the *ab-initio* studies of the intermediate size and mass nuclei. The comparison of the calculations that are included in the Sanetullaev *et al.* paper [26] and the results of this work show a very good agreement in the predictions of the SF even better than the one of the shell model calculations. However, there is a big discrepancy for the energy levels predicted by these studies. The additional experimental information about the nuclei in the fp shell can provide aid for the development of the *ab-initio* calculations.

State	E_{exp} (MeV)	E_{SM1}^* (MeV)	E_{SCGF}^*	$SF_{exp}^{(p,d)}$	$SF_{exp}^{(d,t)}$	SF_{SM1}	SF_{SCGF}
$f_{7/2}$	0.0	0.0	0.0	5.4 ± 1.0	5.8 ± 1.2	6.75	5.78
$2p_{3/2}$	2.1	1.89	4.34	0.10 ± 0.02	0.020 ± 0.004	0.13	0.06
$2s_{1/2}$	3.2	3.039	11.48	2.0 ± 0.4	0.20 ± 0.04	1.57	1.10
$d_{3/2}$	3.6	3.309	12.47	1.8 ± 0.4	1.07 ± 0.21	2.88	2.16

Table 6.1: Experimental and calculated information on the $f_{7/2}$, $2p_{3/2}$, $2s_{1/2}$ and $d_{3/2}$ states. Where E_{exp} (MeV) and SF_{exp} indicated the results of this work, SM1 NuShell shell model calculations and SXGF *ab-initio* calculations.

The use of the combined MUGAST and AGATA set-up in addition with a spectrometer for identifying the residual nucleus will provide great resolving power and efficiency to the measurement. MUGAST is composed of 5 trapezoidal DSSSDs and 1 annular detector at backward angles, 2 squared DSSSDs at 90° and 4 MUST2 telescopes at the forward angles. The lower energy of the protons with the use of SPIRAL at the background angles will not allow them to punch through the annular detector, making their identification possible. The energy resolution of AGATA of about 5 keV after Doppler correction will enable the disentanglement of the different states and the ground state contribution will be deducted by deconvolution.

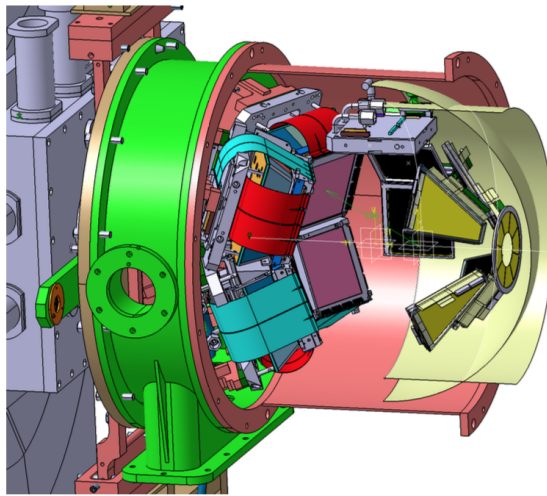


Figure 6.1: MUGAST set-up with the beam going from the right to the left and the 4 MUST2 detectors in the forward direction, the 2 square DSSSD at 90 degree and the 4 to 5 trapezoidal ones in the backward direction. VAMOS is on the left in this picture, E.Rindel

The above experiment has been already proposed by F.Flavigny and our group and will take place in the near future.

6.2 Two-nucleon transfer

The two-nucleon transfer reaction has been treated to aid understanding of the $T=0$ isoscalar pairing in the fp shell. The selectivity of the (d,α) reaction would enable the identification of the first excited state that was a challenging task with the previous measurement of the $(p,^3\text{He})$ reaction [50]. The excitation energy spectrum obtained after the α -particle selection was governed by background originating by the break-up of the carbon in the CD_2 target. After the subtraction of the background we were able to perform an estimate on the upper limit of

the cross-section for the first excited state. The two-nucleon transfer was expected to have a low cross-section and already the previous measurement of first excited state with the $(p, {}^3\text{He})$ reaction gave a cross-section of $\sigma(1^+) = 11.5 \mu\text{b}$. In this case the upper-limit was found to be $\sigma(1^+) = 3 \mu\text{b}$. Even if the $T=0$ pairing is expected to be strong in the $N=Z$ nuclei the existence of the spin-orbit term in fp shell appears to hinder the pairing correlations.

Perspectives

The interest of the np pairing investigation remains high and thus the quest for solutions that will provide a clearer image on the matter is necessary. In order to suppress the background from contaminants, mostly emerging from the carbon break up in the targets, a new generation of active targets/time-projection chamber has been developed and recently started to be used. This class of instruments, initially developed for high-energy physics, has found various applications in medium- and low-energy nuclear physics. In these targets, the reaction between the beam and the gas takes place in the active volume, and at the same time the gas volume is used as a detector: the reaction products ionize the gas, releasing electrons that drift to a highly pixelated pad plane. One can find detectors like this in GANIL and the ACTAR detector [85] or in MSU and the AT-TPC [86]. Proposals of experimental studies of np pairing with the use of active targets have been already be done like for instance the proposal of A.O. Macchiavelli *et al.* for the studies of np pairing with the ${}^{52}\text{Fe}({}^3\text{He}, p)$ reaction in MSU and the AT-TPC. Another more recent

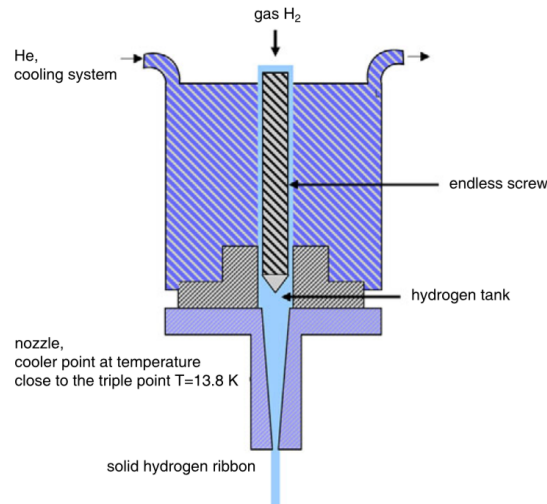


Figure 6.2: Diagram of the device for the extrusion of hydrogen ice [87].

development is the windowless thin solid-hydrogen target called CHyMENE (see Figure 6.2).

The thickness is within the range 50-200 μm , in order to be used as a target for reactions in inverse kinematics with radioactive beams at low incident energies (2–15 MeV/nucleon) [87]. For the moment only the use with ^1H gas is being investigated but in the near future it will be extended also for ^2H and then the (d,α) reaction can be available.

In addition we need a very efficient detection system because the cross-section of the two-nucleon transfers are very low. By coupling charged-particle detector with high resolution γ -detectors we can use the information from the γ -rays to infer the relative ratio of the states of excited states. This method enables to constraint the fit of the excitation energy spectrum, as it has been done for the $(p,^3\text{He})$ reaction. Although, relying a bit more on the γ -detection by gating on the transitions of interest, might allow us to extract the angular distribution from the associated state from the particle measurement.

The ultimate goal of these studies will be to be able to reach the $g_{9/2}$ shell and the heaviest known $N=Z$ nuclei and perform transfer reactions.

Appendices

A

Target Position

The Figure [4.12](#) corresponds to the runs with the CD_2 target. One can notice that on the left side the frame of the target appears tilted. Below we present some further details on how this difficulty was solved.

That corresponds to some movement of the target during the experiment that proved to be a challenge for obtaining the results. This unfortunate fall can be described as an additional distance on the z axis, effecting the energy losses for the final result. To solve the movement of the target and with help of the kinematic lines we fixed the position of the target further on the beam axis by approximately 1 cm. In Figure [A.1](#) we can see the gradual shift of the target position according to the kinematic lines.

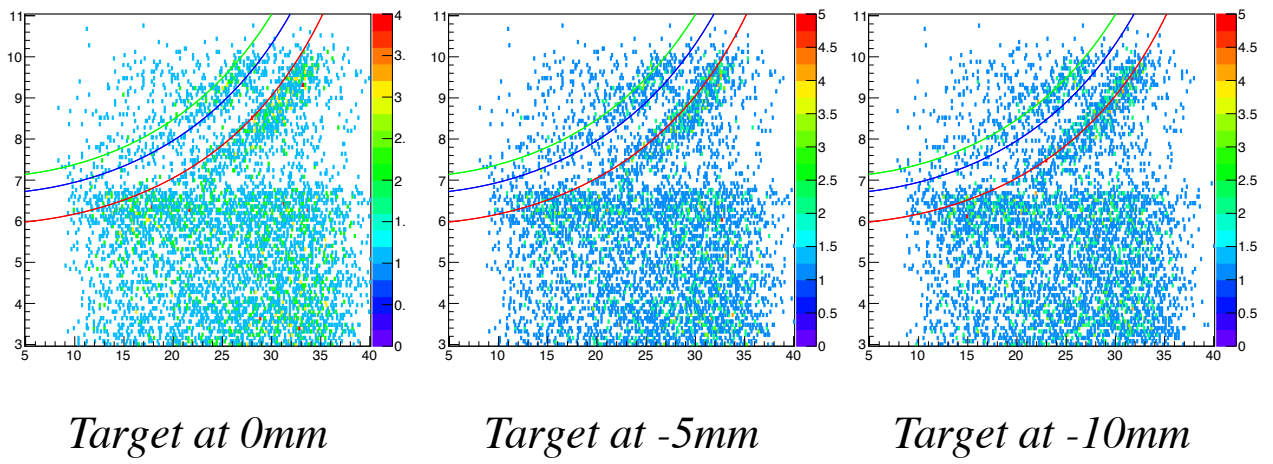


Figure A.1: the gradual shift of the target position according to the kinematic lines. CATS and beam position have been already validated by the mask

B

Fresco Input file example

The following lines describe the input file used for the ground state of the (d,t) reaction for the FRESCO code [78].

```
56Ni(d,t)55Ni at 60MeV;
NAMELIST
&FRESCO hcm=0.05 rmatch=30.00 rintp=0.20 hnl=0.1 rnl=20.00 centre=0.0
jtmin=0.0 jtmax=30 absend=-0.01 thmin=0.00 thmax=180.00 thinc=1.0
iter=1 nnu=36 chans=1 xstabl=1 smats=1
elab=60.00 /

&PARTITION namep= d1 massp=2.0141 zp=1 namet= 56Ni masst=56. zt=28. nex=1 /
&STATES jp=1 bandp=1 ep=0.0 cpot=1 jt=0.0 bandt=1 et=0.0000 /
&PARTITION namep= t2 massp=3. zp=1 namet=55Ni masst=55. zt=28 qval=-10.3858
nex=1 /
&STATES jp=0.5 bandp=1 ep=0.0 cpot=2 jt=3.5 bandt=-1 et=0.0000 /
&partition /
```

Appendix B. Fresco Input file example

```
&POT kp=1 ap=2.0141 at=56.0 rc=1.30 / #adiabatic deuteron optical
&POT kp=1 type=1 p1= 90.838 p2=1.191 p3=0.690 p4=5.495 p5=1.220 p6=0.630 /
&POT kp=1 type=2 p1=0.0 p2=0.0 p3=0.0 p4=11.467 p5=1.220 p6=0.630 /
&POT kp=1 type=3 p1=11.800 p2=1.026 p3=0.630 p4=0. p5=0. p6=0. /

&POT kp=2 ap=3. at=55. rc=1.271 / #triton optical
&POT kp=2 type=1 p1=114.466 p2=1.174 p3=0.84 p4=3.155 p5=1.271 p6=0.84 /
&POT kp=2 type=2 p1=0.0 p2=0.0 p3=0.0 p4=17.2950 p5=1.271 p6=0.84 /

&POT kp=3 at=56.0 rc=1.250 / #neutron bound state potential
&POT kp=3 type=1 p1=50.00 p2=1.250 p3=0.650 /
&POT kp=3 type=3 p1=6.50 p2=1.250 p3=0.650 /

&POT kp=4 type=1 p1=100.000 p2=0.95 p3=0.650 p4=0.0 p5=0.0 p6=0.0 p7=1.0 / #t=
n+ d gs

&POT kp=5 ap=2.0141 at=55.0 rc=1.30 / #adiabatic deuteron optical
&POT kp=5 type=1 p1= 90.838 p2=1.191 p3=0.690 p4=5.495 p5=1.220 p6=0.630 /
&POT kp=5 type=2 p1=0.0 p2=0.0 p3=0.0 p4=11.467 p5=1.220 p6=0.630 /
&POT kp=5 type=3 p1=5.900 p2=1.026 p3=0.630 p4=0. p5=0. p6=0. /

&pot /

&Overlap kn1=1 ic1=1 ic2=2 in=1 kind=0 nn=1 l=0 sn=0.5 j=0.500 kbpot=4 be=6.257
isc=1 ipc=0 /

&Overlap kn1=2 ic1=2 ic2=1 in=2 kind=0 nn=1 l=3 sn=0.5 j=3.5 kbpot=3 be=16.643
isc=1 ipc=0 /

&overlap /

&Coupling icto=2 icfrom=1 kind=7 ip1=1 ip2=-1 ip3=5 /
&CFP in=1 ib=1 ia=1 kn=1 a=1.00 /
```

&CFP in=-2 ib=1 ia=1 kn=2 a=1.00 /
&cfp /
&coupling /

C

Résumé en français

C.1 Motivation Physique

Historiquement, les études de structure nucléaire ont émergé par l'utilisation de réactions directes en cinématique directe. Les réactions ont été effectuées en utilisant des faisceaux d'ions légers sur la cible constituée des noyaux d'intérêt. Pour pouvoir étudier des noyaux de courte durée de vie loin de la stabilité, il faut inverser le problème. Cela a conduit à l'utilisation de la cinématique inverse où la cible légère sert de sonde et le faisceau est constitué par les noyaux instables intéressés à courte durée de vie. La cinématique inverse a été utilisée pour révéler les propriétés des noyaux radioactifs dans les régions exotiques de la carte nucléaire, telles que les limites d'existence, et a permis d'étudier l'évolution des couches loin de la stabilité [1]. Dans ce travail sur l'utilisation de réactions de transfert à un et deux nucléons, nous étudions deux aspects physiques différents. Le noyau doublement magique ^{56}Ni , avec $N = Z = 28$, est un noyau clé pour étudier la fermeture de la couche $N = 28$ ainsi que les corrélations d'appariement neutron-proton (np).

C.1.1 Réaction de transfert d'un nucléon

La chaîne isotopique du Ni fournit une variété de noyaux doublement magiques. Depuis le ^{48}Ni se trouvant dans la limite de la stabilité des particules et constituant le noyau miroir du ^{48}Ca , noyau auto-conjugué de ^{56}Ni et jusqu'au ^{78}Ni se trouvant à la drip line neutrons. L'évolution des nombres magiques $N = Z = 28$ a été d'un grand intérêt ces dernières années. Avec de nouveaux résultats expérimentaux sur la limite d'existence neutron, le nombre magique $Z = 28$ révèle une robustesse qui fait du ^{78}Ni le noyau doublement magique le plus riche en neutrons [3]. Bien que, lorsque l'on se déplace vers les bords de la carte nucléaire, la fermeture de la couche $N = 28$ devient discutable et une disparition des états de particule individuelle devrait avoir lieu.

Les réactions de transfert à un nucléon telles que (d,p), (p,d) et (d,t) sont l'un des moyens les plus directs de tester la configuration de particule individuelle du noyau magique de ^{56}Ni . La mesure de l'occupation des orbites neutrons fournira des informations sur la robustesse du nombre magique $N = 28$ à travers l'étude des isotones $N = 27$ et $N = 29$. L'évolution des couches avec les isotones $N = 27$ autour du ^{48}Ca est décrite en détail dans l'article de synthèse de O.Sorlin et M-G. Porquet [12]. Il convient de noter en particulier qu'environ 90% de la configuration de l'état fondamental du noyau ^{47}Ca sphérique correspond à un trou neutron dans la couche $f_{7/2}$ (configuration 0p1h) et à un noyau fermé en proton (configuration 0p0h). Ils ont présenté un développement possible de la collectivité dans les isotones $N = 27$, en comparant les caractéristiques de leurs premiers états. Le premier état excité avec $J_\pi = 3/2^-$ devrait impliquer la promotion d'un neutron dans la couche supérieure $p_{3/2}$ avec deux trous neutron couplés dans la couche $f_{7/2}$ (1p2h). C'est en accord avec les calculs théoriques montrant que la force réside principalement dans l'excitation pure d'un neutron [11, 10]. Cet état, avec une configuration de proton fermée, se trouverait bien au-dessus de l'état fondamental de tous les isotones $N = 27$, sauf si l'écart de couche $N = 28$ est réduit et est dominé par les corrélations. Comme le montre la même étude, c'est le cas des isotones $N = 27$ dans la couche *sd*. Expérimentalement, la mesure des sections efficaces pour le transfert d'un nucléon doit être comparée à des calculs théoriques. Le rapport entre les deux valeurs donne le facteur spectroscopique pour l'état d'intérêt de la particule individuelle qui peut ensuite être utilisé pour déduire les nombres d'occupation pour les neutrons.

C.1.2 Réaction de transfert de deux nucléons

Une partie importante de l'interaction nucléon-nucléon (NN) est la corrélation à courte portée. Inspiré par la science des matériaux et les paires d'électrons de Cooper, l'appariement entre les nucléons devient une partie importante de l'interaction NN, tandis que de plus en plus d'expériences

prouvent son existence [4]. Il existe deux types d'appariement, le premier dans le canal isovecteur et l'autre dans le canal isoscalaire. Le principe de Pauli joue également un rôle important dans la détermination du moment cinétique total (J) et du spin (S) du couple. Suivant ce principe, les paires np ont des états avec soit le moment angulaire total $J = 0$ et l'isospin $T = 1$ (mode isovecteur), soit avec $J = 1$ et $T = 0$ (mode isoscalaire). L'appariement $T = 1$ devrait être similaire à l'appariement $T = 1$ pour les paires nn et pp en raison de l'indépendance de charge. Les caractéristiques de l'appariement $T = 0$ sont en revanche largement inconnues.

L'étude expérimentale de l'appariement np est une tâche difficile qui repose sur la pertinence de l'observable physique. L'appariement de nn et pp a été mis en évidence par des études de réactions de transfert à deux nucléons dans les isotopes Pb et Sn . La section efficace de transfert de deux nucléons entre l'état fondamental des noyaux pairs et les 1er états excités révèle un comportement vibratoire dans l'isotope du Pb (isotopes à couche fermée) où la section efficace est proportionnelle au nombre de paires. Alors que pour les isotopes Sn (noyaux à couche ouverte), la section efficace est largement amplifiée d'un facteur d'environ 25, montrant un comportement rotationnel. Par extension, les mêmes effets sont attendus dans la réaction de transfert de paires np si l'appariement np se développe dans les noyaux $N = Z$. La réaction de transfert que nous étudions révélera des informations sur la force d'appariement $T = 0$ dans la couche fp . En effet elle est particulièrement adaptée à cette étude car seule la transition $\Delta T = 0$ (transfert d'un deutéron) est autorisée.

C.2 Dispositif expérimental

L'expérience a été réalisée en 2014 au Grand Accélérateur National d'Ions Lourds (GANIL), Caen. Le faisceau radioactif de ^{56}Ni à 30 MeV/u a été produit par fragmentation d'un faisceau primaire de ^{58}Ni et purifié au moyen du séparateur LISE. Les mesures ont été effectuées en cinématique inverse sur les cibles CH_2 et CD_2 . Deux chambres proportionnelles multi-fils (CATS) ont été placées en amont de la cible de la réaction et ont fourni, événement par événement, la position et l'angle des particules du faisceau entrant. L'expérience comprenait une couverture proche de 4π pour les éjectiles légers. Les deux composants du détecteur silicium TIARA, Barrel et Hyball, ont été placés aux angles centraux et arrières. Quatre télescopes MUST2 couvraient les angles avant. Tiara et MUST2 ont fourni les paramètres nécessaires à l'extraction de l'énergie d'excitation et à la distribution angulaire. Les lignes cinématiques des particules légères qui reculent sont représentées à la Figure C.2 dans le plan des énergies et des angles pour les réactions considérées. La couverture angulaire de la détection de particules est également

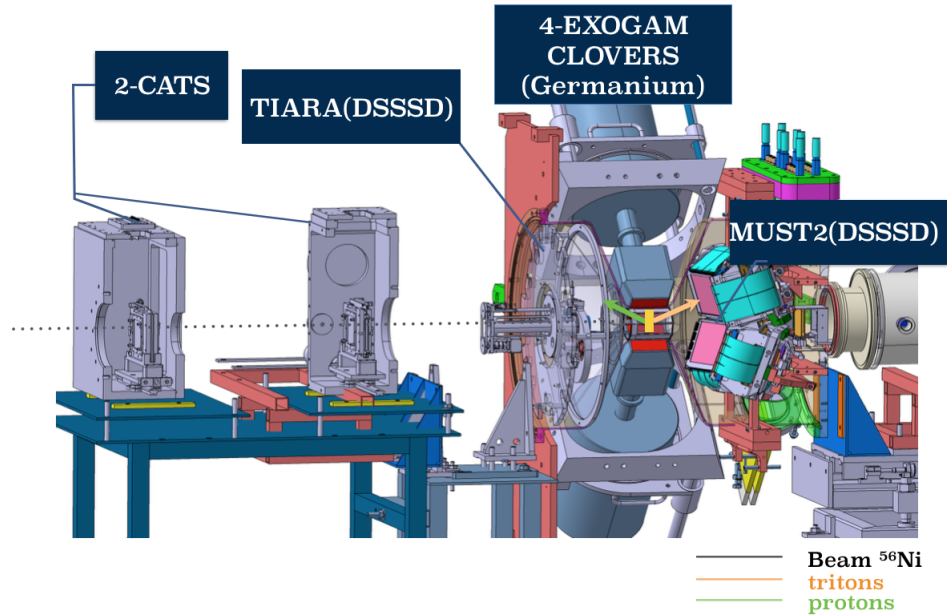


Figure C.1: Le dispositif expérimental constitué de: CATS, TIARA, 4 EXOGAM clover autour de la cible, MUST2 dans les angles avant et CHARISSA. L'ordre des détecteurs est lié à l'arrivée du faisceau de gauche à droite. Illustration de E.Rindel.

indiquée. 4 clovers Germanium provenant d'EXOGRAM ont été rajoutés à 90 deg pour pouvoir mesurer les coïncidences particule-gamma.

C.3 Résultats et conclusions

Dans cette étude, du noyau doublement magique de ^{56}Ni , nous avons étudié la robustesse de la fermeture de couche $N = 28$, ainsi que l'appariement np à la fermeture de couche fp.

C.3.1 Réaction de transfert d'un nucléon

Avec la réaction de transfert d'un nucléon, nous avons obtenu les facteurs spectroscopiques pour l'état fondamental et les trois états excités correspondant à des configurations de particule individuelle $1f_{7/2}$, $2p_{3/2}$, $2s_{1/2}$ et $1d_{3/2}$ via les réactions (d,t) et (p,d). Les informations combinées des coïncidences particule- γ nous ont permis d'enrichir le schéma de niveaux de ^{55}Ni et de démêler les différents niveaux d'énergie. Nous avons étudié l'évolution de la fermeture de couche $N = 28$ en comparant les facteurs spectroscopiques obtenus par des mesures antérieures tout au long de

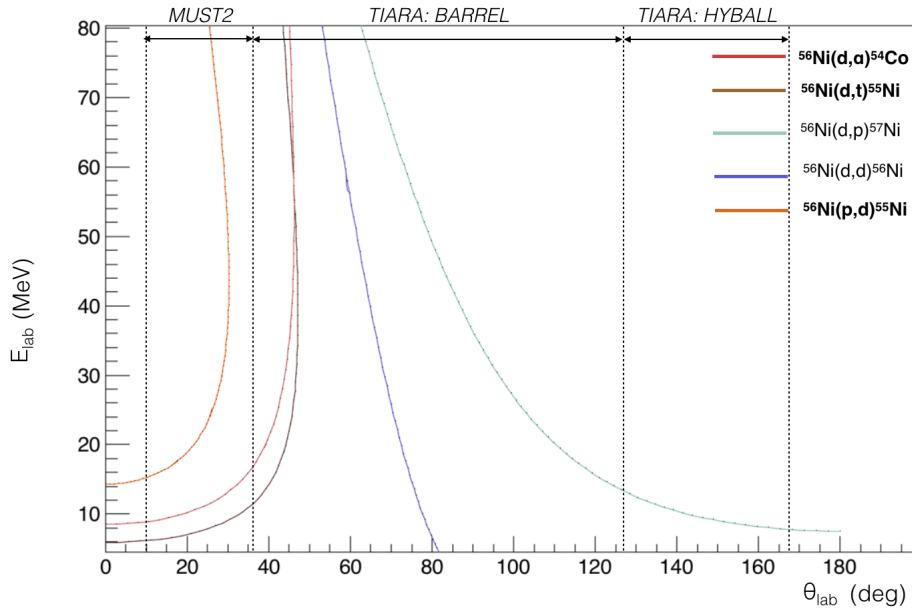


Figure C.2: Les lignes cinématiques des réactions d'intérêt et la couverture du détecteur

la couche fp pour les isotones $N = 27$ avec $Z = 20$ jusqu'à $Z = 28$. Le comportement des noyaux semi magiques de ^{47}Ca et ^{55}Ni révèle la robustesse de la fermeture de la couche $N = 28$ sur l'ensemble de la carte nucléaire. Le facteur spectroscopique obtenu pour l'état fondamental et le niveau à 3,805 MeV du ^{55}Ni correspond à des configurations pure $1f_{7/2}$ et $2s_{1/2}$, respectivement ce qui nous permet d'obtenir les informations sur la surface de Fermi du ^{56}Ni . En prenant en compte les mesures précédentes pour le noyau ^{57}Ni de Rhem et al. [21], nous avons dessiné la surface entière de Fermi qui semble avoir une pente plutôt douce, avec un paramètre de diffusivité élevé ($= 2,4$ MeV) comparable à celui obtenu pour le ^{40}Ca .

C.3.2 Réaction de transfert de deux nucléons

La réaction de transfert de deux nucléons a été traitée pour améliorer la compréhension de l'appariement isoscalaire $T = 0$ dans la couche fp. La sélectivité de la réaction (d, α) permet d'identifier le premier état excité qui posait problème avec la mesure précédente de la réaction $^{56}\text{Ni}(p, ^3\text{He})$ [50]. Le spectre d'énergie d'excitation obtenu après la sélection des particules est dominé par un bruit de fond provenant de l'émission de particules alpha par le carbone de la cible CD_2 . Après la soustraction du fond, nous avons pu effectuer une estimation de la limite supérieure de la section efficace pour le premier état excité. La section efficace du transfert à deux

nucléons devait être basse et déjà la mesure précédente du premier état excité avec la réaction (p, ^3He) donnait une section efficace de $\sigma(1^+) = 11,5 \mu\text{b}$. Dans ce cas, la limite supérieure s'est avérée être $\sigma(1^+) = 3 \mu\text{b}$. Même si on s'attend à ce que l'appariement $T = 0$ soit fort dans les noyaux $N = Z$, l'existence du terme spin-orbite dans la couche fp semble diminuer l'effet des corrélations d'appariement dans le canal isoscalaire.

Bibliography

- [1] Alexandre Obertelli. Nuclear structure from direct reactions with rare isotopes: observables, methods and highlights. *The European Physical Journal Plus*, 131(9):319, Sep 2016.
- [2] Nucleonica GmbH. Nucleonica nuclear science portal. www.nucleonica.com.
- [3] L. Olivier and S. *et al.* Franchoo. Persistence of the $z = 28$ shell gap around ^{78}Ni : First spectroscopy of ^{79}Cu . *Phys. Rev. Lett.*, 119:192501, 2017.
- [4] J. Bardeen, L. N. Cooper, and J. R. Schrieffer. Theory of superconductivity. *Phys. Rev.*, 108:1175–1204, Dec 1957.
- [5] Maria G. Mayer. On closed shells in nuclei. *Phys. Rev.*, 74:235–239, Aug 1948.
- [6] Maria Goeppert Mayer. On closed shells in nuclei. ii. *Phys. Rev.*, 75:1969–1970, Jun 1949.
- [7] Otto Haxel, J. Hans D. Jensen, and Hans E. Suess. On the "magic numbers" in nuclear structure. *Phys. Rev.*, 75:1766–1766, Jun 1949.
- [8] N. Smirnova. Shell structure evolution and effective in-medium nn interaction. In *Ecole Internationale Joliot Curie "Interaction forte dans la matiere nucleaire : nouvelles tendances"*, Lacanau, France, September 2009.
- [9] A. P. Zuker. Three-body monopole corrections to realistic interactions. *Phys. Rev. Lett.*, 90:042502, Jan 2003.
- [10] F. Nowacki and A. Poves. New effective interaction for $0\hbar\omega$ shell-model calculations in the sd – pf valence space. *Phys. Rev. C*, 79:014310, 2009.
- [11] L. *et al.* Gaudefroy. Structure of the $n = 27$ isotones derived from the $^{44}\text{Ar}(d,p)^{45}\text{Ar}$ reaction. *Phys. Rev. C*, 78:034307, 2008.

- [12] O. Sorlin and M. G. Porquet. Evolution of the $N=28$ shell closure: a test bench for nuclear forces. *Phys. Scripta*, T152:014003, 2013.
- [13] L. Gaudefroy, O. Sorlin, F. Nowacki, D. Beaumel, Y. Blumenfeld, Z. Dombrádi, S. Fortier, S. Franchoo, S. Grévy, F. Hammache, K. W. Kemper, K. L. Kratz, M. G. St. Laurent, S. M. Lukyanov, L. Nalpas, A. N. Ostrowski, Yu.-E. Penionzhkevich, E. C. Pollacco, P. Roussel, P. Roussel-Chomaz, D. Sohler, M. Stanoiu, and E. Tryggestad. Structure of the $n = 27$ isotones derived from the $^{44}\text{Ar}(d, p)^{45}\text{Ar}$ reaction. *Phys. Rev. C*, 78:034307, Sep 2008.
- [14] Y. Uozumi, O. Iwamoto, S. Widodo, A. Nohtomi, T. Sakae, M. Matoba, M. Nakano, T. Maki, and N. Koori. Single-particle strengths measured with $^{48}\text{Ca}(d, p)^{49}\text{Ca}$ reaction at 56 mev. *Nuclear Physics A*, 576:123 – 137, 1994.
- [15] Y. Uozumi, N. Kikuzawa, T. Sakae, M. Matoba, K. Kinoshita, S. Sajima, H. Ijiri, N. Koori, M. Nakano, and T. Maki. Shell-model study of ^{40}Ca with the 56-mev (d,p) reaction. *Physical Review, C (Nuclear Physics); (United States)*, 50:1, 1994.
- [16] J. J. Livingood and G. T. Seaborg. Radio isotopes of nickel. *Phys. Rev.*, 53:765–765, 1938.
- [17] Hajime Ohnuma, Teruo Suehiro, Masayuki Sekiguchi, and Satoshi Yamada. (p, d) reactions at 52 mev. i. $^{58}\text{Ni}(p, d)^{57}\text{Ni}$ (experimental). *Journal of the Physical Society of Japan*, 36(5):1236–1244, 1974.
- [18] E. Gerlic, H. Langevin-Joliot, P. Roos, J. Van de Wiele, J. P. Didelez, and G. Duhamel. Excitation of deep lying hole states in ^{11}C , ^{15}O , ^{27}Si , and ^{57}Ni with the $(^3\text{He}, \alpha)$ reaction at 216 mev. *Phys. Rev. C*, 12:2106–2110, 1975.
- [19] H. Nann, A. Saha, and S. Raman. Energy levels in ^{57}Ni from a study of the $^{59}\text{Ni}(p, t)^{57}\text{Ni}$ reaction. *Phys. Rev. C*, 18:1619–1625, Oct 1978.
- [20] H. M. Sen Gupta, Syafarudin, S. Aoki, F. Aramaki, M. Matoba, Y. Uozumi, G. Wakabayashi, T. Sakae, N. Koori, T. Maki, M. Nakano, Y. Fujita, M. Fujiwara, H. Ikegami, I. Katayama, S. Morinobu, and T. Yamazaki. Isobaric analog states observed in the $^{58}\text{Ni}(p, d)^{57}\text{Ni}$ reaction with 65 mev polarized protons. *Phys. Rev. C*, 63:017601, Nov 2000.
- [21] K. E. Rehm, F. Borasi, C. L. Jiang, D. Ackermann, I. Ahmad, B. A. Brown, F. Brumwell, C. N. Davids, P. Decrock, S. M. Fischer, J. Görres, J. Greene, G. Hackmann, B. Harss, D. Henderson, W. Henning, R. V. F. Janssens, G. McMichael, V. Nanal, D. Nisius, J. Nolen, R. C. Pardo, M. Paul, P. Reiter, J. P. Schiffer, D. Seweryniak, R. E. Segel, M. Wiescher, and

-
- A. H. Wuosmaa. Study of the $^{56}\text{Ni}(d, p)^{57}\text{Ni}$ reaction and the astrophysical $^{56}\text{Ni}(p, \gamma)^{57}\text{Cu}$ reaction rate. *Phys. Rev. Lett.*, 80:676–679, Jan 1998.
- [22] I. D. Proctor, W. Benenson, J. Dreisbach, E. Kashy, G. F. Trentelman, and B. M. Preedom. New proton-rich nuclei in the $1f_{7/2}$ shell. *Phys. Rev. Lett.*, 29:434–436, 1972.
- [23] K. Garofali, R. Robinson, and M. Thoennessen. Discovery of Chromium, Manganese, Nickel, and Copper Isotopes. *Atom. Data Nucl. Data Tabl.*, 98:356–372, 2012.
- [24] D. *et al.* Rudolph. High-spin γ -ray spectroscopy in the vicinity of ^{56}Ni . *Nuclear Physics A*, 630, 1998.
- [25] I. Reusen, A. Andreyev, J. Andrzejewski, N. Bijnens, S. Franchoo, M. Huyse, Yu. Kudryavtsev, K. Kruglov, W. F. Mueller, A. Piechaczek, R. Raabe, K. Rykaczewski, J. Szerypo, P. Van Duppen, L. Vermeeren, J. Wauters, and A. Wöhr. β -decay study of $^{54,55}\text{Ni}$ produced by an element-selective laser ion source. *Phys. Rev. C*, 59:2416–2421, 1999.
- [26] A. Sanetullaev, M.B. Tsang, W.G. Lynch, Jenny Lee, D. Bazin, K.P. Chan, D. Coupland, V. Henzl, D. Henzlova, M. Kilburn, A.M. Rogers, Z.Y. Sun, M. Youngs, R.J. Charity, L.G. Sobotka, M. Famiano, S. Hudan, D. Shapira, W.A. Peters, C. Barbieri, M. Hjorth-Jensen, M. Horoi, T. Otsuka, T. Suzuki, and Y. Utsuno. Neutron spectroscopic factors of ^{55}Ni hole-states from (p,d) transfer reactions. *Physics Letters B*, 736:137 – 141, 2014.
- [27] M. Honma, T. Otsuka, B. A. Brown, and T. Mizusaki. New effective interaction for pf -shell nuclei and its implications for the stability of the $n = z = 28$ closed core. *Phys. Rev. C*, 69:034335, Mar 2004.
- [28] M. Honma, T. Otsuka, B. A. Brown, and T. Mizusaki. Shell-model description of neutron-rich pf -shell nuclei with a new effective interaction $g_{\text{xp}f1}$. In Carl J. Gross, Witold Nazarewicz, and Krzysztof P. Rykaczewski, editors, *The 4th International Conference on Exotic Nuclei and Atomic Masses*, pages 499–502, Berlin, Heidelberg, 2005. Springer Berlin Heidelberg.
- [29] C. Barbieri and M. Hjorth-Jensen. Quasiparticle and quasihole states of nuclei around ^{56}Ni . *Phys. Rev. C*, 79:064313, Jun 2009.
- [30] P. Ring and P. Schuck. *The Nuclear Many-Body Problem*. Springer, 1980.
- [31] E. Segré. *Nuclei and Particles*. W.A. Benjamin Inc., 1965.

- [32] Professor R. C. Johnson and Dr M. Oï†. Nuclear superfluidity. pairing in finite systems, by d.m. brink and r.a. broglia. *Contemporary Physics*, 51(1):91–92, 2010.
- [33] J.-F. Berger. *Structure Nucléaire Théorique*. Formation NPAC, 2008.
- [34] N. Zeldes and S. Liran. Pairing-isopairing competition in odd-odd nuclei. *Physics Letters B*, 62(1):12 – 14, 1976.
- [35] John P. Schiffer and William W. True. The effective interaction between nucleons deduced from nuclear spectra. *Rev. Mod. Phys.*, 48:191–217, Apr 1976.
- [36] S. Frauendorf and A.O. Macchiavelli. Overview of neutron–proton pairing. *Progress in Particle and Nuclear Physics*, 78:24 – 90, 2014.
- [37] A. Bohr, B. R. Mottelson, and D. Pines. Possible analogy between the excitation spectra of nuclei and those of the superconducting metallic state. *Phys. Rev.*, 110:936–938, May 1958.
- [38] A. L. Goodman. *Adv. Nucl. Phys.*, 11:263, 1979.
- [39] G. F. Bertsch and Y. Luo. Spin-triplet pairing in large nuclei. *Phys. Rev. C*, 81:064320, Jun 2010.
- [40] Alexandros Gezerlis, G. F. Bertsch, and Y. L. Luo. Mixed-spin pairing condensates in heavy nuclei. *Phys. Rev. Lett.*, 106:252502, Jun 2011.
- [41] A. O. Macchiavelli et al. Collective $T = 0$ pairing in $N=Z$ nuclei? Pairing vibrations around Ni-56 revisited. *Phys. Lett.*, B480:1–6, 2000.
- [42] Kenichi Yoshida. Proton-neutron pairing vibrations in $n = z$ nuclei: Precursory soft mode of isoscalar pairing condensation. *Phys. Rev. C*, 90:031303, Sep 2014.
- [43] A. O. Macchiavelli, P. Fallon, R. M. Clark, M. Cromaz, M. A. Deleplanque, R. M. Diamond, G. J. Lane, I. Y. Lee, F. S. Stephens, C. E. Svensson, K. Vetter, and D. Ward. Is there np pairing in $n = z$ nuclei? *Phys. Rev. C*, 61:041303, Mar 2000.
- [44] S. M. Fischer, C. J. Lister, D. P. Balamuth, R. Bauer, J. A. Becker, L. A. Bernstein, M. P. Carpenter, J. Durell, N. Fotiades, S. J. Freeman, P. E. Garrett, P. A. Hausladen, R. V. F. Janssens, D. Jenkins, M. Leddy, J. Ressler, J. Schwartz, D. Svelnys, D. G. Sarantites, D. Seweryniak, B. J. Varley, and R. Wyss. Alignment delays in the $N = Z$ nuclei ^{72}kr , ^{76}sr , and ^{80}zr . *Phys. Rev. Lett.*, 87:132501, Sep 2001.

-
- [45] K. Kaneko, Y. Sun, and G. de Angelis. Enhancement of high-spin collectivity in $n=z$ nuclei by the isoscalar neutron–proton pairing. *Nuclear Physics A*, 957:144 – 153, 2017.
- [46] B. Cederwall et al. Evidence for a spin-aligned neutron-proton paired phase from the level structure of ^{92}Pd . *Nature*, 469:68, 2011.
- [47] P. Fröbrich. Enhancement of deuteron transfer reactions by neutron-proton pairing correlations. *Physics Letters B*, 37:338–340, December 1971.
- [48] P. Van Isacker, D. D. Warner, and A. Frank. Deuteron transfer in $n = z$ nuclei. *Phys. Rev. Lett.*, 94:162502, Apr 2005.
- [49] Y. Ayyad, J. Lee, A. Tamii, J. A. Lay, A. O. Macchiavelli, N. Aoi, B. A. Brown, H. Fujita, Y. Fujita, E. Ganioglu, K. Hatanaka, T. Hashimoto, T. Ito, T. Kawabata, Z. Li, H. Liu, H. Matsubara, K. Miki, H. J. Ong, G. Potel, I. Sugai, G. Susoy, A. Vitturi, H. D. Watanabe, N. Yokota, and J. Zenihiro. Investigating neutron-proton pairing in sd -shell nuclei via $(p, ^3\text{He})$ and $(^3\text{He}, p)$ transfer reactions. *Phys. Rev. C*, 96:021303, Aug 2017.
- [50] B. Le Crom. *Etude de l'appariement neutron-proton dans les noyaux instables $N=Z$ par réactions de transfert*. PhD thesis, Université Paris-Saclay, Institut de Physique Nucléaire, CNRS/IN2P3/Université Paris-Sud XI, 91406 Orsay Cedex, 2016.
- [51] G Potel, A Idini, F Barranco, E Vigezzi, and R A Broglia. Cooper pair transfer in nuclei. *Reports on Progress in Physics*, 76(10):106301, 2013.
- [52] NNDC. <http://www.nndc.bnl.gov>.
- [53] R.J. Furnstahl and H.-W. Hammer. *Are occupation numbers observable ?* *Physics Letters B*, 531:203–208, 2002.
- [54] T. Duguet and G. Hagen. *Ab-initio take on effective single-particle energies in double closed shell nuclei*. *Physics Review C*, 85:034330, 2012.
- [55] Y. Blumenfeld et al. *Facilities and methods for radioactive ion beam production*. *Physica Scripta*, T152:014023, 2013.
- [56] David J. Morrissey and Brad M. Sherrill. *In-Flight Separation of Projectile Fragments*, pages 113–135. Springer Berlin Heidelberg, Berlin, Heidelberg, 2004.

- [57] R. Anne, D. Bazin, A.C. Mueller, J.C. Jacmart, and M. Langevin. The achromatic spectrometer lise at ganil. *Nuclear Instruments and Methods in Physics Research Section A: Accelerators, Spectrometers, Detectors and Associated Equipment*, 257(2):215 – 232, 1987.
- [58] S. Ottini-Hustache *et al.* CATS, a low pressure multiwire proportionnal chamber for secondary beam tracking at GANIL. *Nuclear Instruments and Methodes in Physics Research A*, **431**:476–484, 1999.
- [59] M. Labiche and *et al.* TIARA: A large solid angle silicon array for direct reaction studies with radioactive beams. *Nuclear Instruments and Methods in Physics Research Section B: Accelerators, Spectrometers, Detectors and Associated Equipment*, 614:439 – 448, 2010.
- [60] E. Pollacco *et al.* MUST2: A new generation array for direct reaction studies. *The European Physical Journal*, **25**(10.1140/epjad/i2005-06-162-5):287–288, 2005.
- [61] Xesus Pereira Lopez. *Study of transfer reactions induced by a ^{16}C beam*. Theses, Université de Caen Normandie, December 2016.
- [62] F. Azaiez. Exogam: a γ -ray spectrometer for radioactive beams. *Nuclear Physics A*, 654(1, Supplement 1):1003c – 1008c, 1999.
- [63] Kwong Lau and Jörg Pyrlik. Optimization of centroid-finding algorithms for cathode strip chambers. *Nuclear Instruments and Methods in Physics Research Section A: Accelerators, Spectrometers, Detectors and Associated Equipment*, 366(2):298 – 309, 1995.
- [64] A. Ramus. *Etude des noyaux instables ^{19}O et ^{25}Ne par réaction de transfert à l'aide du dispositif MUST2-TIARA-VAMOS-EXOGAM*. Theses, Université Paris Sud - Paris XI, September 2009.
- [65] Remy Anne and Alex C. Mueller. Lise 3: a magnetic spectrometer—wien filter combination for secondary radioactive beam production. *Nuclear Instruments and Methods in Physics Research Section B: Beam Interactions with Materials and Atoms*, 70(1):276 – 285, 1992.
- [66] O.B. Tarasov and D. Bazin. Lise++: Radioactive beam production with in-flight separators. *Nuclear Instruments and Methods in Physics Research Section B: Beam Interactions with Materials and Atoms*, 266(19):4657 – 4664, 2008.
- [67] GEANT4. <http://geant4.cern.ch>.

-
- [68] A Matta, P Morfouace, N de Séréville, F Flavigny, M Labiche, and R Shearman. Nptool: a simulation and analysis framework for low-energy nuclear physics experiments. *Journal of Physics G: Nuclear and Particle Physics*, 43(4):045113, 2016.
- [69] ROOT. <http://root.cern.ch.drupal>.
- [70] Andrew E. Stuchbery. γ -ray angular distributions and correlations after projectile-fragmentation reactions. *Nuclear Physics A*, 723:69 – 92, 2003.
- [71] D. Rudolph, C. Baktash, M. J. Brinkman, M. Devlin, H. Q. Jin, D. R. LaFosse, M. Leddy, I. Y. Lee, A. O. Macchiavelli, L. L. Riedinger, D. G. Sarantites, and C. H. Yu. High-spin states in the $t_z=-1/2$ nucleus ^{55}Ni . *Zeitschrift für Physik A Hadrons and Nuclei*, 358(4):379–380, Dec 1997.
- [72] P. Morfouace. *Single-particle states in neutron-rich $^{69,71}\text{Cu}$ by means of the $(d, ^3\text{He})$ transfer reaction*. PhD thesis, Université Paris-Sud XI, Institut de Physique Nucléaire, CNRS/IN2P3/Université Paris-Sud XI, 91406 Orsay Cedex, 2014.
- [73] F. Flavigny. *Détermination de facteurs spectroscopiques absolus par réaction de knockout et de transfert*. PhD thesis, Université Paris-Sud XI, CEA, 2011.
- [74] G.R. Satchler. *Direct nuclear reactions*. International series of monographs on physics. Clarendon Press, 1983.
- [75] D. Y. Pang *et al.* Global optical model potential for $A = 3$ projectiles. *Physical Review C*, **79**:024615, 2009.
- [76] R.L. Varner, W.J. Thompson, T.L. McAbee, E.J. Ludwig, and T.B. Clegg. A global nucleon optical model potential. *Physics Reports*, 201(2):57 – 119, 1991.
- [77] W. W. Daehnick, J. D. Childs, and Z. Vrcelj. Global optical model potential for elastic deuteron scattering from 12 to 90 mev. *Phys. Rev. C*, 21:2253–2274, Jun 1980.
- [78] Ian J. Thompson. Coupled reaction channels calculations in nuclear physics. *Computer Physics Reports*, 7(4):167 – 212, 1988.
- [79] C.M. Perey and F.G. Perey. Compilation of phenomenological optical-model parameters 1954–1975. *Atomic Data and Nuclear Data Tables*, 17(1):1 – 101, 1976.
- [80] Jenny Lee, M. B. Tsang, and W. G. Lynch. Neutron spectroscopic factors from transfer reactions. *Phys. Rev. C*, 75:064320, 2007.

- [81] R.O.Nelson *et al.* Study of low lying levels of ^{53}Fe . *Nuclear Physics A*, 215:541–556, 1973.
- [82] P.J.Plauger *et al.* (p,d) reaction in the titanium isotopes. *Nuclear Physics A*, 152:609–630, 1970.
- [83] D.J. Martin, J.R. Leslie, W. Mclatchie, C.F. Monahan, and L.E. Carlson. The γ -ray decay properties of analogue states of ^{55}Fe excited in the reaction $^{54}\text{Fe}(p, \gamma)^{55}\text{Co}$. *Nuclear Physics A*, 187(2):337 – 354, 1972.
- [84] Y. DUPONT P. MARTIN, M. BUENERD and M. CHABRE. Proton-deuteron reactions at 40 mev on the calcium isotopes. *Nuclear Physics A*, 185:465–487, 1972.
- [85] R. Raabe. Actar: the new generation of active targets. *AIP Conference Proceedings*, 1165(1), 8 2009.
- [86] W. Mittig, S. Beceiro-Novo, A. Fritsch, F. Abu-Nimeh, D. Bazin, T. Ahn, W.G. Lynch, F. Montes, A. Shore, D. Suzuki, N. Usher, J. Yurkon, J.J. Kolata, A. Howard, A.L. Roberts, X.D. Tang, and F.D. Becchetti. Active target detectors for studies with exotic beams: Present and next future. *Nuclear Instruments and Methods in Physics Research Section A: Accelerators, Spectrometers, Detectors and Associated Equipment*, 784:494 – 498, 2015. Symposium on Radiation Measurements and Applications 2014 (SORMA XV).
- [87] A. Gillibert *et al.* Windowless thin solid-hydrogen target: Chymene. *The European Physical Journal A*, 49(12):155, Dec 2013.

Titre : Réactions de transfert induites avec ^{56}Ni : l'appariement neutron-proton et le fermeture de couche N=28

Mots clés : structure nucléaire, réaction de transfert, appariement

Résumé : La structure du noyau N = Z doublement magique ^{56}Ni (N = 28, Z = 28) a été étudiée en mesurant les réactions de transfert à un et deux nucléons. Le transfert nous donne des informations sur deux aspects physiques différents: la fermeture de couche N = 28 et l'intensité de l'appariement neutron-proton. Le nombre magique N=28 est particulier, car c'est le premier créé par le spin-orbit. La double magie permet la détermination de la nature de particule indépendante des voisins N±1 par réaction de transfert d'un nucléon. De plus, en tant que noyau N=Z à couches fermées, le ^{56}Ni est un noyau clé pour l'étude de l'appariement np dans la plus grande couche accessible expérimentalement. L'appariement np se manifeste dans le canal isoscalaire (T=0) et isovecteur (T=1). L'intensité relative de chaque canal révèle la nature collective des états. L'expérience de ce travail a eu lieu au GANIL-Caen, en France, avec un faisceau radioactif de ^{56}Ni à 30 MeV / u produit par fragmentation de ^{58}Ni et purification avec le spectromètre LISE. Les mesures ont été effectuées en cinématique inverse sur des cibles CH2 et CD2. Les détecteurs

MUST2 et TIARA ont été utilisés pour la détection de éjectiles légers et couvraient presque 4π . En outre, quatre détecteurs germanium d'EXOGRAM ont été utilisés pour les coïncidences de particules-gamma afin d'identifier l'état peuplé du résidu de réaction. Pour étudier le gap de N = 28, nous étudions la spectroscopie du ^{55}Ni par les réactions de transfert de nucléons (d, t) et (p, d) sur le ^{56}Ni . Le spectre en énergie d'excitation est déduit de la mesure des éjectiles légers seulement. Ensuite, les coïncidences particule-gamma sont utilisées pour améliorer la résolution et identifier les principaux états peuplés. La comparaison des distributions angulaires ainsi obtenues avec des calculs DWBA permet d'extraire les facteurs spectroscopiques pour les états de particules et de trous ainsi peuplés. En ce qui concerne l'appariement np, nous avons analysé la réaction $^{56}\text{Ni}(d,\alpha)^{54}\text{Co}$ qui réalise un transfert de paires neutron-proton. Un affaiblissement du canal T=0 à cause de l'effet du spin-orbite est attendu. La sélectivité en $\Delta T=0$ de la réaction (d, α) permet d'étudier plus en détail le canal isoscalaire T = 0.

Title : Transfer Reactions Induced with ^{56}Ni : Pairing and N=28 Shell Closure

Keywords : nuclear structure, transfer reactions, pairing

Abstract : The structure of the unstable doubly magic nucleus ^{56}Ni has been investigated by measuring one- and two-nucleon transfer reactions. Each transfer reaction provides information for two different physical aspects: the robustness of the N=28 shell gap and the strength of the neutron-proton pairing. ^{56}Ni is a self-conjugate doubly magic nucleus with N=28 and Z=28. The magic number 28 is a peculiar shell closure created by spin-orbit splitting effects. The double magicity makes the determination of the single-particle nature of their N±1 neighbors by one-neutron transfer reaction of major interest to test both the robustness of shell closures as well as the evolution of particle and/or valence orbitals. Moreover ^{56}Ni , as a N=Z nucleus with fully closed shells, is a key nucleus to investigate neutron-proton pairing in the largest shell accessible experimentally, the fp shell. Neutron-proton pairing can occur both in the isoscalar (T=0) and in the isovector (T=1) channels. The relative intensity of both channels reveals the collective nature of the states. The radioactive beam of ^{56}Ni was produced at

GANIL-Caen, France at 30 MeV/u by fragmentation of ^{58}Ni and purification with the LISE spectrometer. The experimental set-up used, consists of the TIARA-MUST2-EXOGRAM combination which provides an almost 4π coverage and the ability to perform particle- γ coincidences. To probe the N=28 gap, we studied the spectroscopy of ^{55}Ni through one-nucleon transfer reactions on ^{56}Ni . The excitation energy spectrum is deduced by measuring the light ejectiles only, while particle- γ coincidences are used to improve the resolution of the populated states and select the main ones. Comparison in between the extracted angular distributions and DWBA calculations allow the extraction of the spectroscopic strength of the hole- and particle- states populated by these one neutron pick-up reactions. As for neutron-proton pairing, a weakening of the strength is expected in the T=0 channel from previous results. The selectivity in $\Delta T=0$ of the $^{56}\text{Ni}(d,\alpha)^{54}\text{Co}$ reaction enables further investigation of the isoscalar channel contribution.

